A Measurement of the W Boson Mass in $p\overline{p}$ collisions at $\sqrt{s} = 1.8\ TeV$

By

Eric M. Flattum

A DISSERTATION

Submitted to
Michigan State University
in partial fulfillment of the requirements
for the degree of

DOCTOR OF PHILOSOPHY

Department of Physics and Astronomy

1996

ABSTRACT

A Measurement of the W Boson Mass in $p\overline{p}$ collisions at $\sqrt{s} = 1.8\ TeV$

By

Eric M. Flattum

A measurement of the W boson mass has been performed using $W \rightarrow e\nu$ decays in $p\overline{p}$ collisions at $\sqrt{s} = 1.8\ TeV$ at DØ from the 1994-1995 Tevatron run. The mass is determined by fitting to the transverse mass distribution of the W boson events which have an electron in the central calorimeter ($|\eta| < 1.0$). The number of events in the fit region of $60 < m_t < 90\ GeV/c^2$ is 27,040. The constraints on the model are determined from a sample of 1562 $Z \rightarrow ee$ events. The measured W boson mass is $M_W = 80.346 \pm 0.069(stat.) \pm 0.091(syst.) \pm 0.077(scale)$. This is the most precise measurement of the W boson mass to date.

To Marian.

ACKNOWLEDGEMENTS

There are many people to I'd like to thank for helping me to get to this point in my life and career. I begin by thanking my advisor Chip for the many useful discussions and support he has given to me over the years, along with the the freedom to explore and develop as a physicist.

I'd like to thank my family and friends for their support they've given me. A special thanks to my wife, Marian, for the understanding she has shown during this journey. The baby gets a special thanks for speeding up my graduation. I'd like to thank all my friends from the old days, Al, Shawn, and the rest.

It takes a large number of people to do a measurement like this and it was only through the collaborative effort of the W mass group that this analysis has come to its fruition. I'd like to thank the people involved, Zhu, Chip, John, Marcel, Kathy, Srini, Norman, Uli, Ian, Ashintosh, and Michael. I'd like to especially thank Uli and Ian for the close collaborative effort put forth to get the Run 1b measurement to this stage.

I'd like to thank all the people I've had the privilege to meet, work, and become friends with. The list is long, and I'll probably miss someone, but I'd like to recognize Rich, Ian, Sal, Kate, Steve, Jamal, Dylan, and the rest.

And a special recognition must go to the mighty Prerna soccer team; champions

at last.

Differing weights and differing

measures—

the LORD detests them both.

PROVERBS 20:10

Contents

List of Tables

List of Figures

Chapter 1

Introduction

1.1 Introduction

The discovery of the W and Z bosons at the European Nuclear Research Center (CERN) was a remarkable verification of the theory set forth by Glashow, Salam and Weinberg (GSW) [1]. The massive carriers of the electroweak force have been the subject of intense study at the proton-antiproton colliders at CERN and Fermilab. Precise mass measurements of the W and Z boson seek to provide ever more stringent tests of the theory and constraints upon unobserved particles. Table 1.1 gives an historical account of the W boson mass measurements since discovery [2-13].

The Z boson mass (M_Z) has been been measured to very high precision at the Large Electron Positron (LEP) accelerator. The current world average for the Z boson mass is [14]:

$$M_Z = 91.1884 \pm 0.0022\ GeV/c^2 \tag{1.1}$$

Experiment and Year	Decay Channel	Mass and Error (GeV/c^2)	Number of Events
UA1-83	$e\nu$	81 ± 5	6
UA2-83	$e\nu$	80^{+10}_{-6}	4
UA1-84	$\mu\nu$	81^{+6}_{-7}	14
UA1-86	$e\nu$	$83.5^{+1.1}_{-1.0} \pm 2.7$	172
UA2-87	$e\nu$	$80.2 \pm 0.6 \pm 0.5 \pm 1.3$	251
UA1-89	$e\nu$	$82.7 \pm 1.0 \pm 2.7$	240
UA1-89	$\mu\nu$	$81.8^{+6.0}_{-5.3} \pm 2.6$	67
UA1-89	$\tau\nu$	$89 \pm 3 \pm 6$	32
CDF-89	$e\nu, \mu\nu$	$80.0 \pm 3.3 \pm 2.4$	22
UA2-90	$e\nu$	$80.49 \pm 0.43 \pm 0.24$	1203
CDF-90	$e\nu, \mu\nu$	79.91 ± 0.39	1722
UA2-92	$e\nu$	$80.35 \pm 0.33 \pm 0.17$	2065
CDF-95	$e\nu, \mu\nu$	80.410 ± 0.180	8986
DØ -96	$e\nu$	80.35 ± 0.27	7234

Table 1.1: A listing of W boson mass measurements since discovery in 1983 to present.

The precision of M_Z is $\frac{\delta M_Z}{M_Z} = 0.0024\%$. The world average W boson mass is[1]

$$M_W = 80.34 \pm 0.15\ GeV/c^2. \tag{1.2}$$

The precision of M_W is only $\frac{\delta M_W}{M_W} = 0.19\%$. The subject of this thesis is the measurement of the W boson mass with a precision that is better than the world average.

The chapters are structured in the following way. Chapter 2 covers the physics theory of the production and decay of the W and Z bosons. Chapter 3 discusses the experimental apparatus. Chapter 4 covers the selection of events used in the analysis. Chapter 5 covers the Monte Carlo used to determine the W boson mass. The

[1]The world average is determined from the measurements in references [10, 11, 12] and [13].

Monte Carlo includes a discussion of the input physics model, detector resolutions, efficiencies, and cuts. Also, chapter 5 includes how the parameters for the Monte Carlo are determined. Chapter 6 discusses the calibration of the electromagnetic energy scale. Chapter 7 covers the systematic errors associated with the W boson mass and chapter 8 the conclusions.

Chapter 2

The Physics

2.1 Introduction

High energy physics involves the study of matter and forces at a fundamental level. The four forces at work in nature are, in order of strength: the strong nuclear force, electromagnetism, the weak nuclear force, and gravity. These forces interact with matter through the exchange of particles. An example of how particles interact is given by electromagnetism. Consider two electrons positioned a given distance apart. Each electron has electromagnetic charge and so emits a field of virtual photons. The photons from one electron are absorbed by the other. It is through this *mediation* of photons that the electromagnetic force acts upon one electron from the other. Each of the forces of nature can be described by an analogous emission and absorption of particles. Table 2.1 lists the particles that mediate the four forces and some of their properties. The particles that mediate the forces are referred to as vector bosons.

Force	Particle	Mass (GeV/c^2)	Spin
Strong Nuclear	Gluon (g)	0	1
Electromagnetic	Photon (γ)	0	1
Weak Nuclear	W and Z	$\sim$80 and $\sim$90	1
Gravity	Graviton (G)	0	2

Table 2.1: The bosons that mediate the forces of nature.

Charge	Family 1	Family 2	Family 3
$+\frac{2}{3}$	up (u)	charm (c)	top (t)
$-\frac{1}{3}$	down (d)	strange (s)	bottom (b)
-1	electron (e)	muon (μ)	tau (τ)
0	electron neutrino (ν_e)	muon neutrino (ν_μ)	tau neutrino (ν_τ)

Table 2.2: The three families of quarks and leptons. The fractionally charged particles are the quarks and the others are the leptons.

A vector boson is a particle whose spin has an integer value. The particles that matter is composed of are called fermions. Fermions are particles with half-unit spin values and are listed in table 2.2. All matter observed in our everyday lives is made of up and down quarks, and electrons. Each force does not act upon each fermion, table 2.3 lists which forces act upon a given fermion. The topic of this thesis is a measurement of the mass of the W boson.

Force	Neutral Leptons ν_e, ν_μ, ν_τ	Charged Leptons e, μ, τ	Quarks u, d, c, s, t, b
Strong Nuclear			X
Electromagnetism		X	X
Weak Nuclear	X	X	X
Gravity	X	X	X

Table 2.3: The forces that act upon each fermion.

2.2 The Standard Model of Electroweak Interactions

The standard model of electroweak interactions is based upon the $\mathrm{SU}(2)_L \times \mathrm{U}(1)$ gauge group. Observation of the transition of $\nu_e \leftrightarrow e$ in weak interactions suggested that the leptons be combined into a doublet on which a symmetry group acts. The $\mathrm{SU}(2)_L$ group was suggested to give the theory *weak isospin*. The subscript L states that the group only acts upon the left handed component of the field since it was known that neutrinos participating in a weak decay only have negative helicity. Helicity is defined as the projection of the spin along the momentum axis. The lepton doublets and singlets are

$$\begin{pmatrix} \nu_e \\ e \end{pmatrix}_L, \begin{pmatrix} \nu_\mu \\ \mu \end{pmatrix}_L, \begin{pmatrix} \nu_\tau \\ \tau \end{pmatrix}_L, e_R,\ \mu_R,\ \tau_R$$

where the subscript R refers to the right handed component of the fields. A natural extension was to include the the quarks that participate in the weak interaction with the same form. The quark doublets and singlets are written as

$$\begin{pmatrix} u \\ d' \end{pmatrix}_L, \begin{pmatrix} c \\ s' \end{pmatrix}_L, \begin{pmatrix} t \\ b' \end{pmatrix}_L, u_R,\ c_R,\ t_R,\ d_R,\ s_R,\ b_R.$$

The prime on d, s, and b indicates that the quark mass eigenstates are not the same as the weak eigenstates. Though, the weak eigenstates may be written was a linear combination of mass eigenstates. For the case in which there are only two families

of quarks d' is written in the following manner

$$d' = d\cos\theta_C + s\sin\theta_C \tag{2.1}$$

where θ_C is known as the Cabibbo angle and regulates the mixing between the families.

The inclusion of the abelian U(1) group incorporates the electric charge into the theory. The $SU(2)_L \times U(1)$ group then yields two charged and two neutral bosons. The bosons must be massless in order for the theory to be renormalizable. It is through the "Higgs mechanism" that the symmetry of the $SU(2)_L \times U(1)$ is broken and the charged ($W^{\pm}$) and neutral (Z) bosons acquire mass with the photon remaining massless.

Three parameters are needed to describe the masses and interactions in this theory. They are the coupling strengths of the weak isospin (g), the hypercharge (g') from the U(1) group, and the vacuum expectation value (v) from the spontaneous symmetry breaking. The three fundamental parameters are given by the following relations

$$g = \frac{e}{\sin\Theta_W} \tag{2.2}$$

$$g' = \frac{e}{\cos\Theta_W} \tag{2.3}$$

$$\mathrm{v} = \frac{2M_W}{g} \tag{2.4}$$

where e is the charge of the positron, M_W is the W boson mass, and Θ_W is the weak mixing angle [15, 16]. It is often more convenient to work with parameters

determined from low energy weak interactions. The variables of choice are the fine structure constant ($\alpha_{em}=\frac{e^2}{4\pi}$), the Fermi constant ($G_F$), and $\sin^2\Theta_W$. The first two are known to a very high precision; α_{em} from the quantum Hall effect and G_F from the lifetime of the muon [17]. The current values for $\alpha_{em}(Q^2 \approx 0)$ and G_F are [18]:

$$\alpha_{em} = 1/137.0359895(61) \tag{2.5}$$

$$G_F = 1.16639(2) \times 10^{-5}\, GeV^{-2}. \tag{2.6}$$

At the lowest order of perturbation theory the masses of the W and Z bosons are then given by the following relations

$$M_W = \frac{A}{\sin\Theta_W} \tag{2.7}$$

$$M_Z = \frac{A}{\sin\Theta_W \cos\Theta_W} \tag{2.8}$$

where

$$A = \left(\frac{\pi\alpha_{em}}{\sqrt{2}G_F}\right)^{\frac{1}{2}} \tag{2.9}$$

and $\sin^2\Theta_W$ is defined as

$$\sin^2\Theta_W \equiv 1 - \frac{M_W^2}{M_Z^2}. \tag{2.10}$$

With a measurement of $\sin^2\Theta_W$ the W and Z boson masses can be predicted using equations 2.7 and 2.8. Using the current value of the weak mixing angle [18] the predicted masses are $\sim$77 and $\sim$88 GeV/c^2 respectively.

The addition of higher-order loop diagrams in the calculation modifies equation 2.7 in the following way

$$M_W = \frac{A}{\sin\Theta_W\sqrt{1-\Delta R}} \tag{2.11}$$

where $\Delta R = \Delta R(M_{Higgs}, M_{quarks}, M_{leptons}, ...)$ incorporates the effects of higher order quantum corrections and depends upon the masses in the theory. The value of equation 2.9 is also modified because of the running of the electromagnetic coupling constant to the scale of M_W. The mass dependence on the two most interesting particles, the Higgs boson and Top quark, enter in the following way

$$\Delta R(M_{Higgs}) \propto \ln\left(\frac{M_{Higgs}}{M_W}\right) \tag{2.12}$$

$$\Delta R(M_{Top}) \propto \left(\frac{M_{Top}}{M_W}\right)^2 \tag{2.13}$$

It is through equation 2.11 that a precise measurement of the M_W and M_{Top} will constrain the mass of the Higgs. Figure 2.2 is two examples of the self energy diagrams that go into the calculations of equations 2.12 and 2.13. Figure 2.2 shows the allowed values of the Higgs mass as a function of the M_W and M_{Top} masses [12, 13, 19, 20]. As this point the precision of the measurements is insufficient to rule out any value of the Higgs mass.

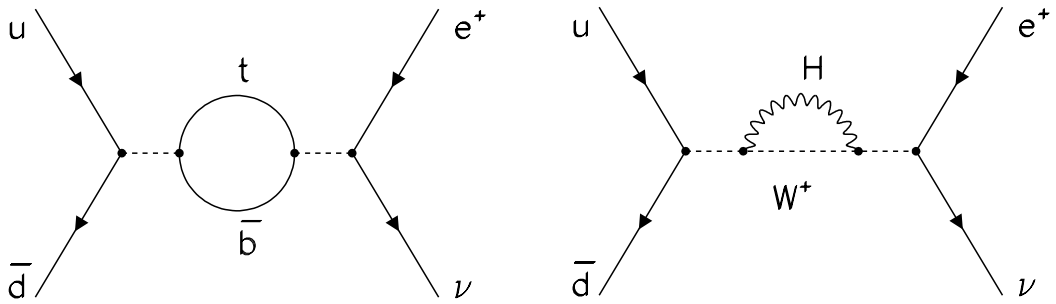

Figure 2.1: Examples of the W boson self energy diagrams involving the Top quark and Higgs particle.

2.3 W^+ Production

This section covers how W boson events are produced and observed at Fermilab. W^+ production is chosen for convenience but the discussion is also valid for W^- and Z boson events. At lowest order a W boson is produced through quark-antiquark annihilation. The valence quark content of the (anti)proton is two (anti)up quarks and a (anti)down quark. An example of the production of a W^+ would be

$$u\overline{d} \rightarrow W^+. \tag{2.14}$$

The momentum of a quark in a proton is given by its momentum fraction (x) times the momentum of the proton. The proton direction is defined as the $+Z$ direction.

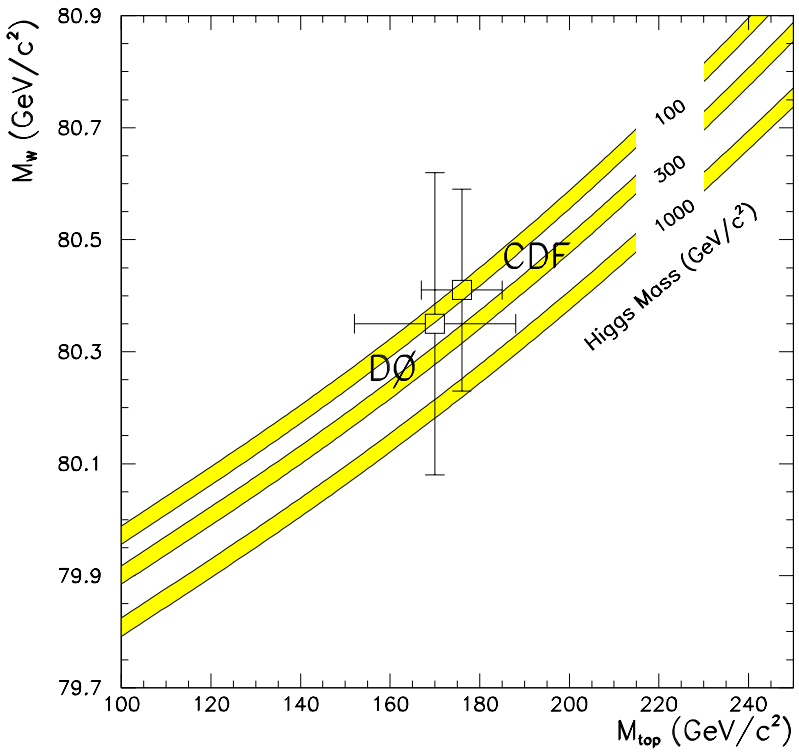

Figure 2.2: Allowed Higgs mass values as a function of W boson and Top quark masses. The two points are the measurements of the W boson and Top quark masses from DØ and CDF.

The energy and momentum of the W boson are given by

$$E = \frac{\sqrt{s}}{2}(x_p + x_{\overline{p}}) \tag{2.15}$$

$$P_L = \frac{\sqrt{s}}{2}(x_p - x_{\overline{p}}) \tag{2.16}$$

where $\sqrt{s}$ is the center of mass energy of the proton-antiproton system and $x_p(x_{\overline{p}})$ is the momentum fraction of the quark from the proton(antiproton). A useful quantity

is the rapidity (y) of a particle which is defined to be

$$y \equiv \frac{1}{2} \ln \left(\frac{E + P_L}{E - P_L} \right) \tag{2.17}$$

where E is the energy and P_L is the longitudinal momentum. Since, $E^2 = (\vec{p}c)^2 + (mc^2)^2$ in the limit of $mc^2 \ll E$ equation 2.17 becomes

$$\eta = -\ln \left(\tan \frac{\theta}{2} \right) \tag{2.18}$$

where θ is the polar angle and η is referred to as the the pseudorapidity. Equation 2.18 is not valid for the W boson because of the large mass but it is valid for the decay products of the boson. By inserting equations 2.15 and 2.16 into 2.17 the rapidity reduces to

$$y = \frac{1}{2} \ln \frac{x_p}{x_{\overline{p}}}. \tag{2.19}$$

The total cross section for W^+ production as shown in equation 2.14 is the sum over all possible quark combinations from the proton-antiproton system and is given by

$$\begin{aligned} \frac{d\sigma}{dy}\left(u\overline{d} \rightarrow W^+\right) = K \frac{2\pi G_F}{3\sqrt{2}} x_p x_{\overline{p}} \{ & u_v(x_p)\overline{d_v}(x_{\overline{p}}) + u_v(x_p)\overline{d_s}(x_{\overline{p}}) + \\ & u_s(x_p)\overline{d_v}(x_{\overline{p}}) + u_s(x_p)\overline{d_s}(x_{\overline{p}}) + \overline{d_s}(x_p)u_s(x_{\overline{p}}) \} \cos\theta_c \end{aligned} \tag{2.20}$$

where the subscript $v(s)$ represents a valance(sea) quark, K includes higher order

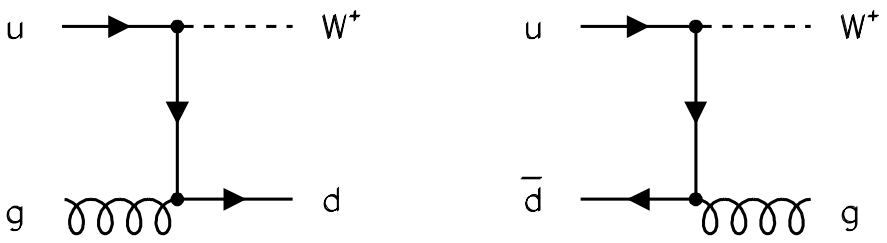

Figure 2.3: The Compton diagrams which contribute to the transverse momentum of the W boson.

QCD corrections, and the 1/3 is due to averaging over the number of quark colors in the initial state.

For the interaction shown in equation 2.14 the W boson does not have any momentum transverse (p_T^W) to the Z direction. All W boson events produced in $p\overline{p}$ collisions have some transverse momentum due to initial state gluon radiation and the Fermi motion of the quarks in the hadron. Initial state gluon radiation is when a quark radiates gluons before it annihilates to produces the W boson. Figure 2.3 shows the lowest order Compton diagrams that contribute to the transverse momentum of the W boson. At the Tevatron the average p_T^W is about 6 GeV/c. The calculation of $\frac{d\sigma}{dp_T^W}$ is complicated and beyond the scope of this paper. See references [21, 22, 23] for more details of this calculation.

2.4 Nature of the $W^+ \rightarrow e^+\nu$ decay

Up to this point only the production of the W boson has been discussed. Due to its large mass the W boson decays within $\sim 10^{-25}$ seconds. Therefore, to measure the mass of the W boson information must be extracted from the particles into which it decays. So which decay channel will allow for the best measurement of the W boson mass? The W boson decays into quark-antiquark and lepton-neutrino pairs. Table 2.4 lists the decay products of the W boson and the fraction of time that the decay occurs. The $q\overline{q}'$ pairs have the largest cross section. What is observed in the detector, when a $q\overline{q}'$ pair is produced, are two *jets* [24] of particles. The $W \rightarrow q\overline{q}'$ channel suffers from a huge background from direct production dijets. This leaves us with only the lepton modes. In the tau channel the τ predominantly decays into hadrons making this channel difficult for two reasons. The first is simply the difficulty in separating the signal from the large QCD background and the jet energy scale is not known well enough to make a precise mass measurement. The muon channel also does not allow for a precise mass measurement since the DØ detector does not have good momentum resolution for high p_T muons and there is no way of determining the momentum scale with sufficient accuracy for a mass measurement. This leaves only the electron channel to measure the mass.

The properties of the leptons from the W boson decay are now discussed. The calculation of the spin averaged differential cross section is given by [16]

$$\frac{d\hat{\sigma}}{d\cos\theta^*}(u\overline{d} \rightarrow e^+\nu) = \frac{\mid V_{ud} \mid^2}{8\pi}\left(\frac{G_F M_W^2}{\sqrt{2}}\right)^2 \frac{\hat{s}(1+\cos\theta^*)^2}{(\hat{s}-M_W^2)^2 + (,_W M_W)^2} \qquad (2.21)$$

Decay Product	Branching Ratio
$u\overline{d}, u\overline{s}, c\overline{s}, c\overline{d}$	$\sim$68%
$e^+\nu, \mu^+\nu, \tau^+\nu$	$\sim$32%

Table 2.4: The decay products of the W^+ and the branching ratios.

where θ^* is the angle between the positron and the $\overline{d}$ direction and $\hat{s}$ is the center of mass energy of the $u\overline{d}$ pair. The neutrino passes through the detector without interacting so its presence can only be inferred from the momentum imbalance in the event. Since many highly energy particles escape detection due to the calorimeter extending only out to an $|\eta| \sim 4$ only the momentum in the plane transverse to the beam direction can be balanced. Rewriting equation 2.21 in terms of the transverse momentum of the lepton (p_T) yields

$$\frac{d\hat{\sigma}}{d\hat{p}_T^2}(u\overline{d} \rightarrow e^+\nu) = \frac{\mid V_{ud} \mid^2}{\pi} \left(\frac{G_F M_W^2}{\sqrt{2}}\right)^2 \frac{1}{\left(\hat{s} - M_W^2\right)^2 + \left(, _W M_W\right)^2} \frac{1 - 2\hat{p}_T^2/\hat{s}}{\sqrt{1 - 4\hat{p}_T^2/\hat{s}}} \quad (2.22)$$

The divergence, when $\hat{p}_T = \frac{1}{2}\sqrt{\hat{s}}$, is known as the Jacobian edge and is a characteristic of all two body decays. The edge occurs at half the mass of the decaying particle so by knowing the distribution of the lepton transverse momentum one is then able to measure the mass of the decaying particle. Now, equation 2.22 is a calculation done at the parton level. The total cross section is a convolution over all possible momenta and quark states and is given by

$$\frac{d\sigma}{dp_T^2}(p\overline{p} \rightarrow e^+\nu X) = \frac{1}{3}\sum_{q,\overline{q}'} \int_0^1 dx_p \int_0^1 dx_{\overline{p}} f_q(x_p) f_{\overline{q}'}(x_{\overline{p}}) \frac{d\hat{\sigma}}{d\hat{p}_T^2} \quad (2.23)$$

where $f_q(x_p)$ is the fraction of momentum carried by quark(antiquark) $q(\overline{q}')$ from the (anti)proton. The singularity in equation 2.22 is removed by the integration over the Breit-Wigner lineshape and the finite natural width of the W boson.

A problem with measuring M_W from the transverse momentum distribution of the lepton is the uncertainty in p_T^W. This is because the transverse momentum of the W adds directly to the lepton momentum distorting the Jacobian edge. The calculations of the p_T^W contain theoretical uncertainties which lead to an uncertainty on the W boson mass. Another quantity that also has a Jacobian edge is the transverse mass (m_t) which is given by

$$\begin{aligned} m_t &= \sqrt{\left(\mid \vec{p_T^e} \mid + \mid \vec{p_T^\nu} \mid\right)^2 - \left(\vec{p_T^e} + \vec{p_T^\nu}\right)^2} \\ &= \sqrt{2p_T^e p_T^\nu \left(1 - \cos\phi^{e\nu}\right)} \end{aligned} \tag{2.24}$$

where $\vec{p_T^e}$ and $\vec{p_T^\nu}$ are the electron and neutrino transverse momenta. The transverse mass is unaffected by longitudinal Lorentz transformations (boosts) and is only affected at second order by transverse boosts [25]. It is with the transverse mass that the W boson mass will be measured.

Chapter 3

Fermilab and the DØ Detector

3.1 Fermilab

The Fermi National Accelerator Laboratory is the highest energy collider in the world with a center of mass energy of the proton-antiproton ($p\overline{p}$) collisions of 1.8 TeV. Five different accelerators are used to achieve this energy. Figure 3.1 shows the locations of the accelerators and the DØ and CDF experimental halls.

The first stage uses a Cockroft-Walton to accelerate H^- ions to 750 keV. The hydrogen ions are then injected into the Linac which is approximately 150 m long. The Linac is made up of nine drift tubes whose spacing increases along the length of the device. The ions drift inside the tube when the alternating electric field is in the wrong direction and are accelerated when they emerge from a drift tube. At the end of the Linac the ions have reached of 400 MeV, a carbon foil is used to strip the ion of its electrons leaving the bare proton. The Booster is a synchrotron which uses

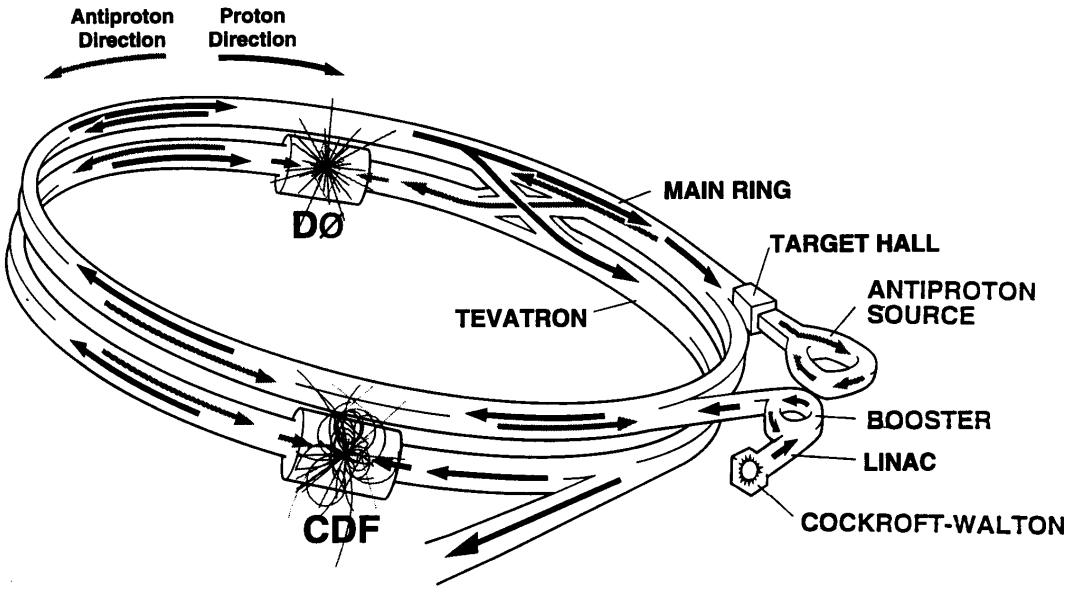

Figure 3.1: The Fermilab accelerators and experimental hall locations.

magnets to bend the protons in a circle while a radiofrequency (RF) cavity increases the energy of the beam. The Booster accelerates the protons to 8 GeV. The fourth and fifth stages are also synchrotrons that are housed in the four mile underground tunnel. The fourth stage, known as the Main Ring, is made of 1000 conventional copper-coiled magnets which are used to increase the protons energy to 150 GeV. The Tevatron finally accelerates the beam to 900 GeV. The Tevatron is made of 1000 superconducting magnets operating at liquid helium temperatures.

If the accelerator is making antiprotons then the Main Ring only accelerates the protons to 120 GeV. This beam is then extracted and sent to a nickel target which produces a series of secondary particles. The resulting particles contain a fraction of antiprotons which are then collected and stored in the antiproton Accumulator.

Once a suitable number of antiprotons have been collected they are extracted from the Accumulator and injected into the Main Ring. The Main Ring accelerates them to 150 GeV and injects them into the Tevatron. When the accelerator is operating in the collider mode six bunches of protons and antiprotons are circulating in the Tevatron. When all twelve bunches have been injected into the Tevatron they are ramped up to 900 GeV. At this energy the crossing time of the bunches is 3.5 μsec. The beams are allowed to collide at the locations along the ring which house the DØ and CDF detectors. The beams are kept apart at the other four locations by electrostatic separators.

3.2 The DØ Detector

The purpose of the DØ Detector [26, 27] is to measure particles produced in $p\overline{p}$ collisions. The DØ Detector is a very large instrument weighting 5000 tons and standing 40 feet tall. It consists of three major subsystems: the central tracker, the calorimeter, and a magnetic muon spectrometer. Figure 3.2 shows the major systems of the detector.

3.2.1 The Central Tracker

The central tracker is used to determine the spatial orientation for a charged particle and to provide discriminating power between the different particles produced during the collision. The idea behind the tracking system is that when a charged particle

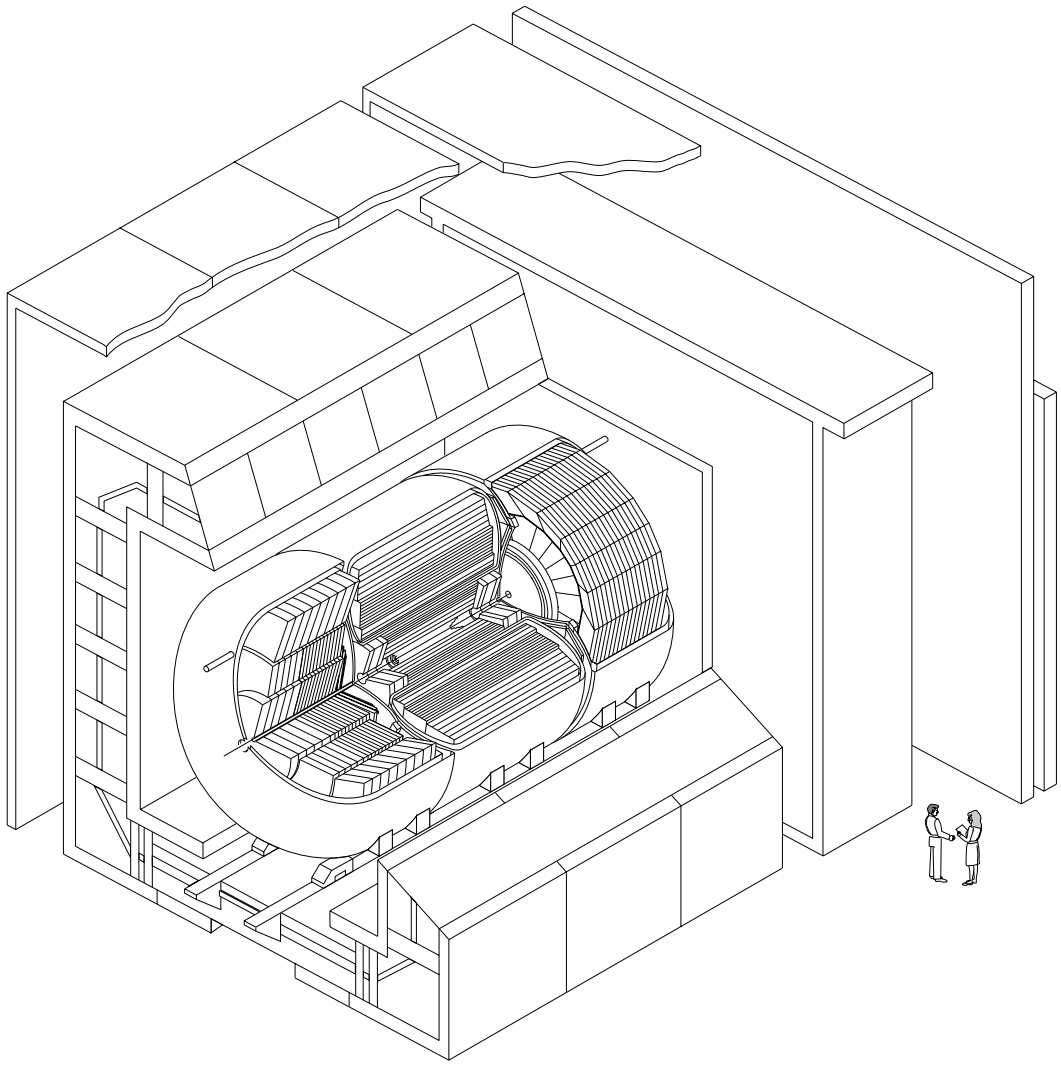

Figure 3.2: The DØ detector.

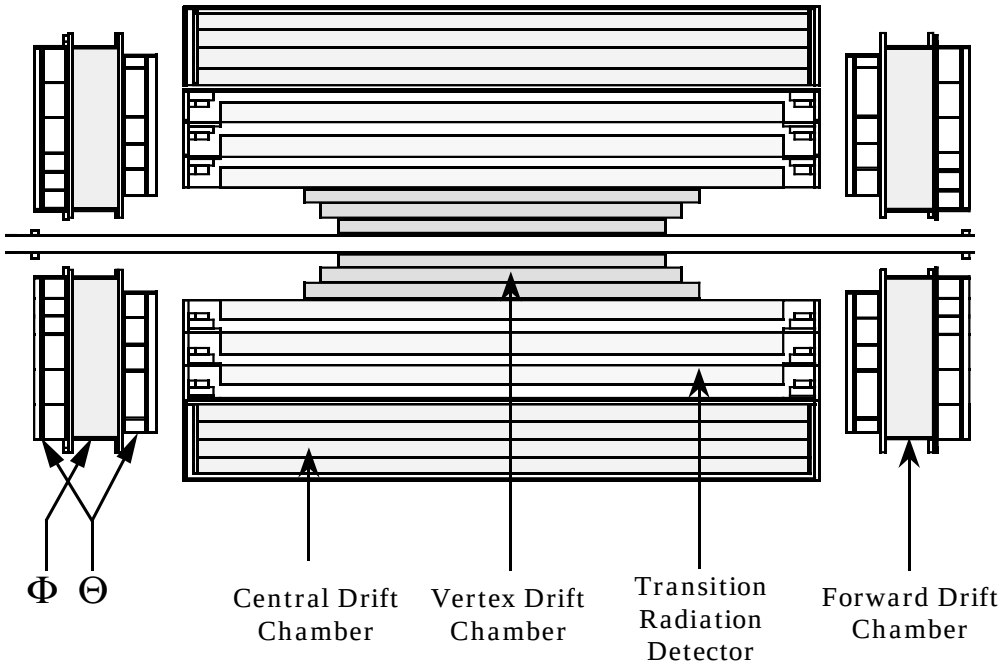

Figure 3.3: The four systems that comprise the central detector.

traverses a gaseous medium it will ionize the gas. An electric field forces the image of the accelerating charge to be deposited on a wire producing a pulse. The orientation of the hits indicates the track for that particle. The central tracker is comprised of four subsystems: the vertex chamber (VTX), the transition radiation detector (TRD), the central drift chamber (CDC), and the forward drift chambers (FDCs). Figure 3.3 shows the components of the central tracker.

The VTX, CDC, and FDC are wire chambers designed to identify the tracks associated with the charged particle. The TRD is designed to discriminate between electrons and hadrons.

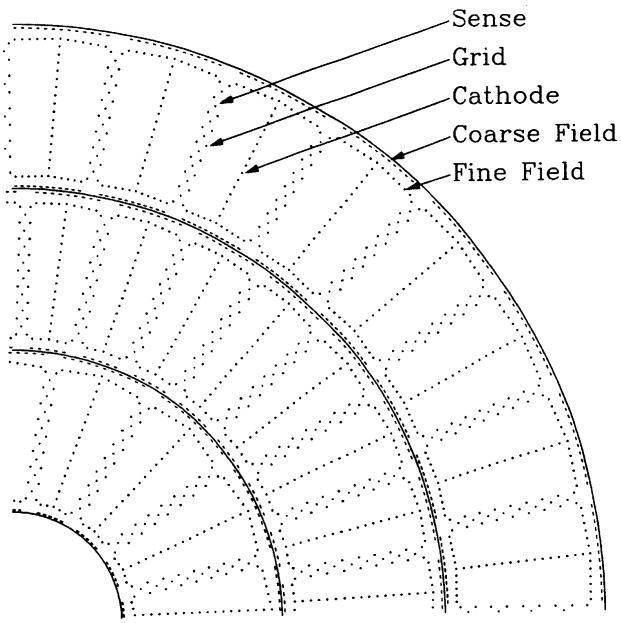

Figure 3.4: R-ϕ view of one quadrant of the VTX chamber.

The Vertex Chamber

The vertex chamber is the innermost tracking device [28]. The chamber occupies a radial distance of 3.7 to 16.2 cm and is approximately 110 cm long. The chamber consists of three concentric layers. The inner layer is divided into 16 cells in ϕ and the outer two layers 32 cells. Figure 3.4 shows the layout of the wires for the chamber. The gas is CO_2(95%)-ethane(5%) with a small amount of H_2O. The water helps to stabilize the detector in a high radiation environment [29].

The Transition Radiation Detector

Since DØ does not have a central magnetic field the transition radiation detector was designed to help distinguish electrons from hadrons. When a highly relativis-

tic particle passes through a boundary with different dielectric constants X-rays are produced [30]. The energy spectrum of the X-rays produced is a function of γ (γ=E/mc^2). The mass difference between the electron and pion allow for the ability to distinguish between the two particles. The TRD has three separate radiators and X-ray detectors arranged in a concentric cylinders beginning outside the VTX and ending inside the CDC. Each radiator is made of 393 foils of 18 μm thick polypropylene immersed in nitrogen gas. The spacing between the foils is 150 μm and is maintained by using a hatched geometry placed on the polypropylene sheets. For this configuration the energy spectrum of the X-rays ranges from 8 keV to 30 keV [31]. Between the radiator and the X-ray detector is at 23 μm gap filled with CO_2 gas to provide a buffer so that the detector gas, Xe(90%)CH_4(7%)C_2H_6(2%), is not contaminated with the radiator gas. The outer layer of the gap is coated with aluminum which provides a high voltage cathode for the detection chamber. Figure 3.5 shows a slice of the TRD. The X-rays produced typically convert in the 15 mm area outside the milar window. The cascade of particles are then amplified in them 8 mm region just inside the 70 μm grid wire.

The full drift time is 0.6 μsec, so the charged that is collected is not only the converted X-rays but also from ionization radiation and delta rays. The magnitude and time of arrival of the charge is used to distinguish between the electrons and pions.

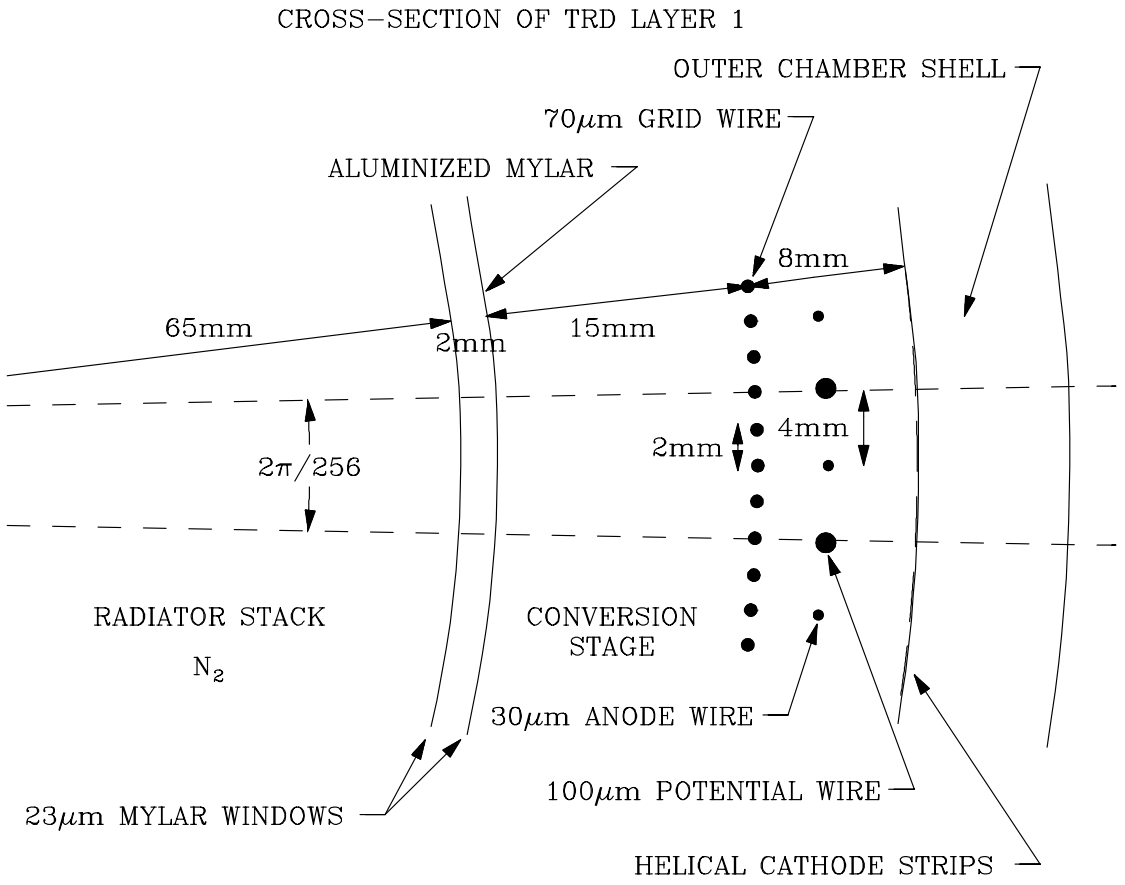

Figure 3.5: A cross section of the TRD.

The Central Drift Chamber

The central drift chamber is a cylindrical device positioned outside the TRD and just before the central calorimeter [32]. Figure 3.6 shows an end view of the central drift chamber. The chamber has a radial dimension of 49.5 to 74.5 cm and is 184 cm long. This covers a pseudo-rapidity range from -1.2 to 1.2. The chamber is composed of four layers each with 32 cells in ϕ. The second and fourth layers are offset by $\frac{2\pi}{64}$ with respect to the first and third layers. The maximum drift distance is $\sim$7 cm. There are 23 wires in each cell: the two outer wires are the delay lines, seven inner

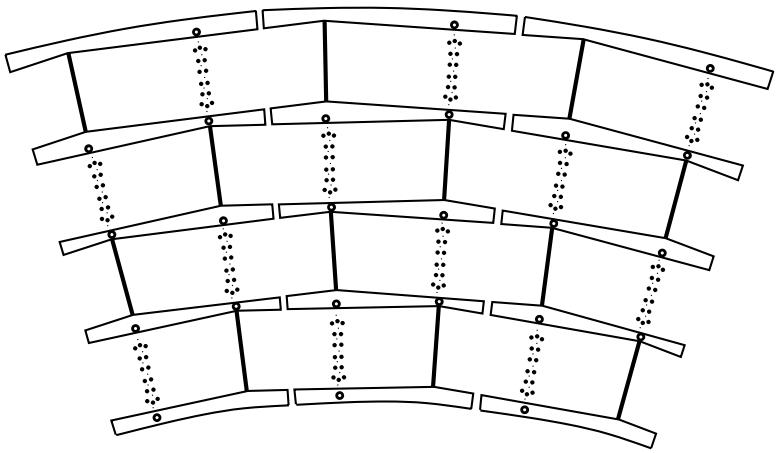

Figure 3.6: R-ϕ view of one quadrant of the CDC chamber.

sense wires, and 14 grounded potential wires. The gold-plated tungsten sense wires are staggered 200 μm in ϕ to resolve left-right ambiguities in the cell. The sense wires are read out at one end of the CDC. The R-ϕ coordinate is determined by the drift time to the sense wires. The delay line is constructed by winding a coil on a carbon fiber epoxy core and is embedded in the cell wall. A signal is induced upon the delay line by the hit on the nearest sense wire. The inner and outermost sense wires have an additional grounded potential wire to minimize the signal from the next nearest sense wire. The delay lines are read out at both ends; the difference in time of arrival of the pulse is used to determine the Z coordinate of the hit. The gas used in the CDC is Ar(92.5%)CH_4CO_2(3%) with 0.5% H_2O. The gain of the gas varies from 2-6x10^4 depending on the location of the sense wire.

The Forward Drift Chamber

The forward drift chambers are located at both ends of the CDC just in front of the forward calorimeters [32, 33]. The FDCs approximately cover a range of $1.4 \leq |\eta| \leq 3.0$. Figure 3.7 shows the exploded view of the three modules for one of the FDC chambers. Two modules give information on the Θ angle and one on Φ. The two Θ chambers are set on either side of the Φ chamber and are offset by $\pi/4$ with respect to one another. The Θ chamber is made up of rectangular cells that increase in length as the radial distance. Each cell has eight sense wires running parallel to the Z direction and normal to the radius and a delay line, of the same type as in the CDC, to measure the position along the cell. The Φ chamber is divided into 36 azimuthal chambers with wires running radially from the beam line. The composition of the gas in the FDC is that same as in the CDC.

3.2.2 The Calorimeter

The calorimeter measures the energy of particles produced during the collision. The DØ calorimeter was designed for the simplicity of calibration, linear compensating response with energy, and good hermeticity [26, 34]. The calorimeter is a pseudo-projective uranium-liquid argon sampling calorimeter. For this geometry the size of a readout pad varies as a function of η. Figure 3.8 shows the pseudo-projective geometry of the DØ calorimeters.

A particle that enters the calorimeter will interact with the absorber and produce a series of secondary particles. There are three different types of absorbers used in the

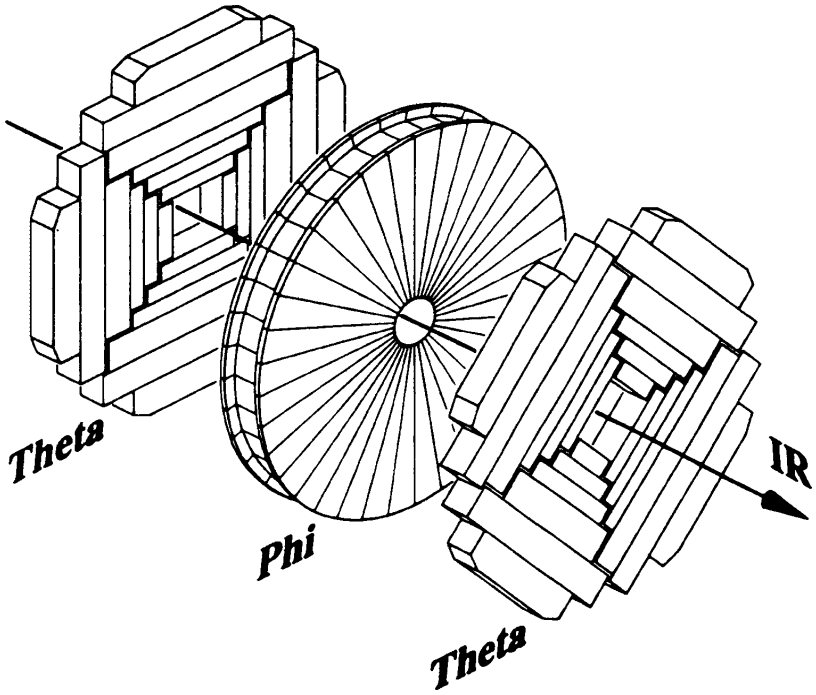

Figure 3.7: Exploded view of one of the forward drift chambers.

calorimeter: uranium, copper, and stainless steel. The secondary particles interact electromagnetically in the active medium, of the liquid argon, producing electrons and ions. A typical calorimeter cell is shown in Figure 3.9. The potential of the absorber plate is kept at ground and the resistive surfaces of the readout board are kept at a positive 2000 V. In the electromagnetic field the ionized particles induce a charge on the readout pads. The electron drift time across the gap is 450nsec. This signal is measured by a preamplifier which sends the information on to the base line subtractor (BLS) which does the analog shaping. One signal is sent to the analogue-to-digital converters (ADCs) where they are converted into energies and another is sent to the trigger framework. If a signal is within 2σ of the pedestal value it is not

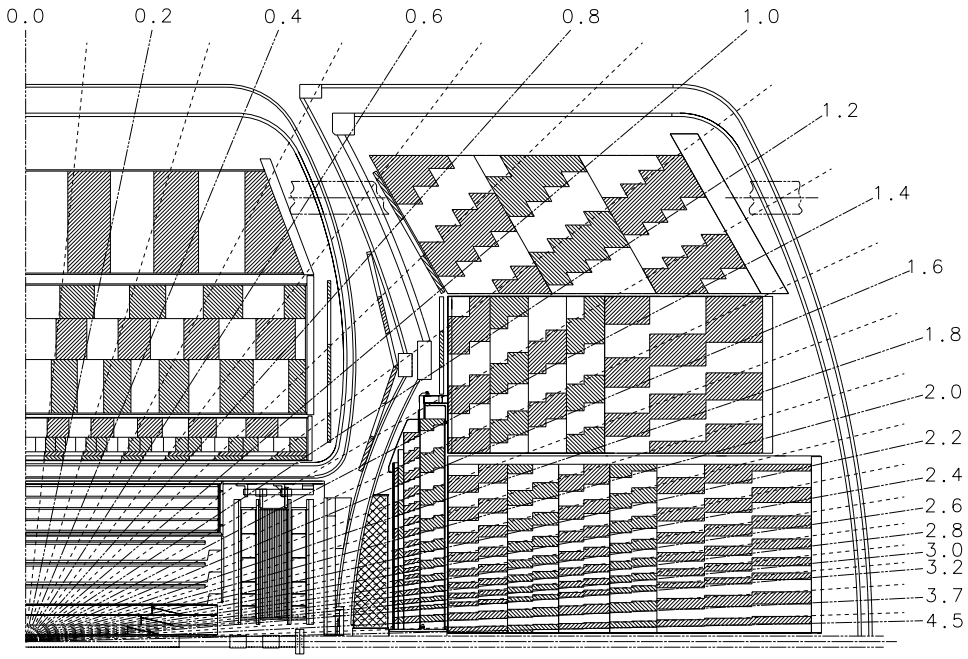

Figure 3.8: One quadrant of the DØ calorimeter and tracking system.

read out. This zero-suppression reduces the number of calorimeter channels read out from 50,000 to 5,000 per event.

The DØ calorimeter has three different cryostats. The end calorimeter south (ECS) covers a range of $1 \leq \eta \leq 4$, the end calorimeter north (ECN) covers a range of -4 $\leq \eta \leq$ -1, and the central calorimeter (CC) covers a range of $|\eta| < 1$.

The CC is composed of three types of modules. Outward, away from the beam-line, they are: the electromagnetic (CCEM), the fine hadronic (CCFH) and the coarse hadronic (CCCH). The CCEM has four longitudinal layers of approximately

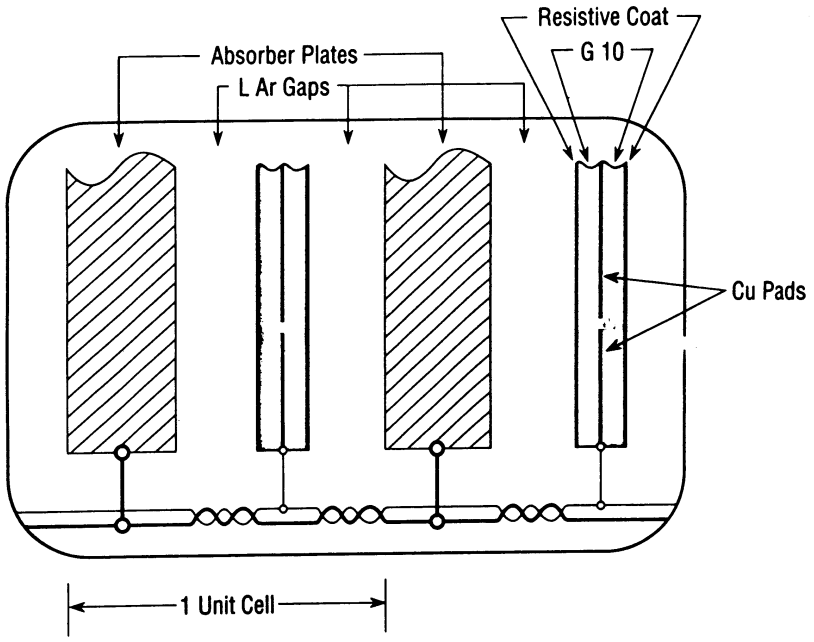

Figure 3.9: Schematic view of a typical uranium liquid argon readout cell.

2.0, 2.0, 6.8, and 9.8 radiation lengths (X_0) respectively. The number of interaction lengths (λ_A) for the CCEM is 0.76. The CCEM is characterized by relatively thin uranium plates of 0.3-0.4 cm. Layers 1, 2, and 4 have an $\eta \times \phi$ segmentation of 0.1×0.1. Layer 3 has an $\eta \times \phi$ segmentation of 0.05×0.05. For an electromagnetic object layer 3 is where the maximum shower deposition occurs so the finer $\eta \times \phi$ segmentation improves the position resolution. The CCEM layer 3 is located $\sim$90 cm radially from the beamline. The CCFH and CCCH have an $\eta \times \phi$ segmentation of 0.1×0.1. The CCFH has three longitudinal layers of 1.3, 1.0 and $0.9\lambda_A$. The CCFH plates are fabricated from a uranium-niobium(2%) alloy and are 0.6 cm thick. The CCCH has only one layer of $3.2\lambda_A$ composed of 4.7 cm thick plates.

The ECs are composed of four types of modules. They are the electromagnetic (ECEM) [35] , the inner hadronic (ECIH), the middle hadronic (ECMH), and the outer hadronic (ECOH). Figure 3.8 shows the different module types for the end calorimeter. The ECEM is composed of uranium disks which range from 5.7 cm to a radius of 84 to 104 cm. The ECEM has four readout layers of 0.3, 2.6, 7.9, and $9.3X_0$. The material in front of the first layer increases the number radiation lengths to $\sim$2. Like the CCEM, the third layer of the ECEM has a finer $\eta \times \phi$ segmentation than the rest of the layers in the EC. The ECIH modules are cylindrical disks of radii 3.92 to 86.4 cm. The fine hadronic portion of the ECIH contains four readout layers of $1.1\lambda_A$ each. The coarse hadronic is built from stainless steel plates and has a single readout with $4.1\lambda_A$. The ECMH has four fine hadronic sections of $0.9\lambda_A$ and a stainless steel coarse hadronic section of $4.4\lambda_A$. The stainless steel plates of the ECOH are tilted 60° with respect to the beam axis.

The region between the central and forward cryostats is instrumented with scintillating tiles. The intercryostat detectors (ICDs) [36] are attached to the front surface of the EC. The tiles have an $\eta \times \phi$ segmentation of 0.1×0.1 to match the cell size in the calorimeter. The tiles are made from Bicron BC-414 scintillator and are read out with 2 mm bundles of wave shifting fiber. The relative gain of the photomultipliers is maintained by pulsing the scintillator with an ultra-violet laser. Additionally, scintillator is mounted on the face of the CCCH, the ECMH, and ECOH to provide additional calorimetry and are refered to the the massless gaps. The result of inclusion of these tiles is to improve the $\not\!\!E_T$ resolution since the energy of the particles

entering this region would otherwise be lost.

3.2.3 The Muon Spectrometer

The DØ muon system consists of three layers of proportional drift tubes (PDTs) along with five toroidal magnets to measure momentum. The central toroid (CF) covers a region of $|\eta|<1$ and two forward toroids (EF) covering from $1\leq|\eta|\leq2.5$. Collectively, they are referred to as the wide angle muon system (WAMUS). The PDTs near the beam pipe are referred to as the small angle muon system (SAMUS) and cover the region from $2.5\leq|\eta|\leq3.6$.

Figure 3.2 shows the three layers of PDTs and the toroids of the WAMUS system. The three layers of WAMUS chambers are labeled A, B, and C. The A layer is inside the toroid and is composed of four layers of cells. The B and C layers are outside the toroid and have only three layers of cells. The B and C layers are separated by 1m allowing for a good measurement of the direction after the muon has passed through the magnet. A PDT cell is composed of a diamond shaped cathode pad on top and bottom and a gold-plated tungsten anode wire. The period of the diamond pattern is 60.9 cm. The aluminium PDT is kept at ground while the cathode pad and anode wire are kept at +2.3 kV and +4.56 kV respectively. Determining where the hit occurred along the anode wire is a two step process. In order to give access to the muon electronics the anode wires for adjacent calls are jumpered together. The difference in time of arrival of the signal gives a rough estimate of the position along the wire. Using the cathodes, the sum and difference of the charge on the inner and

outer pads can be used to find the position within 0.3 cm.

The SAMUS system is composed to three layers of drift tubes. Each layer is composed of three sub-layers where the sub-layer is composed of two layer of tubes offset by half their width. The doublets are then rotated with respect to one another. The tubes are 3 cm in diameter and have a single anode wire.

The drift time of a PDT can take up to 1.2 μsec. The Fermilab upgrade will increase the number of bunches in the Tevatron from 6 to 36 decreasing the bunch crossing time to 0.396 μsec. In order to identify which interaction the muon came from a fast muon timing tag is required. A layer of scintillating counters has been built to do this. The scintillator covers the region outside the C layer of PDTs for $|\eta|<1$ and all of ϕ except the region from 225-315°. Each counter is 25in wide and 81.5 to 113in long. The light from the $\frac{1}{2}$in thick scintllator is propogated to photomultiplier tubes by 1 mm diameter optical fiber. The counters were used during Run 1b in the trigger and as a cosmic veto. See Appendix A.1 for more details on the muon scintillator.

3.2.4 Triggering

At DØ triggering is the filtering of specific signals from a large number of less interesting interactions. Most interactions occurring at DØ are uninteresting low transverse momentum events. The DØ trigger has four levels of filtering to decide which events should be kept and written to magnetic tape. The four levels of triggering are called level 0, 1, 1.5, and 2. The first three levels of triggering are done by dedicated

hardware whereas the fourth level is a software trigger.

Level 0 is designed to look for the break up of the proton and anti-proton. It consists of two scintillator hodoscopes mounted on the forward calorimeters. The detector is composed of two layers of rectangular scintillator and are readout with photomultiplier tubes. The coverage in $|\eta|$ is 1.9 to 4.3 but because of the rectangular geometry the ϕ coverage is not uniform. By comparing the difference in the time of arrival of the hits in the two hodoscopes a Z vertex for the interaction can be determined. This vertex is then available for p_T calculations in the subsequent trigger levels. The efficiency of level 0 is >98% [38].

The level 1 trigger has two components; muon and calorimeter. For more information on the muon trigger see reference [37]. The level 1 calorimeter trigger is a hardware trigger which uses information taken from the BLS cards. The job of the level 1 trigger is to reduce the input rate of ~200 kHz from level 0 to an output rate of ~200 Hz. The trigger tower, the region in which trigger decisions are based, is at level 1 a 0.2×0.2 in $\eta\times\phi$ region out to an η of 4. The electromagnetic (EM) and fine hadronic (Had) energy for each tower is available for decision making. A number of global quantities are then calculated and can be used to trigger. Level 1 can also make decisions using only the individual tower transverse energies [37]. If the level 1 criteria is satisfied then an event may be passed directly to level 2 or sent on to level 1.5 for further evaluation.

Level 1.5 uses the information available at level 1 but then clusters the two highest energy towers into a single object. These towers can only be clustered along the η

or ϕ direction. For level 1.5 the transverse energy ($E_T^{L1.5}$) and EM fraction ($f_{em}^{L1.5}$) are calculated from equations 3.1 and 3.2.

$$E_T^{L1.5} = \sum_{\mathrm{i}=1}^{2} \mathrm{E_i(EM)} \sin \Theta_\mathrm{i} \tag{3.1}$$

$$f_{em}^{L1.5} = \sum_{\mathrm{i}=1}^{2} \frac{\mathrm{E_i(EM)}}{\mathrm{E_i(EM) + E_i(Had)}} \tag{3.2}$$

Where Θ_i is the polar angle defined by the Z vertex and the center of the i^{th} 2×2 tower. If $E_T^{L1.5}$ and $f_{em}^{L1.5}$ pass certain thresholds the event is sent to level 2.

The level 2 trigger is a software trigger where information for the entire detector is available to make trigger decisions. Level 2 has a farm of processors which run software tools to identify electrons, muons, jets,...etc, in the event. This information is then used to select whether or not the event is kept and written to tape. The energy of the electron candidate taken from the region $\eta \times \phi$, equal to 0.3×0.3, about the highest E_T tower from Level 1. An electron is identified from the shower shape, electromagnetic fraction, and isolation. The transverse shape is based on the difference in energies in the regions 0.25×0.25 and 0.15×0.15. The isolation (f_{iso}^{L2}) condition is given by

$$f_{iso}^{L2} = \frac{E(0.4) - E}{E} \tag{3.3}$$

$$< 0.15 \tag{3.4}$$

where $E(0.4)$ is the energy in a cone of radius ($\mathcal{R}$) equal to 0.4 and E is the energy of the electron candidate. The rate at which the event is written to tape is 2-4 Hz. The

events are then sent offline where a more thorough reconstruction program produces the events used in the physics analysis.

Chapter 4

Event Selection

4.1 Overview

The Tevatron Run 1 took place over a period of three years from late 1992 to early 1996. The run was broken up into three distinct periods given the labels 1a, 1b, and 1c. The data for this analysis were taken during the Tevatron Run 1b from February 1994 to April 1995. The integrated luminosity over this period was 76 pb^{-1} which is approximately 6 times the amount of data collected during Run 1a. Figure 4.1 shows the integrated luminosity as a function of the date. The difference between the delivered and recorded luminosity is due to a beam that was not suitable for data taking or detector problems.

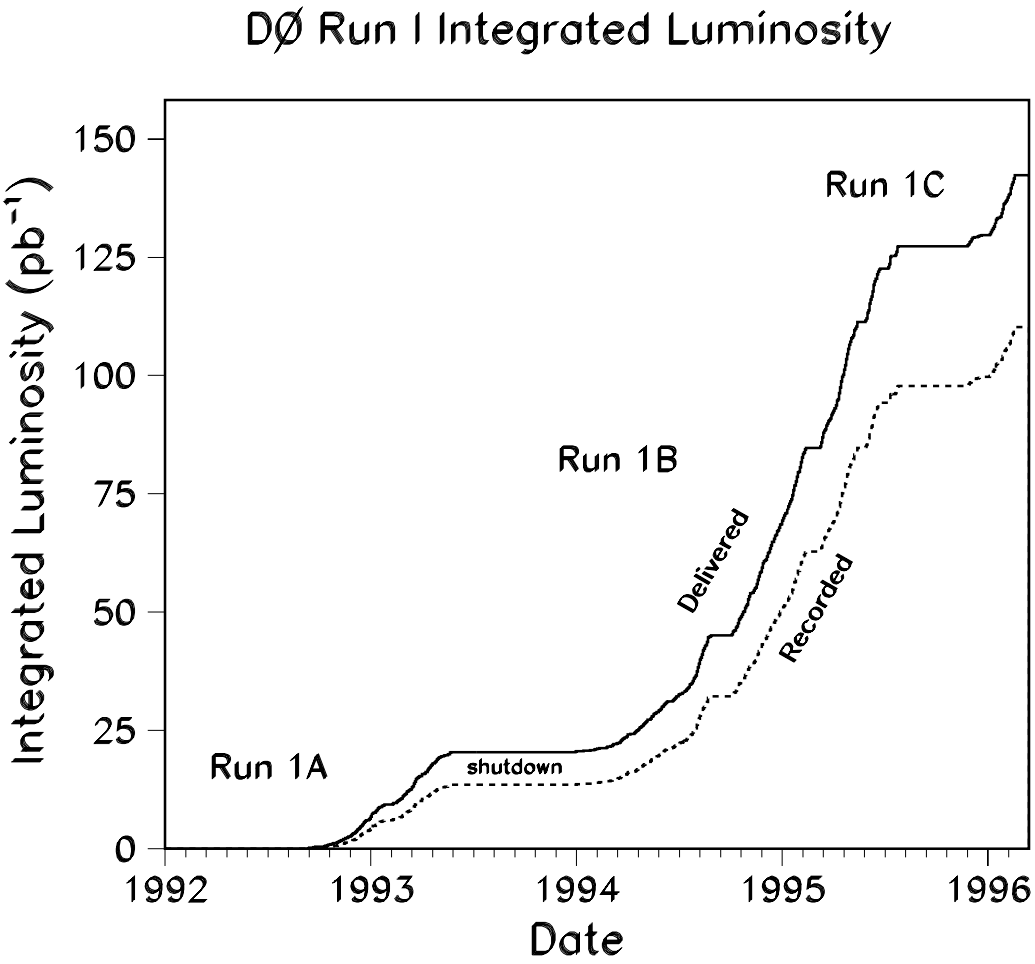

Figure 4.1: The Run 1 integrated luminosity as a function of time.

4.2 Defining the Observables

The observables in a $W(Z)$ boson event are the event vertex, the electron(s) position and momentum, and the recoil transverse momentum. An electron is defined to be a deposition of energy in the electromagnetic portion of the calorimeter along with an associated track in the tracking chamber. The electron energy cluster is required to pass some loose shower shape cuts and an electromagnetic fraction (f_{em}) cut. The energy of the electron is the sum of the cells in a $\eta \times \phi$ region equal to 0.5×0.5 in the first five layers (EM1, 2, 3, 4, and FH1) of the calorimeter. This region is called a 5×5 *window* and covers approximately a 2500 cm^2 region of the detector. The depth of the five layers is $\sim 40 X_0$. The f_{em} is the ratio of the energy in FH1 to the total energy in the window. The electron centroid $\vec{x}_c$=$(X_{Elc}, Y_{Elc}, Z_{Elc})$ is calculated from

$$\vec{x}_c = \frac{\sum_i w_i \vec{x}_i}{\sum_i w_i} \tag{4.1}$$

where the sum runs over all the cells of the electron and $\vec{x}_i$ is the location of the center of the i^{th} cell. The weights are given by

$$w_i = \max\left(0, w_0 + \ln\left(\frac{E_i}{E}\right)\right) \tag{4.2}$$

and E_i is the energy in the i^{th} cell in EM3, E is the energy of the cluster, and the weight w_0 is chosen to minimize the resolution. The motivation for the log weighting is given in reference [39]. Small corrections are made to Z_{Elc} to correct for biases observed in the DØGEANT [40] Monte Carlo simulation of electrons [41].

The event vertex Z position (Z_V) is calculated from the electron centroid and the center of gravity (COG) of the associated track, $\vec{x}_t$=($X_{Trk}, Y_{Trk}, Z_{Trk}$). It has been found that a bias exits in the measured Z position (Z_{Trk}^{Meas}) determined by the CDC. The CDC Z_{Trk} has been calibrated using cosmic ray and collider muons [42, 43] and is given by the following function

$$Z_{Trk} = S_{CDC} Z_{Trk}^{Meas} + \beta_{CDC}. \tag{4.3}$$

where the scale (S_{CDC}) is 0.988$\pm$0.002 and β_{CDC} is consistent with zero.

The vertex is given by

$$Z_V = Z_{Trk} - \frac{R_{Trk}}{R_{Elc} - R_{Trk}} (Z_{Elc} - Z_{Trk}) \tag{4.4}$$

where $R_a = \sqrt{(X_a - X_V)^2 + (Y_a - Y_V)^2}$ and $a = \{Trk, Elc\}$. The vertex is determined with this method because when several interactions occur during a beam crossing the vertexing algorithm cannot distinguish between two vertices when they are less than 10 cm apart. The COG method has poorer resolution then the conventional method of finding the vertex but has the virtue of being independent of the instantaneous luminosity at which the event was observed. The (X_V, Y_V) position of the vertex is measured by the VTX. Given this information the electron vector components are given by

$$E_x = E \sin\theta \cos\phi \tag{4.5}$$

$$E_y = E \sin\theta \sin\phi \tag{4.6}$$

$$E_z = E\cos\theta \tag{4.7}$$

where

$$\tan\phi = \frac{Y_{Elc} - Y_V}{X_{Elc} - X_V} \tag{4.8}$$

$$\tan\theta = \frac{R_{Elc}}{Z_{Elc} - Z_V} \tag{4.9}$$

and the magnitude of the electron transverse momentum is written as $E_T = E\sin\theta$.

The recoil momentum of the $W(Z)$ boson is calculated by summing over all the calorimeter cells except for the cells occupied by the electron(s). The components of the recoil vector are

$$p_x^R = \sum_i E_i \sin\theta_i \cos\phi_i \tag{4.10}$$

$$p_y^R = \sum_i E_i \sin\theta_i \sin\phi_i \tag{4.11}$$

where E_i is the energy in the i^{th} cell and θ_i and ϕ_i are the angles determined with respect to the vertex and the center of the i^{th} cell. For a W boson event, given the recoil momentum ($\vec{p}_T^R$) and electron vector ($\vec{p}_T^e$), the neutrino transverse momentum ($\vec{\not{p}}_T$) is inferred by

$$\vec{\not{p}}_T = -\left(\vec{p}_T^e + \vec{p}_T^R\right) \tag{4.12}$$

and magnitude of the neutrino vector is written as $\not{E}_T$. The transverse momentum of the W boson event is defined to be equal to the negative of the recoil vector.

There are some convenient variables used to describe W and Z boson events. Figure 4.2 shows the variables $U_{||}$ and $U_{\perp}$ which are defined as

$$U_{||} = \frac{\vec{p}_T^{\,R} \cdot \vec{p}_T^{\,e}}{\mid \vec{p}_T^{\,e} \mid} = \mid \vec{p}_T^{\,R} \mid \cos \phi^{e,R} \quad (4.13)$$

$$U_{\perp} = \mid \vec{p}_T^{\,R} \mid \sin \phi^{e,R}. \quad (4.14)$$

$U_{||}$ is the projection of the recoil along the electron transverse direction and $U_{\perp}$ is the projection of the recoil perpendicular to this axis. If $U_{||}$ has a large negative value then the recoil is away from the electron and the electron is boosted. If the $U_{||}$ is large and positive the recoil is near the electron and the neutrino gets the boost. Figure 4.3 shows a useful way of defining the variables in a Z boson event. The η axis is the bisector of the electrons in the transverse plane and the ξ axis is perpendicular to the η axis. The η axis is used because it minimizes the sensitivity to the electron resolution.

4.3 Event Selection

The W and Z boson candidates are selected with a trigger according to their kinematic properties. A W boson is identified by a high p_T electron and significant missing transverse energy, and a Z boson by two high p_T electrons. The offline selection is simply refinements of these basic criteria.

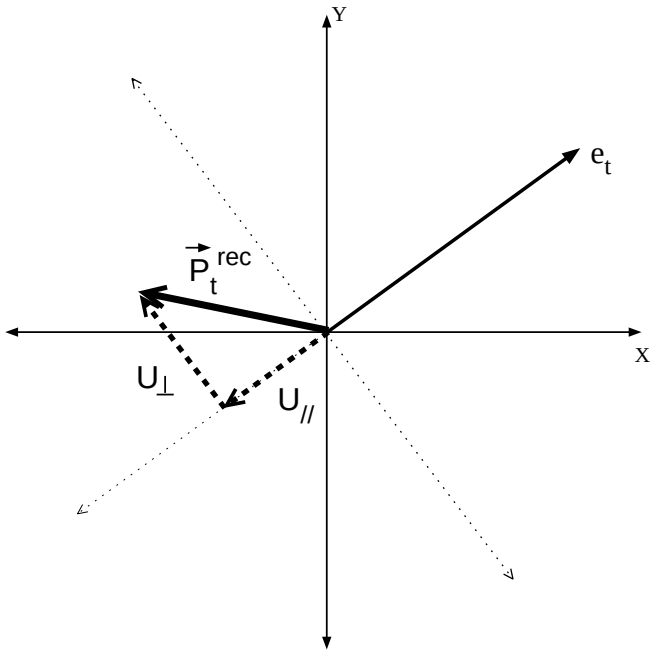

Figure 4.2: Definition of $U_{||}$ and $U_\perp$.

4.3.1 Triggering

Z Boson Events

The trigger framework first requires a Z boson candidate fire the Level 0 trigger, i.e. the breakup of the proton and antiproton is observed. The Level 1 trigger, EM_2_MED, requires two electromagnetic objects with E_T >7 GeV. This candidate is then passed to the Level 1.5 trigger framework which requires that one of the objects pass an E_T >10 GeV cut. The Level 2 trigger, EM2_EIS2_HI, selects two isolated electromagnetic objects with E_T >20 GeV. Also, Level 2 requires that the clusters have longitudinal and transverse shower shape consistent with electrons from the testbeam. If the candidate passes these criteria it is written to magnetic tape.

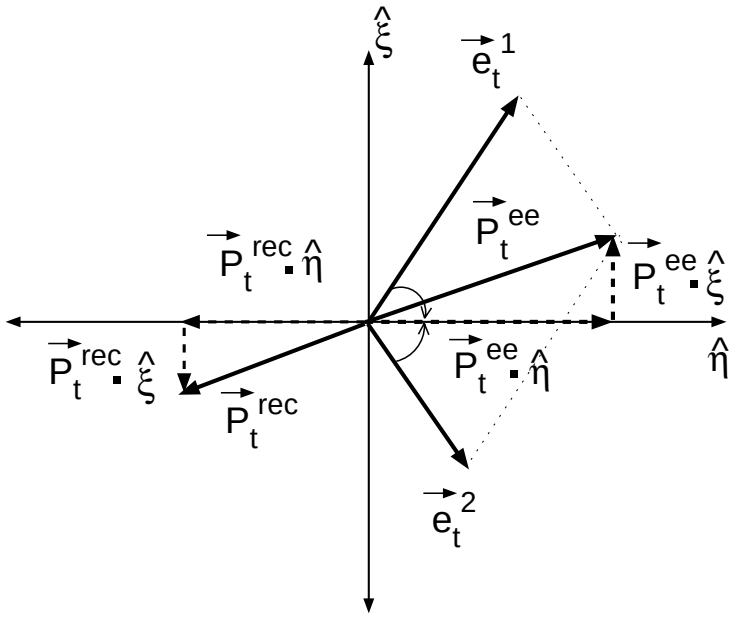

Figure 4.3: Definition of the useful axis and projections in a Z boson event. The η axis is the bisector of the electrons in the transverse plane and the ξ axis is perpendicular to the η axis.

W Boson Events

The trigger conditions for the W boson did *not* require a Level 0 to have fired. This was to allow for the study of diffractive W boson events. The first trigger requirement for a W boson candidate was a Level 1 trigger, EM_1_HIGH, which required one electromagnetic object with E_T >10 GeV. Level 1.5 then required the Level 1 object pass an E_T cut of 15 GeV. The Level 2 trigger, EM1_EISTRKCC_MS, required one electromagnetic object with E_T >20 GeV and $\not\!\!E_T$ >15 GeV. The same isolation and shower shape cuts were required on the W boson electron as on the Z boson electrons.

4.3.2 Offline Selection

The final selection of W and Z boson events involves a combination of kinematic, fiducial, electron quality, and detector status cuts.

Kinematic

The kinematic cuts for the W boson events are:

- E_T >25 GeV
- $\not\!\!E_T$ >25 GeV
- p_T^W <30 GeV/c

and the Z boson events:

- $E_T^{1,2}$ >25 GeV .

Fiducial

The fiducial cuts are used to ensure the electron(s) are measured in a part of the calorimeter that has good response. This means cutting away from edges, cracks, and regions of low response. There are two fiducial cuts for electrons in the central calorimeter (CC):

- The absolute value of Z_{Elc} must be less than 107.7 cm which is equivalent to an $|\eta_{Det}|$<1.0 cut where η_{Det} is the detector eta.

- The ϕ of the track may not point to within 10% of a CC ϕ module boundary.

The forward calorimeters (ECs) do not have ϕ cracks so the fiducial cut selects electrons in the region $1.4<|\eta_{Det}|<2.6$.

Electron Quality

The electron quality cuts are designed to reject background while maintaining a high efficiency for electrons. The quality cuts used are the isolation, a cluster shape variable, the electromagnetic fraction, and the track match. The isolation is defined as

$$f_{iso} = \frac{E(0.4) - EM(0.2)}{EM(0.2)} \tag{4.15}$$

where $E(0.4)$ is the total energy in a cone of radius ($\mathcal{R}$) equal to 0.4 and EM(0.2) is the electromagnetic energy in a cone $\mathcal{R} = 0.2$. This cut is independent of the electron location and is $f_{iso} < 0.15$. Also, the electrons are required to have $f_{em} > 0.9$.

A covariance matrix is used to define a variable (χ^2) which measures how consistent the shower shape is to that expected from an electron [44]. The Monte Carlo electrons used to generate the matrix were tuned on test beam electrons. There are 41 variables used in the covariance matrix: the energy fractions in EM1, EM2, EM4, and in a 6×6 grid centered around the highest energy cell in EM3, the log of the total energy, and the vertex position divided by the RMS of vertex distribution. Table 4.1 lists the value of χ^2 cut depending on the location of the electron.

Parameter	CC Value	EC Value
χ^2	< 100	< 200
σ_{Track}	< 5	< 10

Table 4.1: Electron quality cuts in the different cryostats.

The track match significance (σ_{Track}), or just track match, is a measurement of how well the track matches to the electron position. The track direction is extended into the calorimeter and a three dimensional match is performed to the cluster position. The track match is defined as

$$\sigma_{Track} = \frac{\Delta R\phi}{\sigma_{R\phi}} \oplus \frac{\Delta Z}{\sigma_{\Delta Z}} \tag{4.16}$$

where $\Delta R\phi$ is the difference between the track and the cluster in the $R-\phi$ plane, $\sigma_{R\phi}$ is the resolution of the $R\phi$ difference, ΔZ is the difference between the cluster and the track at the nearest point in the $R-Z$ plane, and $\sigma_{\Delta Z}$ is the resolution of ΔZ. Table 4.1 lists the value of track match cut depending on the electron location.

Detector Status

The components of the detector are required to be in good working in order for the event to be allowed into the data sample. If any detector component was not in good working order during a run, the run was flagged as a BADRUN. Any run that is selected as a BADRUN is removed from the sample.

During a run there are times when the accelerator affects the detector. The largest effect is due to the Main Ring when it is in the production of antiprotons.

The Main Ring passes through one of the coarse hadronic modules of the calorimeter. If protons are lost from the Main Ring they may end up depositing energy in the calorimeter. Since the $\not\!\!E_T$ is the sum of all cells in the calorimeter any energy from the Main Ring will bias this quantity. There are two cases when the Main Ring is flagged for affecting the detector.

The first is MRBS (Main Ring Beam Sync.) loss and occurs when the protons are first injected into the Main Ring and is accelerating the protons to the working energy of 120 GeV. The proton losses during this time are large and result in the calorimeter being sprayed with particles. When this happens a flag called the MRBS loss bit is set to true.

The second case is after MRBS and the protons are circulating in the Main Ring. If the protons in the Main Ring are passing through the detector at the same time as when the Tevatron beam is colliding at DØ another bit is set called the μBLANK. These two effects result in a loss of 20% of the available luminosity!

Any W boson candidate that has either the μBLANK or the MRBS loss bit set is removed from the data sample. For the Z boson events the event may be kept depending on what analysis is being performed. If a Z boson event is being used to study the electrons then the μBLANK or the MRBS loss cuts are not made. If the event is being used to study the hadronic portion of the event then the event is removed.

The final selection criteria is to require that the Level 0 trigger have fired. This forces the W and Z boson events to have similar trigger conditions.

Topology	Number of Events		
	Total	**70< $M(ee)$ <110 GeV/c^2**	**μBLANK, MRBS**
CC-CC	1562	1470	1323
CC-ECS	772	733	637
CC-ECN	776	728	656
ECS-ECS	302	251	260
ECN-ECN	344	291	294

Table 4.2: Number of Z boson events for the different topologies where the second column is all events passing the selection criteria, the third column restricts to the invariant mass region 70-110 GeV/c^2, and the fourth column removes events where the μBLANK or MRBS loss bit was set.

Topology	Number of Events	
	Total	**60< m_t <90 GeV/c^2**
CC	32856	27040
ECS	12041	9557
ECN	12629	9881

Table 4.3: Number of W boson events for the different topologies where the second column is the total number of events and the third column is the number of event in the transverse mass window 60-90 GeV/c^2.

4.4 The Data Sample

The number of Z boson events that pass the cuts in section 4.3 are listed in table 4.2. Table 4.3 lists the number of W boson events which pass the cuts in section 4.3. Figure 4.4 shows the electron E_T, $\not\!\!E_T$ and m_t for the CC W bosons and the invariant mass distribution for the Z boson CC-CC events. Figure 4.5 shows the lego plot for a W boson event. This is a W boson candidate because there is one high p_T isolated electron and large missing p_T. The lego plot involves slicing the calorimeter along the ϕ direction and displaying the transverse energy in a given area as the height

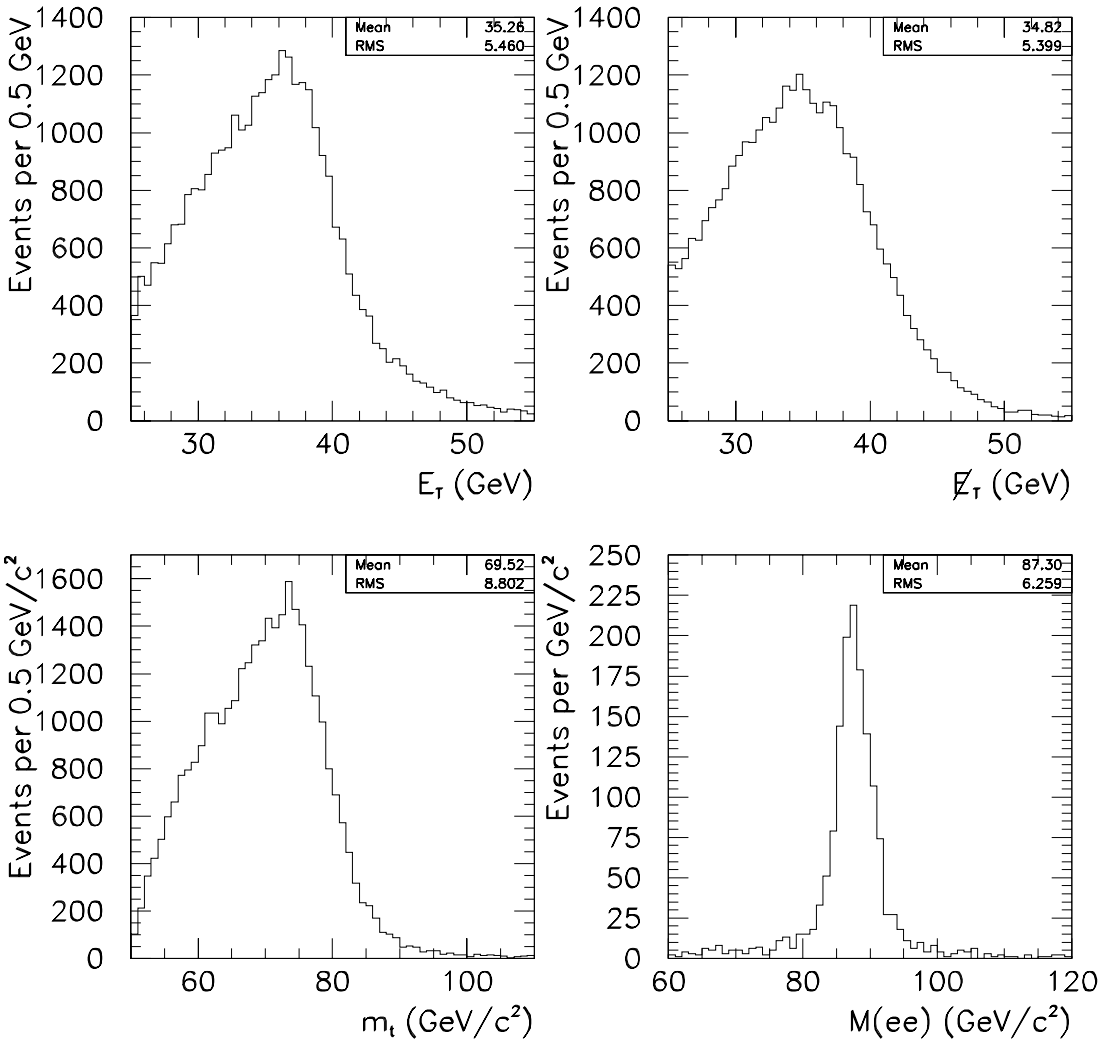

Figure 4.4: The E_T, $\not\!\!E_T$, and m_t distributions for the CC W boson events and the invariant mass distribution for the CC-CC Z boson events passing the selection criteria.

of the tower. Observe that in figure 4.5 that there is one energetic electromagnetic object and very little other energy elsewhere in the event. Figure 4.6 is a display of the electron in figure 4.5 where energy in the first four layers of the calorimeter is displayed. At the bottom of figure 4.6 is shown the energy deposition in the first five layers of the calorimeter and on the left side of the figure is displayed various quantities associated with the electron. The electron in figure 4.5 is shown as an example of a well isolated electron. Figures 4.7 and 4.8 show an example of an electron that passes the selection criteria but has an isolation value near the cut. One can see this is not a well isolated electron from the energy surrounding the electron, see figure 4.7. Figure 4.9 shows the lego plot of a Z boson event.

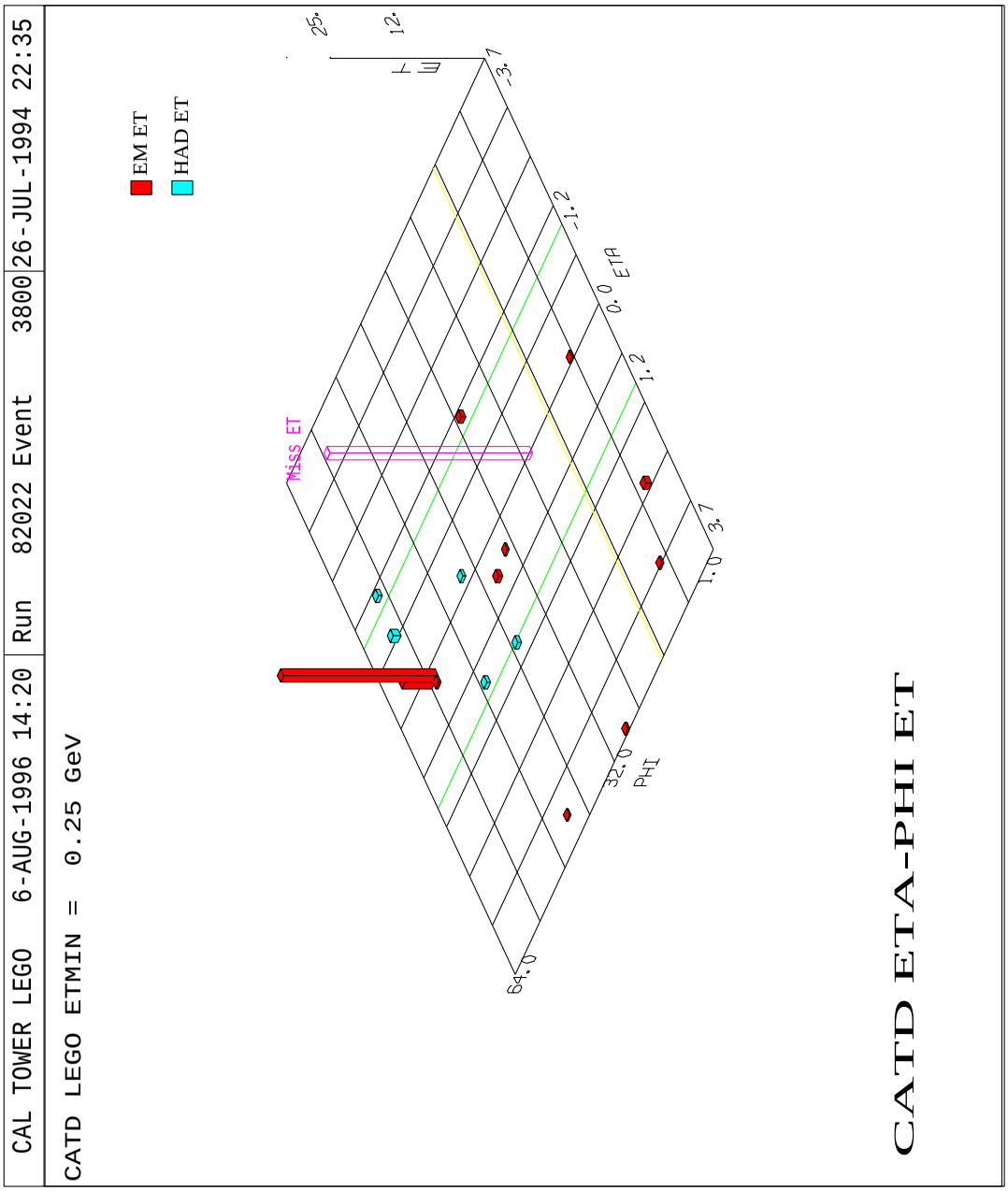

Figure 4.5: The lego plot of a W boson event where the electron is well isolated. The cone in which the electron is isolated extends from the center of the electromagnetic cluster out two-thirds of a grid width.

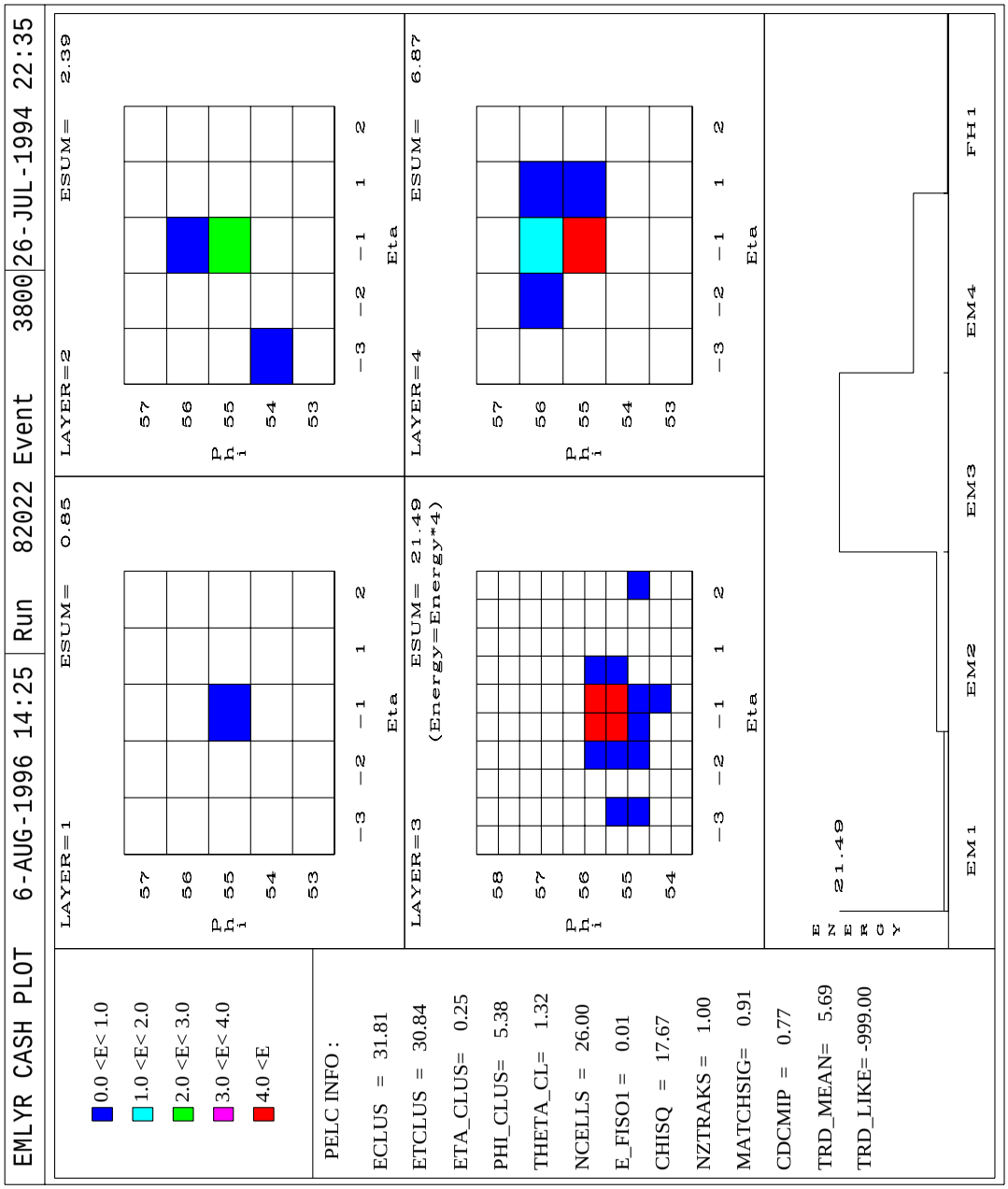

Figure 4.6: A display of the electron in figure 4.5 showing the deposition of energy and various electron parameters.

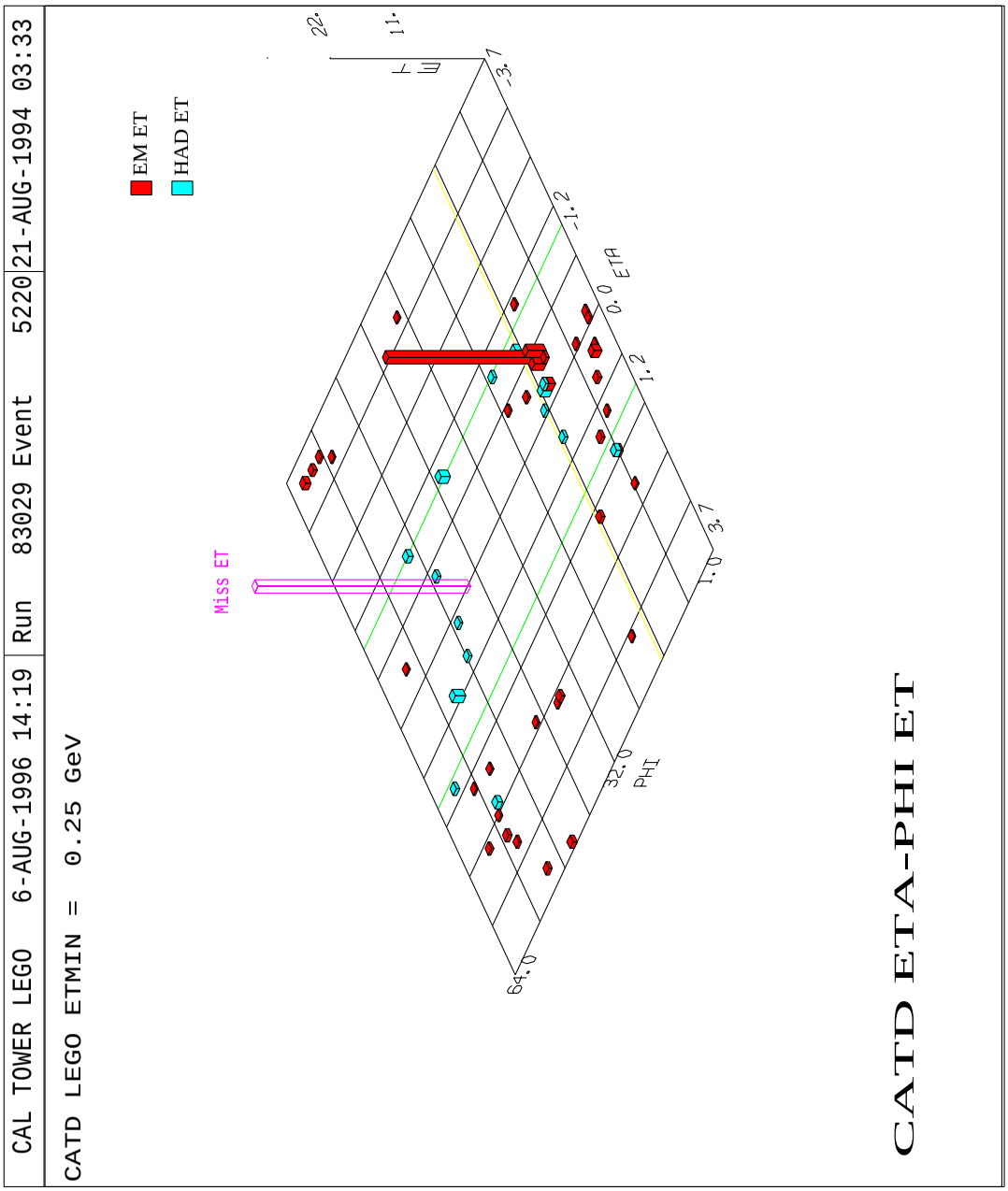

Figure 4.7: The lego plot of a W boson event where the electron is not well isolated.

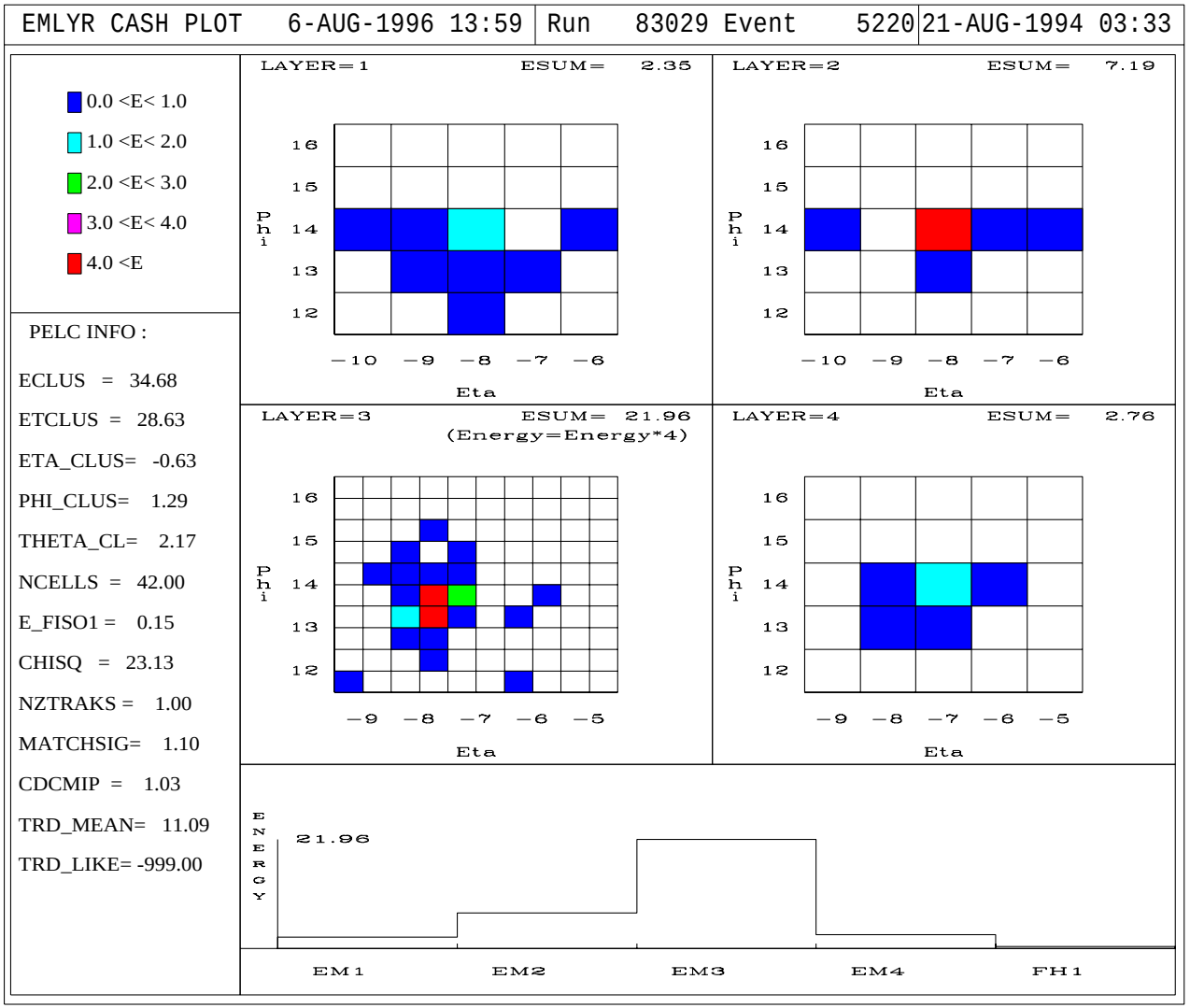

Figure 4.8: A display of the electron in figure 4.7.

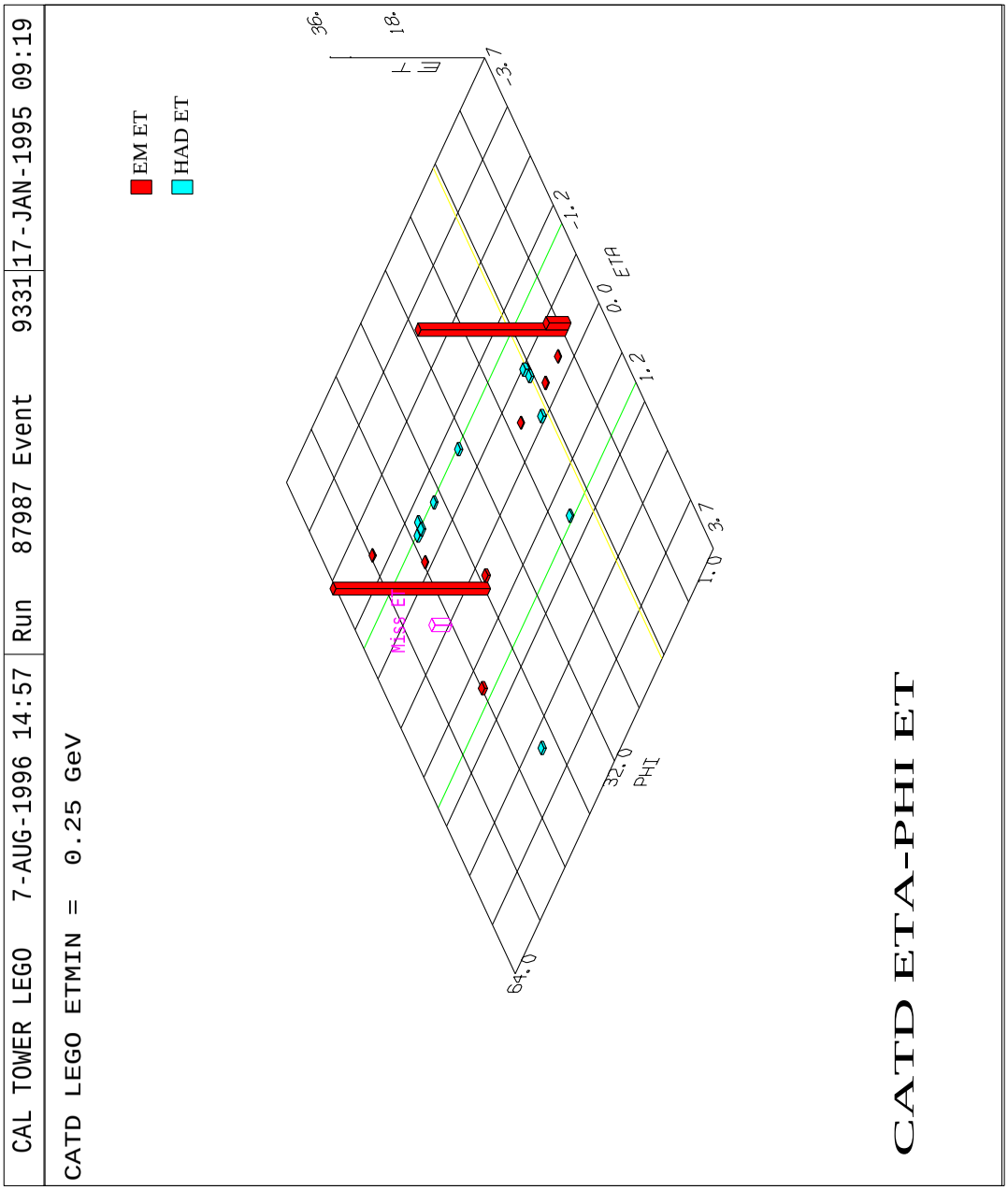

Figure 4.9: A lego plot of a Z boson event where both electrons are in the central calorimeter.

Chapter 5

The Monte Carlo

5.1 The W and Z Boson Event Generator

The W boson mass is measured by performing a maximum likelihood fit to the transverse mass distribution. Other kinematic variables such as the E_T, $\not\!\!E_T$, and E may also be used to measure the mass but each suffers from systematic or statistical errors that make that measurement less precise. The transverse mass does not have a simple analytical form, therefore a Monte Carlo is used to provide transverse mass lineshapes as a function of the W boson mass. The CMS (Columbia-Michigan State) Monte Carlo was written for this purpose. It was designed to be fast and easily modifiable. The CMS Monte Carlo had its origins in the fast Monte Carlo used for the Run 1a W boson mass measurement [45] but significant modifications were made due to the luminosity dependences found in Run 1b and general improvements in the algorithm.

The final W boson mass quoted is a measurement of the ratio of the measured W and Z boson masses. The CMS Monte Carlo generates both the W and Z boson in the same program to be certain that each is treated in the same manner. The final W boson mass is given by

$$M_W = \left(\frac{M_W}{M_Z}\right)_{D\emptyset} \cdot M_Z^{LEP} \tag{5.1}$$

where M_Z^{LEP} is the world average Z mass [14]. The ratio measurement has the virtue that many cancelations occur which reduce the systematic error. The major drawback is that the measurement has a large error due to the statistical error on the Z boson.

5.2 The Physics

The Monte Carlo simulates the production and decay of $W \rightarrow e\nu$ and $Z \rightarrow ee$ events. The following sections discuss the production of W bosons but is also valid for the generation of Z bosons. Any differences in the algorithm will be pointed out.

5.2.1 $p\overline{p} \rightarrow W \rightarrow e\nu$

The triple differential cross section $p\overline{p} \rightarrow W$ completely defines the production of the W boson. The theoretical model implemented assumes that the cross section can be

factorized in the following manner

$$\frac{d^3\sigma}{dydp_Tdm} = \frac{d^2\sigma}{dydp_T} \cdot \frac{d\sigma}{dm} \tag{5.2}$$

where y is the rapidity, p_T^W is the transverse momentum, and m the mass of the W boson. In general this is not correct and the issue of the correlation between the two terms in equation 5.2 is addressed later in this section.

The generation begins by selecting the sign of the W which then defines the polarization of the boson. For a W^+ the polarization vector is opposite the proton direction, where the proton direction is taken to be along the +Z axis. A fraction (f_{ss}) of events involve quarks that both originate from the sea. If this is the case then 1/2 of these events have their polarization reversed. From the distribution of $\frac{d^2\sigma(p\bar{p}\rightarrow W^+)}{dydp_T^W}$ the rapidity and transverse momentum for the W boson are selected. There are two $\frac{d^2\sigma}{dydp_T^W}$ distributions used which depend upon whether or not a sea quark was involved in the interaction. The calculation of $\frac{d^2\sigma}{dydp_T^W}$ was provided by the authors in reference [23]. The mass of the boson is then selected from a relativistic Breit-Wigner modified by a function that depends upon the parton luminosity. The parton luminosity term occurs because the momentum distribution of the quarks makes it more probable that a particle with a mass of 60 GeV/c^2 will be produced than a mass of 90 GeV/c^2. The mass distribution is given by

$$\frac{d\sigma}{dm} = PL(m) \cdot \frac{m^2}{(m^2 - M^2)^2 + \frac{m^4\Gamma^2}{M^2}} \tag{5.3}$$

where $PL(m)$ is the parton luminosity term, m is the mass of the particle being generated, M is the true mass of the particle, and , is the natural width of the particle. The parton luminosity distribution is well modeled by the function, $PL(m) = \frac{e^{-\beta \cdot m}}{m}$, where the slope ($\beta$) is evaluated in the following way. The cross section may be written as

$$\frac{d^2\sigma}{dx_1 dx_2} = f_{q/p}(x_1) f_{\overline{q}'/\overline{p}}(x_2) \widehat{\sigma}(m^2) \tag{5.4}$$

where $f_{q/p}(f_{\overline{q}'/\overline{p}})$ is the probability a (anti)quark from the (anti)proton carries a given momentum fraction $x_1(x_2)$. Using $m^2 = x_1 x_2 s$, where $\sqrt{s}$ is the center of mass energy, to change variables in terms of the mass, equation 5.4 becomes

$$\frac{d\sigma}{dm} = \frac{e^{-\beta \cdot m}}{m} \widehat{\sigma}(m^2) \tag{5.5}$$

where

$$e^{-\beta \cdot m} = \frac{2m^2}{s} \int_{\frac{m^2}{s}}^{1} \frac{dx_1}{x_1} f_{q/p}(x_1) f_{\overline{q}'/\overline{p}}\left(\frac{m^2}{s x_1}\right). \tag{5.6}$$

The β used depends upon the rapidity distribution of the $W(Z)$ boson and therefore on the cuts applied to the leptons. The allowed rapidity range of the boson changes the choice of β because of the correlation between the mass and the rapidity. Figure 5.1 shows the parton luminosity slope for the W^+ as a function of the W boson rapidity for the MRSD-' parton distribution function (pdf). To measure β the invariant mass distribution from the CMS Monte Carlo is compared to that from the RESBOS Monte Carlo [46]. The RESBOS Monte Carlo does the full triple differential cross section $\left(\frac{d^3\sigma}{dy dp_T dm}\right)$. Before the selection cuts and with a β averaged over the

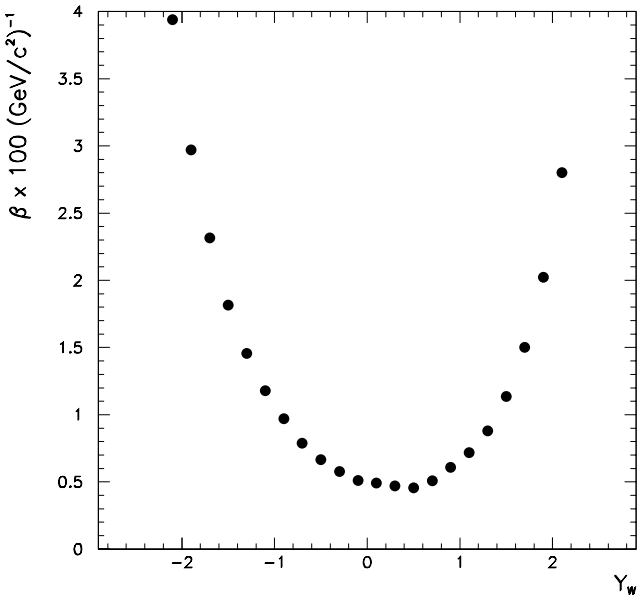

Figure 5.1: Parton luminosity slope as a function of the rapidity of the W^+ for the MRSD-' parton distribution function.

entire rapidity distribution, the mass spectra of the two Monte Carlos are identical. After applying the selection cuts to the leptons the differences in the invariant mass distributions are due to the change in the parton luminosity factor. Table 5.1 shows the parton luminosity slope for the most recent parton distribution functions.

The vertex of the event is generated according to a Gaussian distribution with a mean (=0 cm) and RMS (=25 cm) which are the same as that observed in the data. At this point kinematics of the W boson event are entirely defined.

In the rest frame the W boson is decayed into the leptons. The angular distribution of the leptons depends upon the type of quarks that produced the W boson.

PDF	$\beta_W \times 100$ $(GeV/c^2)^{-1}$	$\beta_Z \times 100$ $(GeV/c^2)^{-1}$	f_{ss}
MRSA	0.667	0.359	0.207
MRSD-'	0.646	0.373	0.201
CTEQ3M	0.624	0.326	0.203

Table 5.1: The parton luminosity slope for different parton distribution functions. β_W is the slope for CC W boson events and β_Z is the slope for CC-CC Z boson events. The last column is the fraction of sea-sea interactions for the given parton distribution function.

For the W^+ the cross section [45] may be written as

$$\begin{aligned} \frac{d^2\sigma}{dy\, d\cos\theta^*} &\sim (1-\cos\theta^*)^2\left(\frac{1}{2}\frac{d\sigma_s}{dy}+\frac{d\sigma_v}{dy}\right)+(1+\cos\theta^*)^2\frac{1}{2}\frac{d\sigma_s}{dy} \\ &\sim (1-\cos\theta^*)^2\frac{d\sigma_v}{dy}+(1+\cos^2\theta^*)\frac{d\sigma_s}{dy} \end{aligned} \tag{5.7}$$

where the subscript $v(s)$ refers to the contribution from valance(sea) quarks and θ^* is the angle of the electron with respect to the +Z direction. The leptons are generated with the angular distribution given in equation 5.7 with the ϕ being generated randomly from 0 to 2π. Deviations from the angular distribution given in equation 5.7 due to higher order loop effects are expected to be small for the p_T^W region used in this analysis [47]. The leptons are then boosted into the lab frame using the four vector of the generated boson.

The angular distribution of the leptons in Z boson decays have the form [45]

$$\begin{aligned} \frac{d\sigma}{d\cos\theta^*} &\sim \left[(g_V^q)^2+(g_A^q)^2\right]\left[(g_V^e)^2+(g_A^e)^2\right](1+\cos\theta^*)^2+ \\ &\quad 8 g_V^q g_A^q g_V^e g_A^e \cos\theta^* \end{aligned} \tag{5.8}$$

where g_x^y, $x = \{V, A\}$ and $y = \{q, e\}$, are the vector and axial couplings for the quarks and leptons. Because DØ does not have a central magnetic field the sign of the leptons is not measured. This effectively averages $\cos\theta^*$ to zero giving the angular distribution of the leptons the form $(1 + \cos\theta^*)^2$.

5.2.2 $p\overline{p} \rightarrow W \rightarrow e\nu\gamma$ and $W \rightarrow \tau\nu \rightarrow e\nu\nu\nu$

The radiative process $W \rightarrow e\nu\gamma$ is generated using the calculation from Berends and Kleiss [48]. This calculation is done at $\mathcal{O}(\alpha_{em})$ and does not include the radiation from the initial state quarks. The calculation has a lower limit on the energy of the photon that may produced (γ_{Min}). The value of γ_{Min} defines the fraction of events that radiate. The nominal value of γ_{Min} is 50 MeV which defines ~31% of the events as radiative events. For events that have a photon in the final state the p_T^W, y, and mass are determined in the same manner as in section 5.2.1. The electron, photon, and neutrino are then boosted into the lab frame. The separation of the electron and photon in the lab frame is defined by

$$R_{e,\gamma} = \sqrt{(\phi_e - \phi_\gamma)^2 + (\eta_e - \eta_\gamma)^2} \tag{5.9}$$

where ϕ and η are the phi and rapidity of the electron and photon. Figure 5.2 shows the $R_{e,\gamma}$ and transverse momentum of the photon for CC W boson events. Due to detector effects if the photon is near the electron it will not be observed as a separate object. If $R_{e,\gamma}$ is less than a parameter ($R_{Coalesce}$) then the photon energy is merged with the electron. The value of $R_{Coalesce}$=0.3 is taken from a Monte Carlo study of

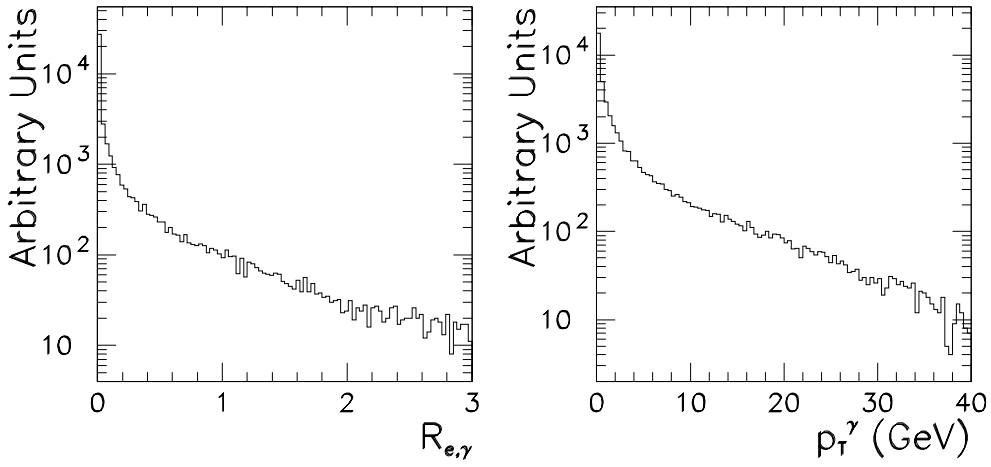

Figure 5.2: The distribution of the separation between the electron and photon, and the p_T of the photon for CC W boson radiative events.

radiative events where the electron and photon were put through the DØGEANT simulation and the event reconstruction program [56].

The radiative program also does the $Z \rightarrow ee\gamma$ decay [48] where *one* of the electrons is allowed to radiate. For the nominal value of γ_{Min} ~66% of the events are radiative.

The $W \rightarrow \tau\nu \rightarrow e\nu\nu\nu$ decay is topologically indistinguishable from the $W \rightarrow e\nu$ decay. The $\tau \rightarrow e\nu\nu$ decay is included in the Monte Carlo with a branching fraction for $\tau \rightarrow e$ of 0.18. The process $W \rightarrow \tau\nu$ is generated in the same manner as $W \rightarrow e\nu$. In the rest frame of the τ the three body decay, $\tau \rightarrow e\nu\nu$, is done. The energy and angular correlations of the electron with respect to the τ polarization vector are preserved by selecting from a two dimensional distribution obtained from $\tau \rightarrow e\nu\nu$ decays generated with the ISAJET [49] program. After the selection cuts

are applied 2.3% of the $W \rightarrow \tau \rightarrow e$ events are accepted.

5.3 Detector Resolutions

In order to properly model the W and Z boson events the effect of the detector must be applied to the observed quantities. The detector effects are: the electromagnetic energy and angular resolutions, the hadronic momentum resolution, the efficiencies, the acceptances, and small corrections to the electron and recoil momentum vectors. The resolutions and efficiencies used in the Monte Carlo are mostly measured from the collider data.

5.3.1 Angular Resolution of the Electrons

The polar angle (θ) of the electron is determined from COGs of the electron cluster and track. These points have a resolution associated with them which translates into a resolution on the polar angle. The electron cluster position resolution is taken from a DØGEANT simulation of single electrons. In the central calorimeter this resolution was found to be both a function of the angle of incidence and the position in the calorimeter. The resolution is parameterized with the following function

$$\sigma(\theta^{'}, Z) = (a + b \cdot \theta^{'}) + (c + d \cdot \theta^{'}) \cdot \mid Z \mid \qquad (5.10)$$

where Z is the position in the calorimeter in centimeters, and $\theta^{'}$ is the angle with respect to the normal in degrees. The values of the parameters are shown in table 5.2.

Parameter	Value
a	0.33183 cm
b	$0.52281 \cdot 10^{-2}$ cm/degree
c	$0.41968 \cdot 10^{-3}$
d	$0.75496 \cdot 10^{-4}$/degree

Table 5.2: Parameters used in the resolution function for the Z position in the central calorimeter.

In the CC the Z position resolution varies from 0.4 to 1.1 cm depending on the angle and position. In the forward calorimeters the electron radial position resolution is found to be 0.2 cm. The azimuthal angle resolution of the cluster is determined from several methods: test beam, Monte Carlo, and data studies and in the central and forward calorimeters is $\sim 3 \cdot 10^{-3}$ rad.

The second point used to determine the polar angle comes from the (Z_{Trk}, R_{Trk}) position of the COG of the associated track. The resolution of the track COG is determined from CC-CC Z boson events. The polar angle for each electron defines a Z position along the beamline (Z_1 and Z_2). The difference between the Z positions ($\Delta Z_v = Z_1 - Z_2$) for each Z boson event is then plotted. The Monte Carlo is then compared to the ΔZ_v distribution as a function of the Z_{CDC} position resolution. It has been found that a double Gaussian for the Z_{CDC} resolution best reproduces the observed ΔZ_v distribution. Figure 5.3 shows the ΔZ_v distribution from the data and the Monte Carlo simulation. Table 5.3 lists the resolutions of the two Gaussians and the fraction of time that each Gaussian is used.

Gaussian	Z_{CDC} Resolution	Fraction
1	0.306 cm	94%
2	1.556 cm	6%

Table 5.3: The resolution parameters used to smear the Z_{CDC} position. The fraction represents the percentage of time that each resolution is used.

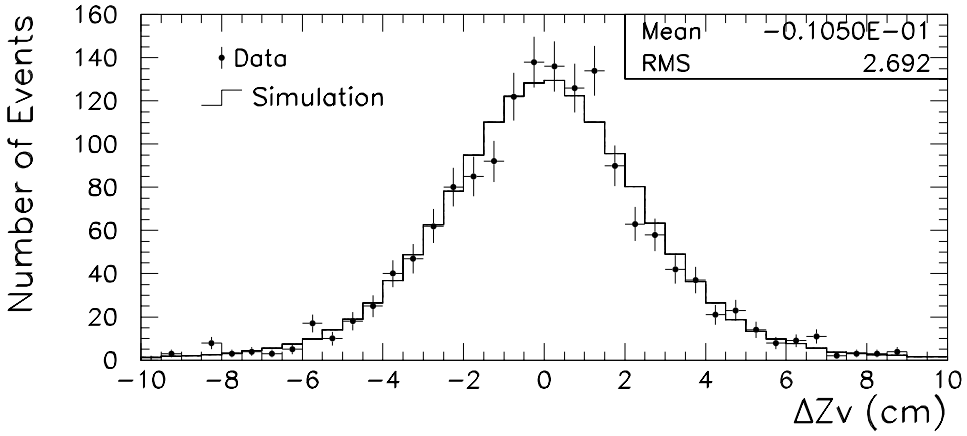

Figure 5.3: The ΔZ_v distribution from CC-CC Z boson events. The dots are the data and the solid line the Monte Carlo simulation.

Parameter	Central Calorimeter	Forward Calorimeter
$\mathcal{C}$	$0.9^{+0.30}_{-0.45}\%$	1.00%
$\mathcal{S}$	$13.5\% \sqrt{GeV}$	$15.7\% \sqrt{GeV}$

Table 5.4: Electromagnetic energy resolution parameters for the central and forward calorimeters.

5.3.2 Electromagnetic Energy Resolutions

The electromagnetic energy resolution may be written as follows [50]

$$\frac{\Delta E}{E} = \mathcal{C} \oplus \frac{\mathcal{S}}{\sqrt{E_T}} \oplus \frac{\mathcal{N}}{E} \tag{5.11}$$

where $\mathcal{C}$ is the constant term, $\mathcal{S}$ is the sampling term, and $\mathcal{N}$ is the noise term. The square root of E_T is used for events in the central calorimeter but in the forward calorimeter $\sqrt{E}$ is used [51]. Table 5.4 lists the values of the resolution parameters in the CC and EC. The resolution due to the noise term is taken directly from the W boson events and is incorporated into a correction to the electron energy, see section 5.3.4. The sampling term is measured by using the testbeam data [58] and is taken to be exact. Any uncertainty in the energy resolution is incorporated into an error on the constant term.

The constant term is determined from the width of the invariant mass distribution from CC-CC Z boson events. At this point all the resolutions that affect the invariant mass distribution have been measured except for the constant term. By varying the constant term in the Monte Carlo the best fit to the invariant mass distribution is obtained. Figure 5.4 shows the χ^2 fit to the invariant mass distribution as a function

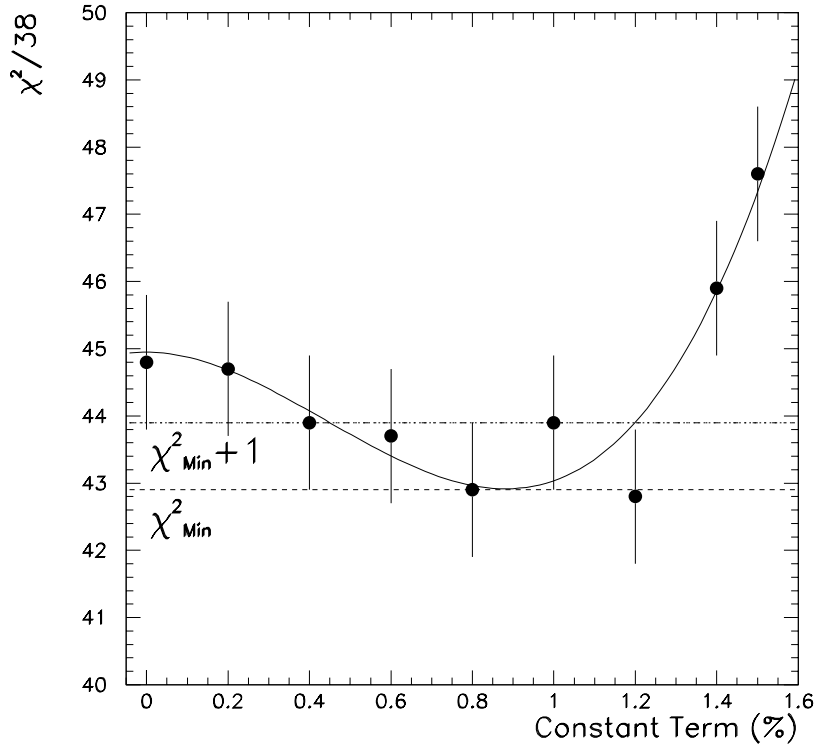

Figure 5.4: The χ^2 between data and Monte Carlo as a function of the electromagnetic resolution constant term for CC-CC Z boson events.

of the constant term. The minimum of the chi squared (χ^2_{Min}) yields a constant term of 0.9%. The error on the constant term is determined from the range allowed by $\chi^2_{Min}+1$ and is $^{+0.30}_{-0.45}$%.

5.3.3 Hadronic Response and Resolutions

A W or Z boson event can be thought of as a hard scattering which produces the boson plus the hadronization of the spectator partons. The hard scattering produces a W boson with some initial transverse momentum which is balanced by energy flow in the opposite direction, and the spectator partons which produce an energy flow which is symmetric in ϕ. The recoil vector that is measured by the detector is the sum of these two processes. The model used to simulate the recoil vector is twofold. The resolution of the recoil that balances the initial p_T of the boson is assumed to be modeled by the function

$$\frac{\Delta p_T}{p_T} = \mathcal{C}_H \oplus \frac{\mathcal{S}_H}{\sqrt{p_T}}. \tag{5.12}$$

where from the QCD group the value of $\mathcal{C}_H$ is taken to be 4%. The sampling term ($\mathcal{S}_H$) is measured from the Z boson data and is presented below.

The contribution from the spectator partons is modeled using minimum bias data. A minimum bias event is an event where an inelastic collision takes place between the proton and antiproton. The $\not\!\!E_T$ from the minimum bias event is added, randomly in ϕ, to the Monte Carlo. The minimum bias events were collected throughout the run. The luminosity at which the W boson events were recorded varies from $1{\cdot}10^{30}$ to $20{\cdot}10^{30}$ cm^{-2}sec^{-1} and is shown in figure 5.5. From references [51, 52] the following relationship between the instantaneous luminosity of the $W(\mathcal{L}_W)$ and minimum bias ($\mathcal{L}_{Min}$) events is given by

$$1 + \sigma \mathcal{L}_W t = \frac{\sigma \mathcal{L}_{Min} t}{1 - e^{-\sigma \mathcal{L}_{Min} t}} \tag{5.13}$$

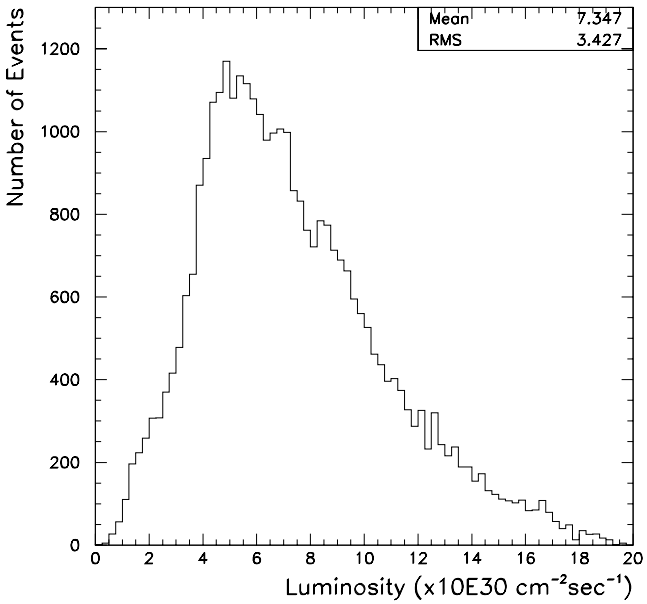

Figure 5.5: The instantaneous luminosity distribution for the W boson events.

where σ=46 mb is the total inelastic cross section integrated over the DØ acceptance, and t=3.5 μsec is the beam crossing time. From equation 5.13 and the luminosity distribution of the W boson events the appropriate luminosity from which to pick the minimum bias event is determined. It is important to match the luminosity distribution of the W boson events since as the instantaneous luminosity increases the average number of interactions increases and other effects like pileup and detector noise are then modeled properly. The magnitude of the $\not\!\!E_T$ from the minimum bias event is scaled by a factor (MB) which allows for the tuning of the resolution. How $\mathcal{S}_H$ and MB are measured will be discussed later in this section.

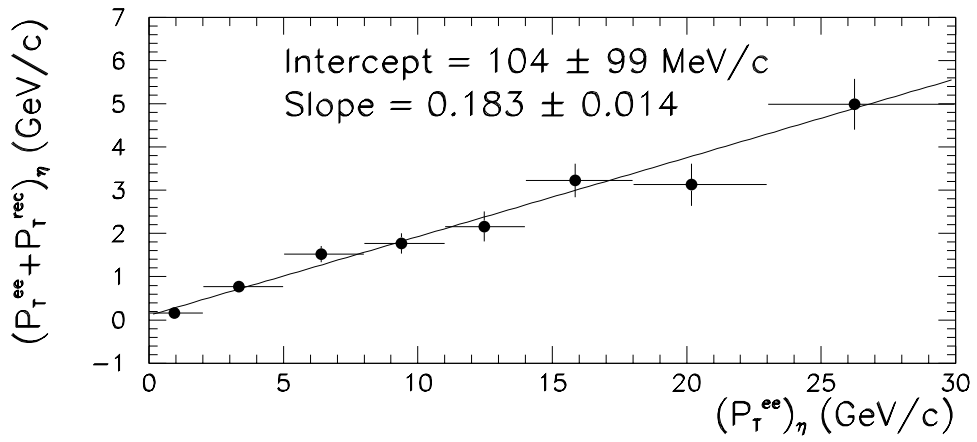

Figure 5.6: The fit to $(\vec{p}_T^{ee} + \vec{p}_T^R) \cdot \hat{\eta}$ versus $\vec{p}_T^{ee} \cdot \hat{\eta}$ for CC-CC and CC-EC Z boson events. The fit has a $\chi^2/\text{dof} = 7.4/6$.

Hadronic Response

The hadronic response (α_H) is the energy scale of the hadronic recoil of the boson. The hadronic response is measured relative to the electromagnetic energy scale. The hadronic response is lower than the electromagnetic response for several reasons. The recoil is mainly composed of pions which inherently have a lower response than electrons and the recoil particles may go into regions of the calorimeter that have poor response. The hadronic response is defined to be

$$\vec{p}_T^R = \alpha_H \vec{p}_T^{ee}. \tag{5.14}$$

From Z boson events the plot of $(\vec{p}_T^{ee} + \vec{p}_T^R) \cdot \hat{\eta}$ versus $\vec{p}_T^{ee} \cdot \hat{\eta}$ measures α_H, see figure 5.6.

The events used in figure 5.6 are CC-CC and CC-EC events. CC-EC events are

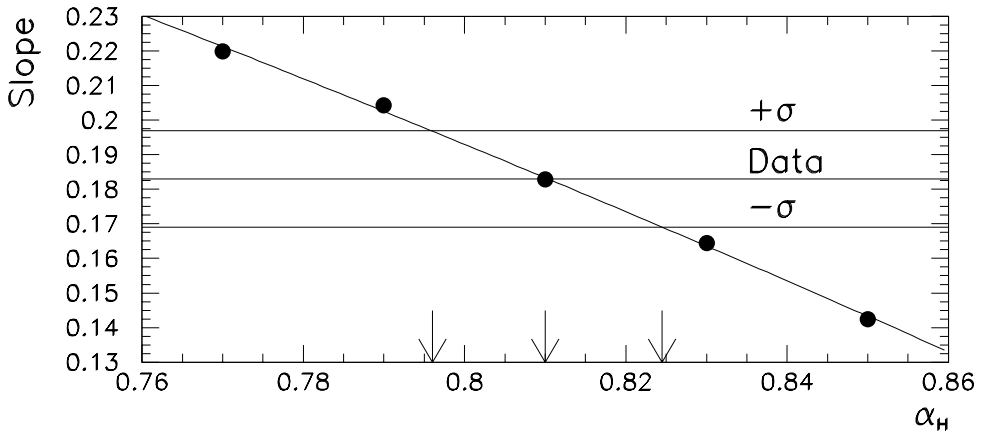

Figure 5.7: Slope of the fit to the $(\vec{p}_T^{ee} + \vec{p}_T^R) \cdot \hat{\eta}$ versus α_H. The fit to the data and errors are plotted yielding $\alpha_H = 0.810 \pm 0.015$.

used in order to give the Z boson the same topology as the CC W boson events since the neutrino is not observed so its rapidity is not restricted to the central region. The Monte Carlo is then used to derive fit slope values as a function of α_H, see figure 5.7. This is done because in the Monte Carlo there are corrections applied to the recoil which affect the hadronic response, see section 5.3.4. Figure 5.7 shows the value of the hadronic response for a given slope value. Using the slope from figure 5.6 the hadronic response is found to be 0.810 ± 0.015. The hadronic response obtained from figure 5.7 is lower by 0.007 than if the slope in figure 5.6 had been used. This change is less than half the statistical error on α_H. The error on α_H is assigned a 0.005 systematic error due to the uncertainties in the EC electromagnetic energy scale. Thus, the hadronic response is $\alpha_H = 0.810 \pm 0.016$.

Several consistency checks have been performed on the stability of the value of the hadronic response. If one restricts the electrons from the Z boson to the central

calorimeter only then $\alpha_H = 0.804 \pm 0.019(stat.)$. This value is consistent with the CC-CC/CC-EC events. For the fit in figure 5.6 the intercept is allowed to float. One could argue that if the $\vec{p}_T^{ee} = 0$ then you should not have an offset and indeed the offset that is returned is consistent with zero. This is checked by forcing the fit in figure 5.6 through zero. This gives a hadronic response of $0.800 \pm 0.010(stat.)$, with a $\chi^2/\text{dof} = 7.6/7$, which is again consistent with the previous result.

Hadronic Resolution

To measure the hadronic resolution parameters the Monte Carlo is used to determine the resolution on the η-balance as a function of MB and $\mathcal{S}_H$. The η-balance is computed with the hadronic recoil vector that is corrected for the hadronic response, i.e. the η-balance is equal to $(\vec{p}_T^{ee} + \vec{p}_T^{R}/\alpha_H) \cdot \hat{\eta}$. The following equation is evaluated

$$\chi^2(MB, \mathcal{S}_H) = \sum_{i=1}^{6} \left(\frac{\sigma_\eta^i(Elc) \oplus \sigma_\eta^i(MB) \oplus \sigma_\eta^i(\mathcal{S}_H) - \sigma_\eta^i}{\delta_{\sigma_\eta}^i} \right)^2 \tag{5.15}$$

where for the bin i

- σ_η^i is the η-balance resolution from the data
- $\delta_{\sigma_\eta}^i$ is the error on the η-balance resolution from the data
- $\sigma_\eta^i(Elc)$ is the η-balance resolution due to the electrons
- $\sigma_\eta^i(MB)$ is the η-balance resolution due to the number of minimum bias events
- $\sigma_\eta^i(\mathcal{S}_H)$ is the η-balance resolution due the hadronic sampling term.

$\mathcal{C}_{\mathbf{H}}$	$\mathcal{S}_{\mathbf{H}}$	MB
4%	49±14%	1.01±0.03

Table 5.5: The hadronic resolution parameters.

$\vec{p_T}(ee)\cdot\hat{\eta}$	η-**Balance Resolution**(GeV/c)					
bin (GeV/c)	**Electron**	$\mathcal{S}_H$	MB	**Quadrature**	**Data**	χ
0-1	0.163	0.225	4.220	4.229	4.42±0.21	0.91
1-2	0.177	0.509	4.275	4.309	4.40±0.24	0.38
2-4	0.183	0.767	4.299	4.371	4.41±0.21	0.19
4-7	0.207	1.115	4.225	4.375	4.14±0.20	-1.18
7-12	0.258	1.526	4.235	4.509	4.77±0.23	1.14
12-25	0.389	2.182	4.223	4.769	4.95±0.29	0.62
					$\chi^2/\mathrm{dof} = 4.1/4$	

Table 5.6: The $(\vec{p_T^{ee}} + \vec{p_T^R}/\alpha_H)\cdot\hat{\eta}$ resolution in the different $\vec{p_T^{ee}}\cdot\hat{\eta}$ bins. Shown are the values for the nominal values of resolution parameters for the electron, $\mathcal{S}_H$, MB, the three taken in quadrature, the data values, and the comparison between the data points and the Monte Carlo.

The sum runs over bins $\vec{p_T}(ee)\cdot\hat{\eta}$ of the size 0-1, 1-2, 2-4, 4-7, 7-12, and 12-25 GeV/c which were chosen to give the same error on δ_{σ_η}. The values of MB and $\mathcal{S}_H$ are taken from the minimum of equation 5.15 (χ^2_{Min}). The error on hadronic resolution parameters is taken from the contour traced out from the $\chi^2_{Min}+1$ ellipse. Figure 5.8 shows the 1σ contour in the MB and $\mathcal{S}_H$ plane. Table 5.5 lists the nominal values of the hadronic resolution parameters and their errors. Figure 5.9 shows the contribution from each component of the η-balance resolution as a function of $\vec{p_T}(ee)\cdot\hat{\eta}$ for the nominal values of the resolution parameters. Figure 5.10 shows the comparison between the Monte Carlo and data for the η-balance and ξ-balance distributions.

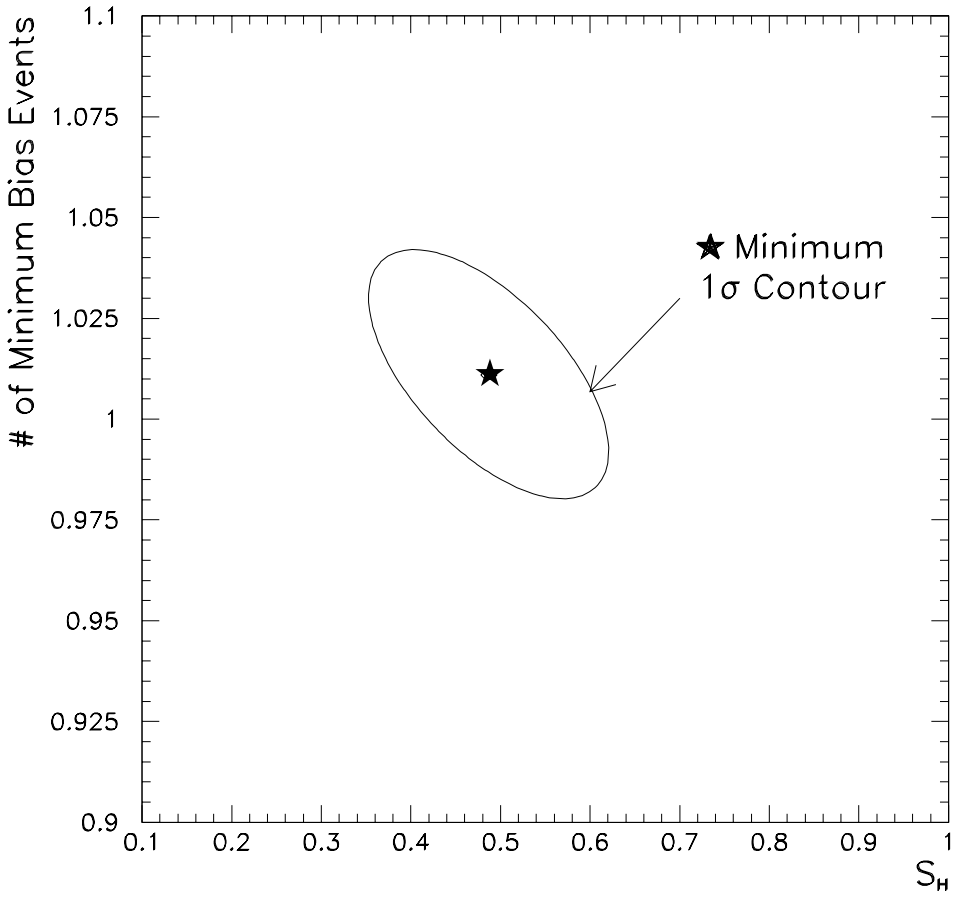

Figure 5.8: The correlation between the hadronic resolution parameters. The nominal values are represented by the star and the solid line is the one standard deviation contour.

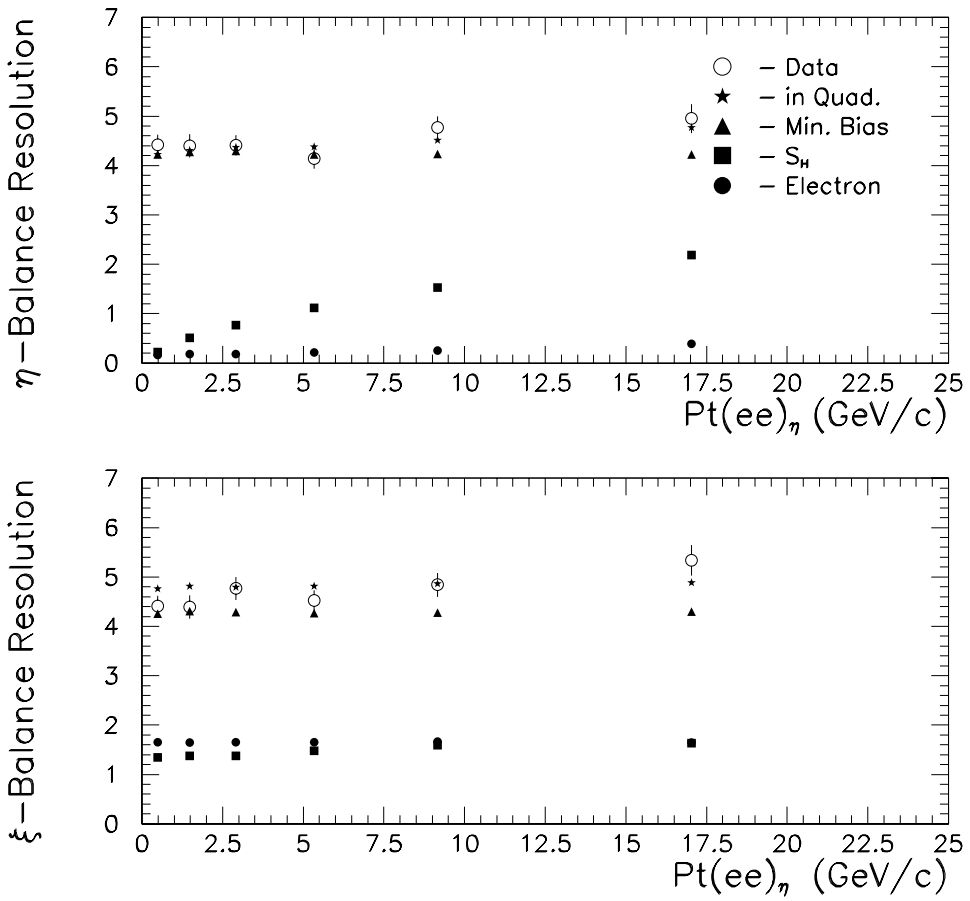

Figure 5.9: The top plot is the η-balance resolution as a function of $\vec{p_T}(ee) \cdot \hat{\eta}$. The three components of the η-balance resolution are shown on the plot: solid circles are the resolution from the electron energy and angle, the solid squares are the resolution from the hadronic sampling term, the solid triangles are the resolution from the number of minimum bias event, the stars are the three resolutions taken in quadrature, and the open circles are the data values. The bottom plot is the ξ-balance as a function of $\vec{p_T}(ee) \cdot \hat{\eta}$ and is only used as a consistency check.

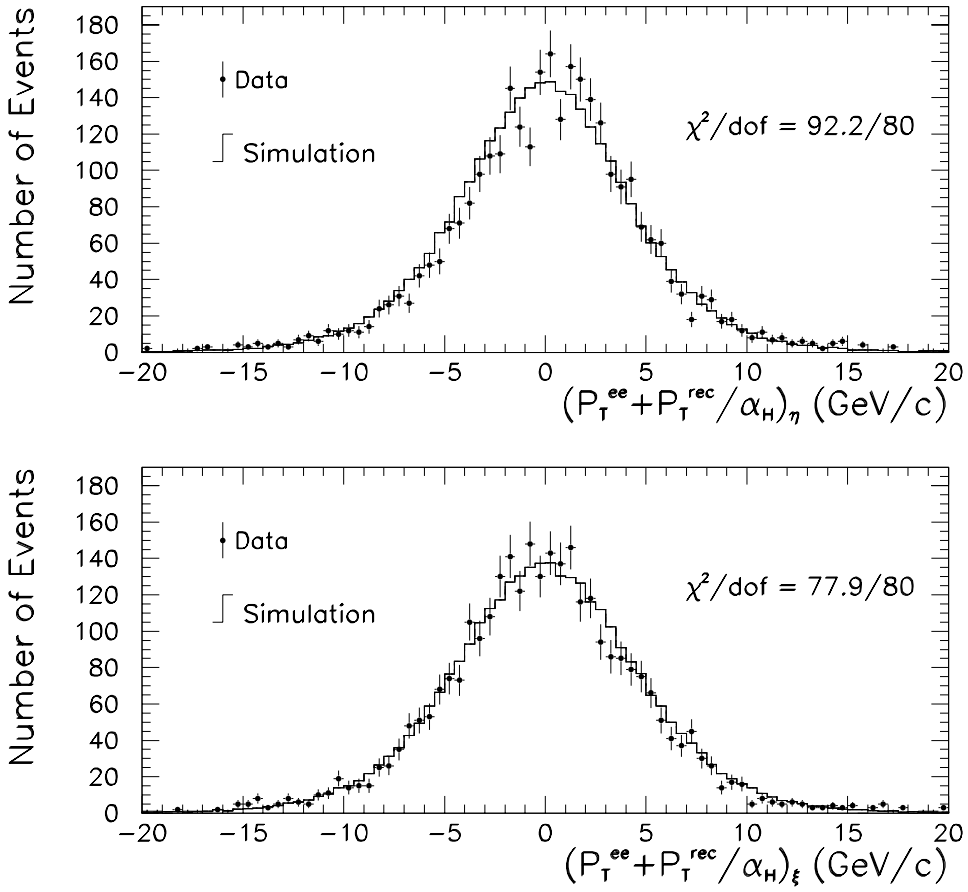

Figure 5.10: Comparison between the Monte Carlo and the data for the η-balance and ξ-balance which have been corrected for the hadronic response.

$\vec{p_T}(ee)\cdot\hat{\xi}$	ξ-Balance Resolution(GeV/c)					
bin (GeV/c)	Electron	$\mathcal{S}_H$	MB	Quadrature	Data	χ
0-1	1.654	1.344	4.256	4.760	4.41±0.21	-1.67
1-2	1.643	1.379	4.312	4.816	4.39±0.24	-1.78
2-4	1.657	1.373	4.285	4.795	4.77±0.23	-0.11
4-7	1.659	1.478	4.267	4.811	4.52±0.21	-1.39
7-12	1.670	1.591	4.280	4.862	4.84±0.24	-0.09
12-25	1.647	1.634	4.300	4.886	5.34±0.31	1.47
					χ^2/dof = 10.1/6	

Table 5.7: The $(\vec{p}_T^{ee} + \vec{p}_T^R/\alpha_H)\cdot\hat{\xi}$ resolution for the nominal values of the resolution parameters.

5.3.4 Corrections to the Momentum Vectors

Due to the manner in which the electron and the recoils are measured in the data corrections to the Monte Carlo vectors are required. There are two effects: a correction to the electron vector for energy flowing into the window that is not from the electron and a correction to the recoil vector for energy lost under the electron. These two values are different due to the zero suppression of the calorimeter cells.

The measurement of the recoil vector does not include the electron(s) window cells. The correction to the recoil vector is called $\Delta U_{||}$ because the correction is along the electron axis which defines $U_{||}$. This quantity is determined from the W boson events by rotating, in ϕ, a 5×5 window away from the electron and summing the energy within that region. An isolation cut is applied to the rotated window position since the rotated window may overlap with a region of high activity [53]. If this were the case then the electron identification cuts would remove this event. The electron energy from the core of the electron (EM($\mathcal{R}$=0.2)) is used to calculate the

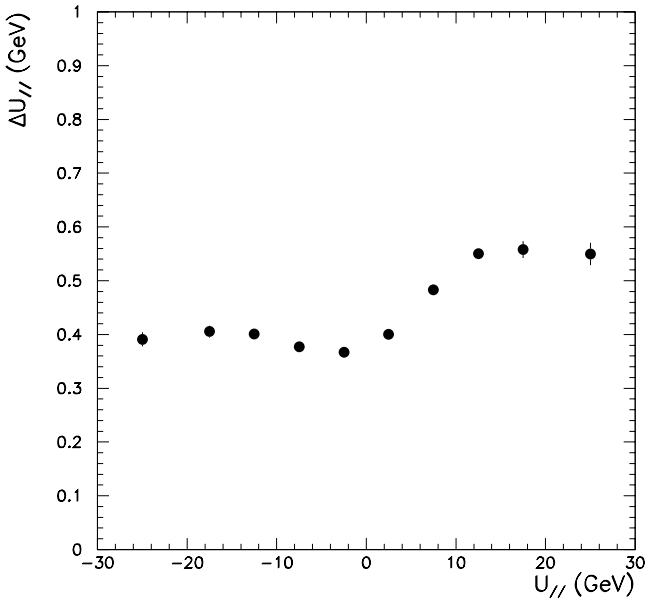

Figure 5.11: The $\Delta U_{||}$ correction versus $U_{||}$ after the luminosity dependence has been removed.

isolation variable (f_{iso}^{Rot}) for the rotated position. The isolation is required to pass the f_{iso}^{Rot} <0.15 cut. The $\Delta U_{||}$ correction is found to be luminosity dependent and is given by

$$\frac{d\Delta U_{||}}{d\mathcal{L}} = 11.2 \cdot \frac{MeV}{10^{30}\mathrm{cm}^{-2}\mathrm{sec}^{-1}}. \tag{5.16}$$

Observe that $\Delta U_{||}$ changes by over 200 MeV for the instantaneous luminosity range given in Run 1b. The $\Delta U_{||}$ correction is also found to be dependent upon the $U_{||}$ of the event. This is because when the recoil energy is near the electron more energy will flow into the window. Figure 5.11 shows the $\Delta U_{||}$ correction versus the $U_{||}$ after the luminosity dependence has been removed. The mean value of $\Delta U_{||}$ for the entire event sample is 460 MeV with an error of 25 MeV. The error was determined by

varying the isolation cut by ± 0.05 about the nominal value.

The energy flow into the electron window that is not due to the electron is called the *underlying event* energy (E_{ue}). This energy is from the spectator partons and the recoil of the boson. To measure this quantity ISAJET electrons which have the same η and E_T distribution as electrons from W boson events are used. These electrons are put through DØGEANT. The electrons are then superimposed onto non-zero suppressed minimum bias data. This gives us three sets of data: the single electrons, the non-zero suppressed minimum bias events, and the overlapped events. The three sets of data are put through the same reconstruction program that was used for the collider data. Then on an event by event basis the energy flow under the electron is computed by taking the difference between the three sets of data. It is found that the underlying event, in the CC, is flat in $\sin\theta$. The luminosity dependence that is used is the same as given in equation 5.16. The average value of the underlying event is $(215 \pm 25)\ MeV$.

In the Monte Carlo the corrections E_{ue} and $\Delta U_{||}$ are modelled according to the distributions which were determined during the analysis. Figure 5.12 shows the distribution of $\Delta U_{||}$ used in the Monte Carlo after the luminosity and $U_{||}$ effects have been applied. By using a similar distribution for E_{ue} the noise term for the electromagnetic resolution is properly modeled.

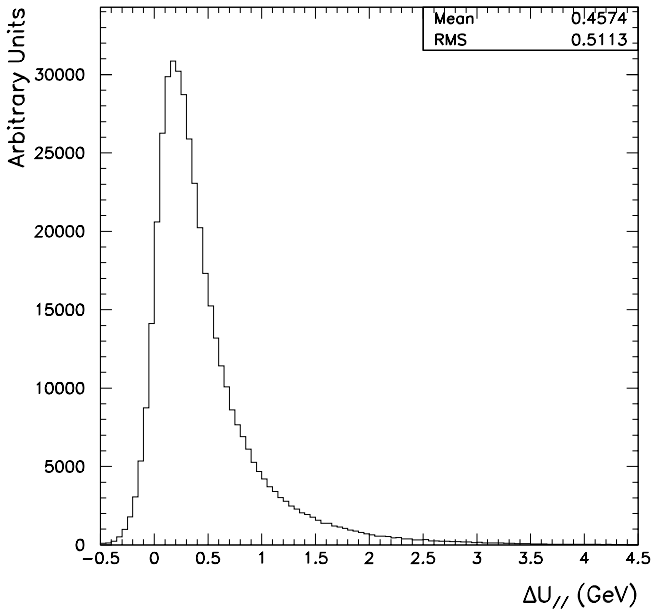

Figure 5.12: The distribution of $\Delta U_{||}$ used in the Monte Carlo.

5.4 Efficiencies

There are four efficiencies that are used in the Monte Carlo. They are the trigger turn on curves for the electron and missing E_T, the electron identification efficiency for the radiative events, and the electron identification efficiency which depends upon the proximity of the recoil vector to the electron.

5.4.1 Trigger Turn on Curves

The trigger turn on curves are a result of the poorer resolution of the kinematic quantities at the trigger level. The electron trigger turn on curve is measured by taking the ratio of the signal trigger to a monitor trigger as a function of the offline

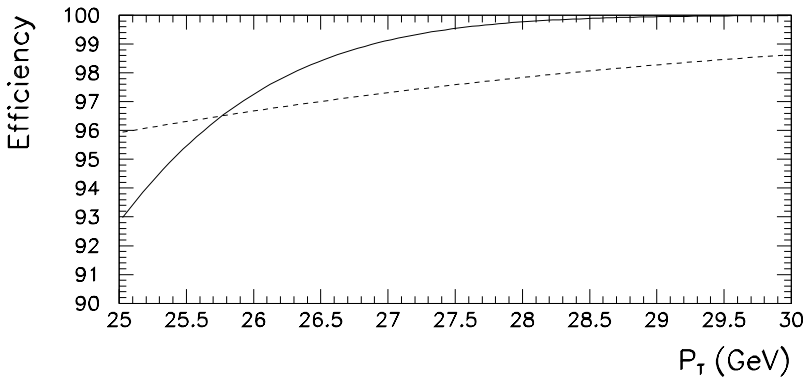

Figure 5.13: The electron and missing p_T trigger turn on curves. The solid line is the electron turn on curve and the dashed line is the missing p_T turn on curve.

electron E_T [54]. The monitor trigger has a lower Level 2 E_T threshold and is 100% efficient in the E_T range of interest for the signal trigger EM1_EISTRKCC_MS. The monitor trigger used is ELE_1_MON which has a Level 2 E_T cut of 16 GeV on the electron. The electrons from the ELE_1_MON trigger are required to pass the same quality cuts as the EM1_EISTRKCC_MS trigger. The signal trigger is found to be 93% efficient for an electron with E_T of 25 GeV and 100% efficient at 30 GeV [54].

The $\not\!\!E_T$ turn on curve is done in a similar manner. The monitor trigger used was EM1_ELE_MON which had the same electron Level 1 and 2 trigger requirements as EM1_EISTRKCC_MS trigger except it did not have a $\not\!\!E_T$ cut. The ratio of these two triggers as a function of the offline $\not\!\!E_T$ determines the turn on curve. The EM1_EISTRKCC_MS trigger is 96% efficient at a $\not\!\!E_T$ of 25 GeV which rises to 99% at a $\not\!\!E_T$ of 30 GeV [55]. Figure 5.13 shows the trigger turn on curves that are implemented in the Monte Carlo.

5.4.2 Electron Identification Efficiencies

There is an electron inefficiency due to the presence of the photon in radiative events. When the photon is near the electron it may cause the isolation or the χ^2 cut to fail the event. This inefficiency has been studied using DØGEANT where the electron and photon were put through the full detector simulation [56]. The efficiency for accepting an event was found to be dependent upon the transverse energy of the photon and the separation between the electron and photon. Most radiative events have either the photon with low p_T or near the electron, i.e. $R_{e,\gamma}$ <0.1. In either of these cases the electron identification is not effected by the presence of the photon. When the photon has $E_T > 1\ GeV$ and is in the region 0.1< $R_{e,\gamma}$ <0.4 then the χ^2 and isolation cuts have the largest effect. The efficiency that is applied in the Monte Carlo is a function of the p_T of the photon and $R_{e,\gamma}$. The number of radiative events lost due to these inefficiencies is 2.5%.

Another electron inefficiency is due to the presence of the recoil particles near the electron. This inefficiency is determined as a function of the $U_{||}$ in the event since this quantity is a measure of the electron and recoil topology. The $U_{||}$ efficiency is determined by taking single electrons which have the same kinematic and angular distribution as electrons from W boson events and superimposing them on a W boson data event. The overlapped events are then put through the trigger simulator and the reconstruction program. The E_T of the overlapped events is then tuned to match the data since $U_{||}$ and E_T are highly correlated. The following function is

used for the $U_{||}$ efficiency

$$f(U_{||}) = \begin{cases} 1 & U_{||} < U_{||}^o \\ 1 - s(U_{||} - U_{||}^o) & U_{||} > U_{||}^o \end{cases} \tag{5.17}$$

where $U_{||}^o = (3.85 \pm 0.55)\ GeV$ and $s = (0.013 \pm 0.001)\ GeV^{-1}$ [57].

5.5 Comparison between the Monte Carlo and the W Boson distributions

All the parameters and efficiencies used in the Monte Carlo have now been determined, except for the electromagnetic energy scale which will be discussed in chapter 6. Some distributions from W boson events and the Monte Carlo simulation are presented. Figure 5.14 shows the comparison between the data and Monte Carlo for the p_T^W distribution. Figure 5.15 shows the $U_{||}$ and $U_{\perp}$ distributions. Figure 5.16 is the average $U_{||}$ versus the p_T^W, m_t, E_T, and $\not\!\!E_T$. Figure 5.17 shows the rapidity distribution of the electron. The distribution, which is area normalized, shows a decrease in the number of events in the central region. Figure 5.18 shows the electron and track COG Z positions in the CDC and CC which are used to calculate η. Both distributions also show a depression at zero. This may be due to a tracking inefficiency at the center of the CDC. The issue of an η dependence in the W boson mass fit is discussed in section 7.4.

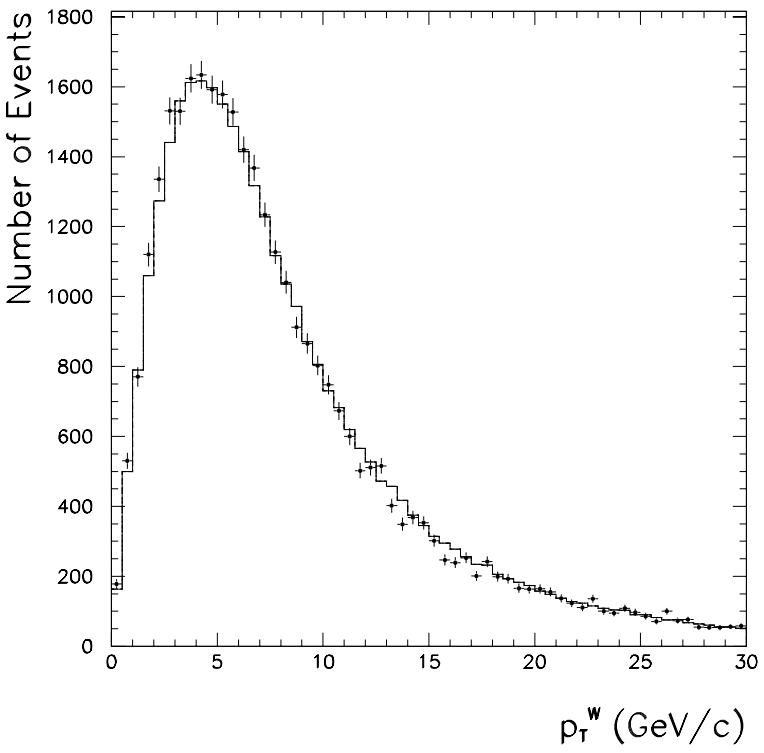

Figure 5.14: The solid points the are data and the histogram is the Monte Carlo for the recoil vector in the W boson events.

Variable	**Data**		**Monte Carlo**	
(GeV)	**Mean**	**RMS**	**Mean**	**RMS**
$U_{\|\|}$	-1.33$\pm$0.04	6.70$\pm$0.03	-1.39	6.62
$U_{\perp}$	-0.04$\pm$0.04	7.32$\pm$0.03	0.01	7.53

Table 5.8: The mean and RMS values for the $U_{||}$ and $U_{\perp}$ distributions. The effect of the backgrounds have been included in the Monte Carlo.

Parameter	Symbol	Value and Error
CC Constant Term	$\mathcal{C}$	$0.9^{+0.30}_{-0.45}\%$
Hadronic Response	α_H	0.810 ± 0.016
Hadronic Sampling Term	$\mathcal{S}_H$	$49 \pm 14\%$
Number of Min. Bias Events	MB	1.01 ± 0.03
Average $\Delta U_{\|\|}$ Correction	$< \Delta U_{\|\|} >$	$460 \pm 25\ MeV$
Average Electron E_T Correction	$< E_{ue} >$	$215 \pm 25\ MeV$
CDC Z Resolution	σ_{z1}	0.306 ± 0.02 cm

Table 5.9: A summary of the inputs to the Monte Carlo.

5.6 Summary

The CMS Monte Carlo has been shown to reproduce the observed kinematic variables in the W and Z boson events. A summary of some of the inputs to the Monte Carlo is shown in table 5.9.

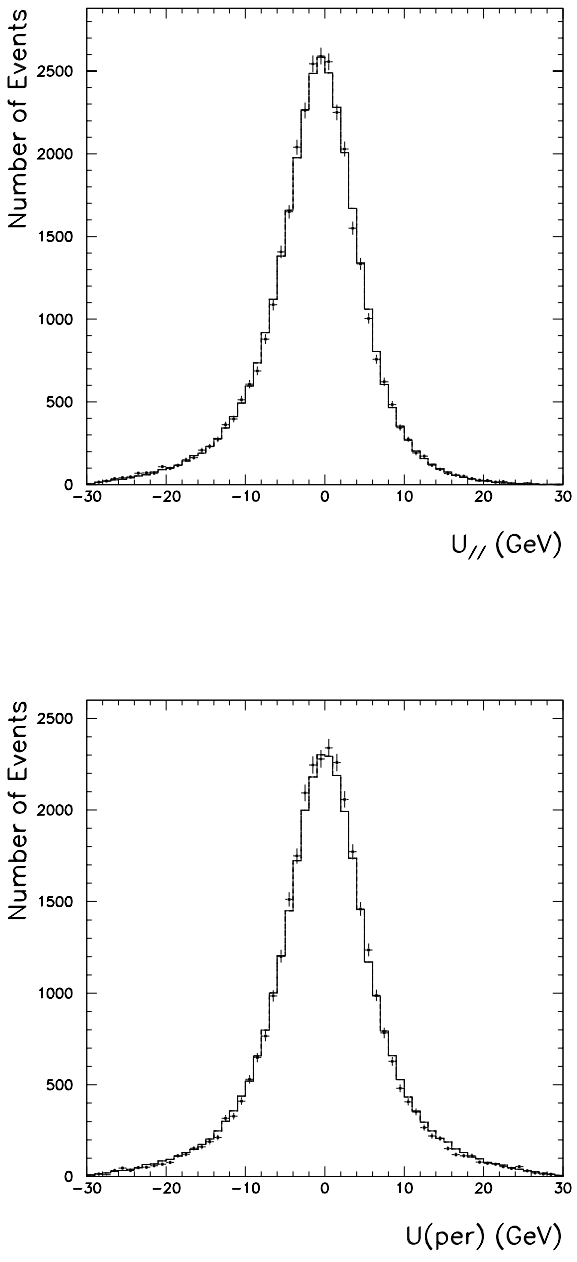

Figure 5.15: The comparison between the Monte Carlo and data for the $U_{||}$ and $U_{\perp}$ distributions. Table 5.8 summarizes the mean and RMS values for the $U_{||}$ and $U_{\perp}$ distributions.

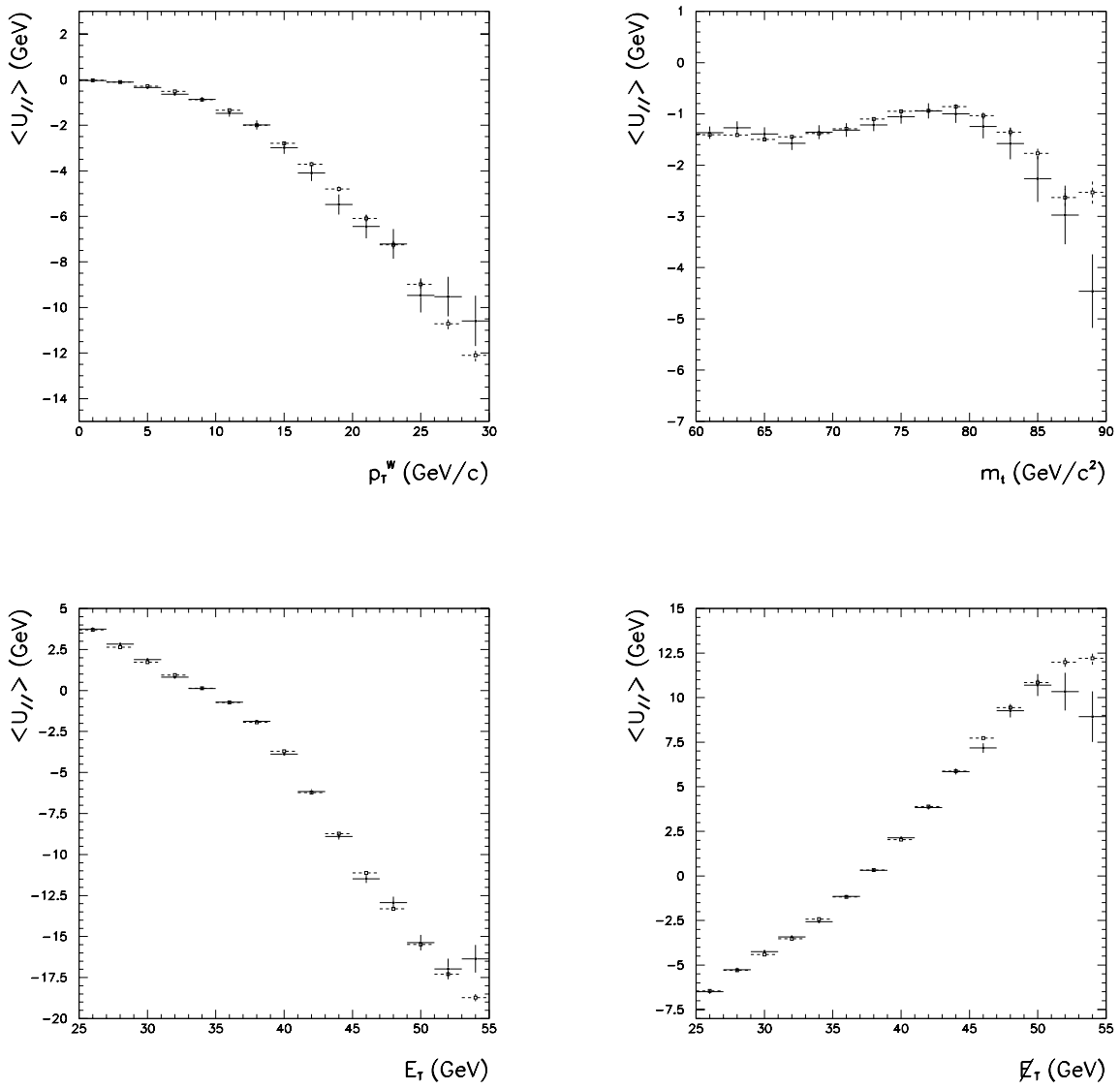

Figure 5.16: The mean $U_{||}$ versus the p_T^W, m_t, E_T, and $\not\!\!E_T$ for the CC W boson events. The solid dots are the data and the open dots are the Monte Carlo simulation.

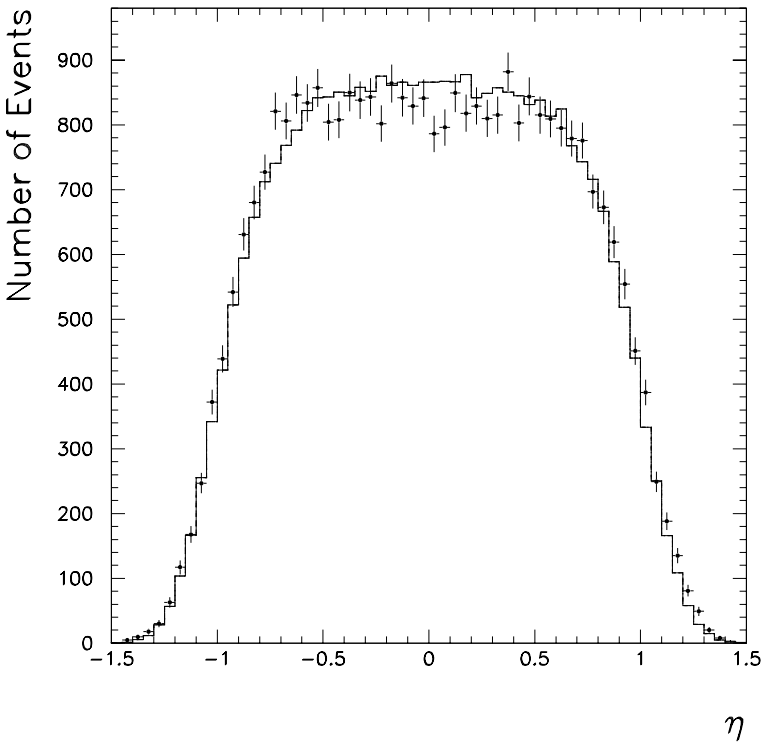

Figure 5.17: The rapidity distribution of the electron in CC W boson events. The histogram is the Monte Carlo and the dots are the data.

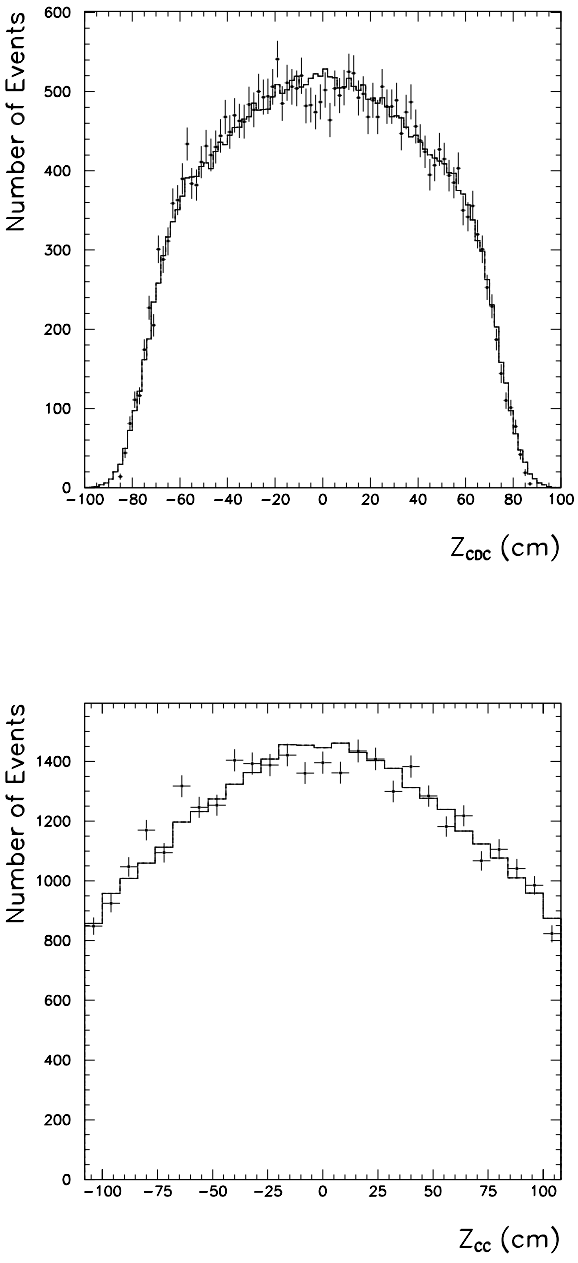

Figure 5.18: The distribution of the Z positions in the CDC (upper plot) and the calorimeter (lower plot).

Chapter 6

The Electromagnetic Energy Scale

6.1 Measuring the Energy of an Electron

The energy of an electron is measured in a window of 0.5×0.5 in $\eta \times \phi$ and includes the first five layers of the calorimeter. Each layer has 25 cells except for EM3 which contains 100 cells. Each cell is built from a number of unit cells which are ganged together. A unit cell consists of a uranium plate, liquid argon gap, and a readout pad, see figure 3.9. The signal received from a cell is digitized and stored as the number of ADC counts. To convert ADC counts to energy *sampling fractions* have been determined from the test beam data [58]. The energy for the i^{th} electron is given by

$$E_i = \alpha \sum_{j=1}^{5} \beta_j \mathcal{A}_{ij} + \delta \tag{6.1}$$

Parameter	Value
β_1	1.308±0.008
β_2	0.852±0.007
β_3	1.0
β_4	0.966±0.004
β_5	1.8395
$\alpha \times 10^3 (GeV/ADC)$	2.956±0.005
$\delta(GeV)$	0.347±0.013

Table 6.1: Sampling fractions determined from the test beam data.

where α is an overall scale, β_j is the weight for layer j, $\mathcal{A}_{ij}$ is the sum of the ADC counts in layer j, and δ is an overall offset. The electron test beam data for the central calorimeter was taken at the three values of $\eta = (0.0, 0.45, 1.05)$ and spanned an energy range from 7.5 to 150 GeV. The sampling fractions are chosen to provide the best linearity, resolution, and uniformity. Since, there is an overall scale α the weight of the third layer (β_3) is defined to be 1. The weight of the FH1 layer (β_5) is given the value expected for a minimum ionizing particle since there is little energy deposited in FH1 and because the optimization technique is insensitive to β_5. The parameters $\alpha, \beta_1, \beta_2, \beta_4$, and δ are obtained by minimizing

$$\chi^2 = \sum_E \sum_{i=1}^{N} \left(\frac{p_i - E_i}{\sigma_E} \right)^2 \tag{6.2}$$

where p_i is the momentum of the electron, E_i is the energy calculated from equation 6.1, and σ_E is the resolution for the energy point E. Table 6.1 lists the sampling fractions obtained from this procedure [58].

It is a very difficult process to measure the absolute energy scale in a test beam

and then transfer that calibration to another detector with the precision *required* for the W boson mass measurement. So are the δ and α are determined from the test beam the correct values for the DØ central calorimeter? The offset δ has been attributed to energy loss due to material in front of the calorimeter [59]. The test beam had different types and amounts of material in front of the calorimeter than the DØ detector. For example, the thickness of the cryostat wall at the test beam was different than what was used in the DØ calorimeter. It follows that the δ evaluated from the test beam data should be different than what is required for the DØ calorimeter.

Another difference between the test beam and the DØ central calorimeter is due to the ϕ modules that were used. The studies conducted at the test beam used only two calorimeter modules. In contrast the DØ central calorimeter was built from 32 modules and the two modules that were in the test beam were not put into the DØ calorimeter. Thus, the scale α which was determined from these two modules may not reflect the response of the DØ calorimeter. For instance, the scale is very sensitive to the spacing of the uranium plates. If the spacing of the two modules in the test beam was somewhat different than what was put in the calorimeter a difference in the response would be expected. A confirmation of this uncertainty comes from the relative calibration of the CC modules done during Run 1a [51]. The relative response of the CC modules was obtained by using an inclusive electron trigger and counting the number of events above an E_T threshold [60]. The distribution of the relative response for the CC modules had an RMS of 1.3%. Therefore, a scale determined

from just two modules should not be expected to give the correct scale for the DØ calorimeter.

6.2 The Scale and the Offset

The task now is to measure the scale and the offset from the collider data. The functional form the energy response is more easily measured, than the absolute energy scale, at the test beam and is given by

$$E^{Meas} = \alpha_{EM} E^{True} + \delta_{EM} \tag{6.3}$$

where E^{Meas} is the measured energy, α_{EM} is the scale, E^{True} is the true energy, and δ_{EM} is the offset measured *relative* to the offset in the sampling fractions. Figure 6.1 shows the fractional deviation of the electron energy response versus momentum using equation 6.3. From equation 6.3 the mass may be written as

$$M^{Meas} = \alpha_{EM} M^{True} + f\delta_{EM} + \mathcal{O}(\delta_{EM}^2) \tag{6.4}$$

where

$$f = \frac{E_1 + E_2}{M}(1 - \cos\gamma) \tag{6.5}$$

and γ is the opening angle between the two decay products. Now that the measured mass is related to the true mass, scale, and offset the electromagnetic decays of the

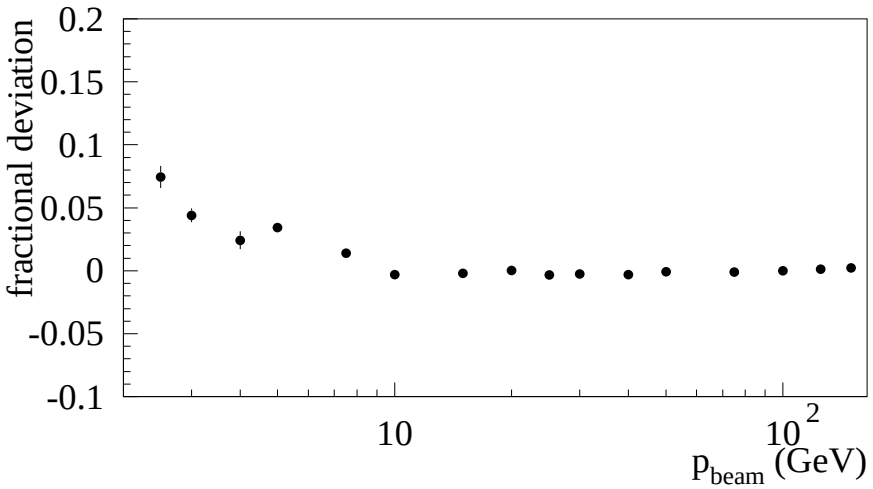

Figure 6.1: Fractional deviation of the electron energy versus the momentum from the test beam. The deviation is from the function given in equation 6.3 where E^{True} is equal to p_{beam}. The response is linear in the region of $p_{beam} > 10 GeV/c$ and only deviates at low momentum.

π^0, J/ψ, and Z boson may be used to constrain α_{EM} and δ_{EM}.

6.2.1 π^0

The electromagnetic decay of the π^0 into two photons allows us to use this resonance to measure the response of the electromagnetic calorimeter. If the π^0 has a $p_T > 1$ GeV/c then the photons from the decay cannot be separated in the DØ calorimeter and the invariant mass cannot be reconstructed. There is a $\sim$ 10% chance that a photon will convert into a e^+e^- pair. If both photons convert then the tracking system can be used to determine the opening angle. The signal sample $\pi^0 \rightarrow e^+e^-e^+e^-$ is selected by looking for two doubly ionizing tracks in the tracking chamber. The energy of the π^0 is defined as the energy of the cluster ($E(\pi^0)$) which has two doubly

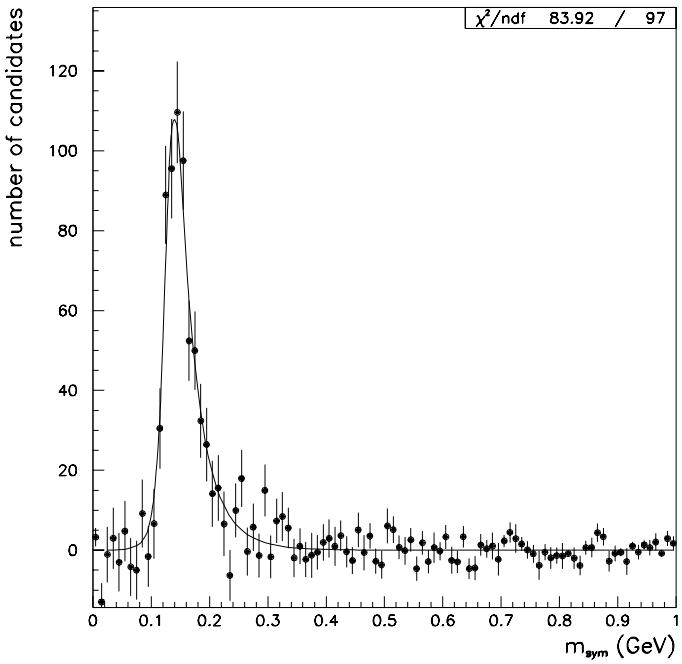

Figure 6.2: The background subtracted symmetric mass distribution from the π^0 decays. The dots are the data and the solid line the Monte Carlo simulation.

ionizing tracks pointing at it. The symmetric mass (m_{sym}) is defined as

$$m_{sym} = \sqrt{\frac{1}{2}E(\pi^0)(1-\cos\gamma)} \tag{6.6}$$

where γ is the opening angle between the converted photons. The magnitude of the symmetric mass is greater than or equal to the invariant mass. A Monte Carlo was written to determine the mass of the π^0 from the symmetric mass distribution as a function of α_{EM} and δ_{EM}. Figure 6.2 shows the background subtracted symmetric mass distribution and the Monte Carlo fit. Since the mass is a function of the scale and the offset these two quantities are correlated. Figure 6.4 shows the contour of the allowed α_{EM} and δ_{EM} values for the π^0 analysis. A more detailed account of

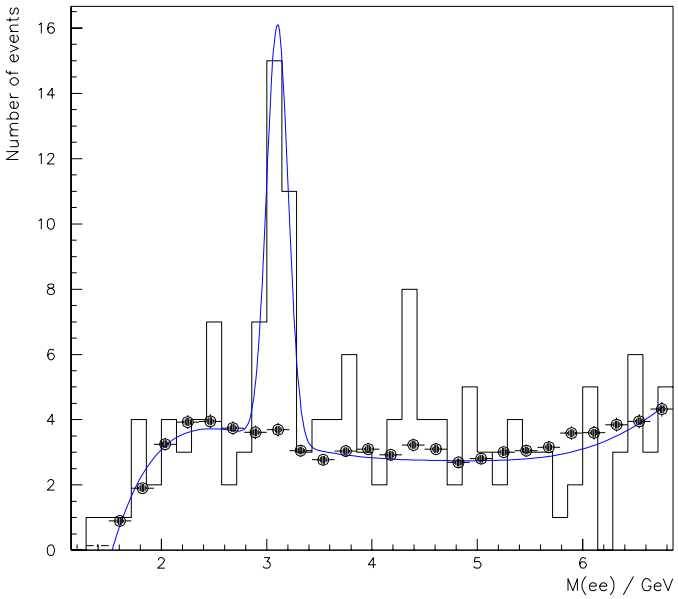

Figure 6.3: The dielectron mass distribution for the J/ψ events. The histogram is the data and the dots are the expected background. The solid line is the fit to the peak plus the background shape.

this analysis can be found in [61] and [62].

6.2.2 J/ψ

A sample of J/ψ events was collected during special runs with a low E_T di-electron trigger. Figure 6.3 shows the distribution of J/ψ events along with the expected background. The mass that is measured is $3.032 \pm 0.035(stat.) \pm 0.190(syst.)\ GeV/c^2$. The mass expected to be observed is

$$M_{Obs} = \alpha_{EM} M_{J/\psi} + f_{J/\psi} \delta_{EM} \tag{6.7}$$

with the Monte Carlo value of $f_{J/\psi}$=0.56. Figure 6.4 shows the allowed values of α_{EM} and δ_{EM} from the J/ψ analysis. A more detailed account of this analysis can be found in [63].

6.2.3 Z

The Z boson events can also be used to constrain α_{EM} and δ_{EM} because the electron energies are not monochromatic. The measured Z boson mass as a function of f_Z is shown in figure 6.5. The values in figure 6.5 are then compared with the Monte Carlo as a function of α_{EM} and δ_{EM}. Figure 6.4 shows the allowed contour from the Z boson data.

6.2.4 The Combined Result

Figure 6.4 shows the one standard deviation contour of α_{EM} versus δ_{EM} for the three data samples. The three results are combined to measure an offset of

$$\delta_{EM} = -0.16 \pm 0.03\ GeV. \tag{6.8}$$

Remember this offset is relative to the δ given in table 6.1 which would imply the δ that should be used in the sampling fractions is 0.187 GeV.

In this analysis the assumption is that equation 6.3 holds true. The test beam data does accommodate a small term in the energy response that goes as E^2. If this term is allowed to vary within the test beam limits the error on δ_{EM} becomes

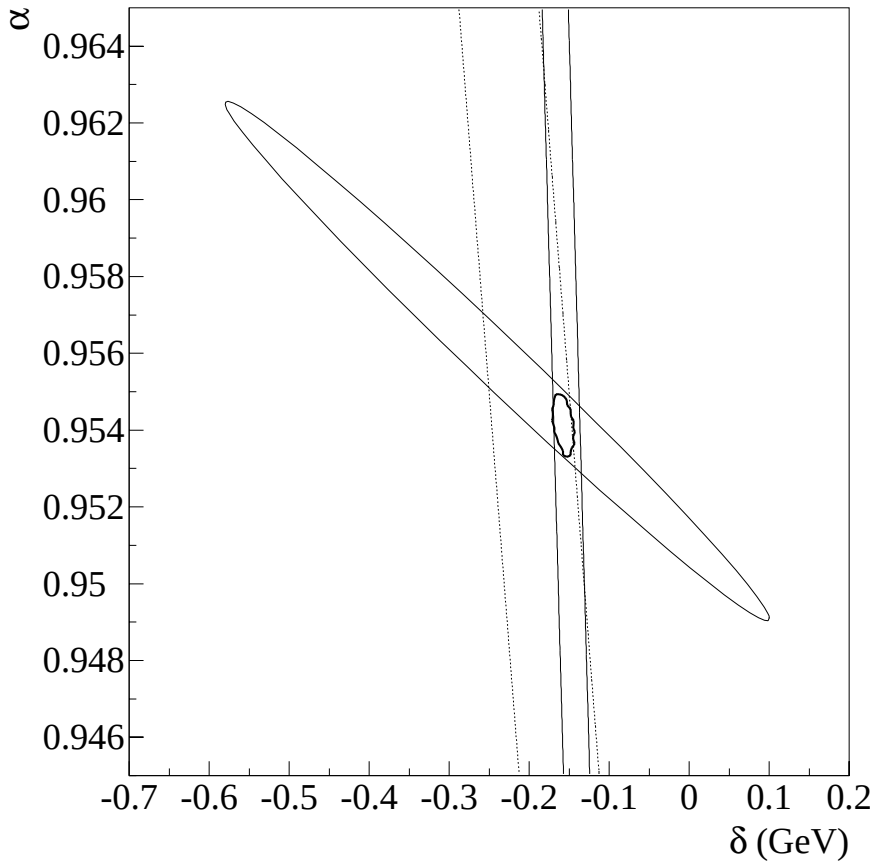

Figure 6.4: In the α_{EM}-δ_{EM} plane the 1σ contours for the three data sets. The solid ellipse lying on its side is the contour from the Z data. The thin, nearly vertical, solid ellipse is the contour for the π^0 data. The dotted ellipse is the contour for the J/ψ data. The small thick contour is the combination of all three data sets.

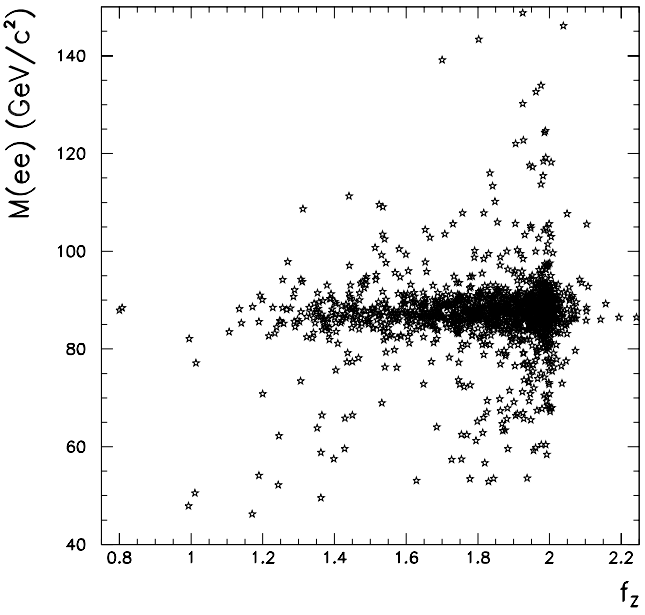

Figure 6.5: The invariant mass versus f_Z for the CC-CC Z boson events.

asymmetric and is

$$\delta_{EM} = -0.16^{+0.03}_{-0.21}\, GeV. \tag{6.9}$$

Using the Z boson data alone, the offset is determined to be $-0.25 \pm 0.35\, GeV$ which is nearly as accurate as the combined result and does not suffer from the possible higher order effects at low energy.

The π^0 and J/ψ constrain δ_{EM} in a manner which is nearly independent of α_{EM}. Therefore, when measuring α_{EM} the offset is fixed to -0.16 GeV and allow the CC-CC Z boson data alone to determine the scale. The CC-CC Z boson invariant mass spectrum is fit in the from 70 to 110 GeV/c^2. The background shape is found to be well modeled by an exponential and has a slope equal to $(-0.036 \pm 0.002)\ (GeV/c^2)^{-1}$.

The background shape was determined by selecting two electromagnetic objects which fail an electron identification requirement. The magnitude of the background in the fit is allowed to float. Figure 6.6 shows the fit to the invariant mass distribution for CC-CC Z boson events. From this fit a Z boson mass of

$$M_Z = 91.189 \pm 0.083\ GeV/c^2 \tag{6.10}$$

is measured for a scale of

$$\alpha_{EM} = 0.95372. \tag{6.11}$$

The statistical error on the Z boson mass translates into an uncertainty of 0.00091 on α_{EM}. Figure 6.7 shows the relative likelihood curve used to determine the value of α_{EM}. Figure 6.8 shows the comparison between the Monte Carlo and data as a function of the invariant mass. The variable χ is the data value minus the theory divided by the error on the data point.

The Z boson mass is insensitive to choice of the fitting window and variations in the magnitude of the background. The parton distribution functions and other systematic errors contribute a negligible amount to the uncertainty on the Z boson mass [64, 45].

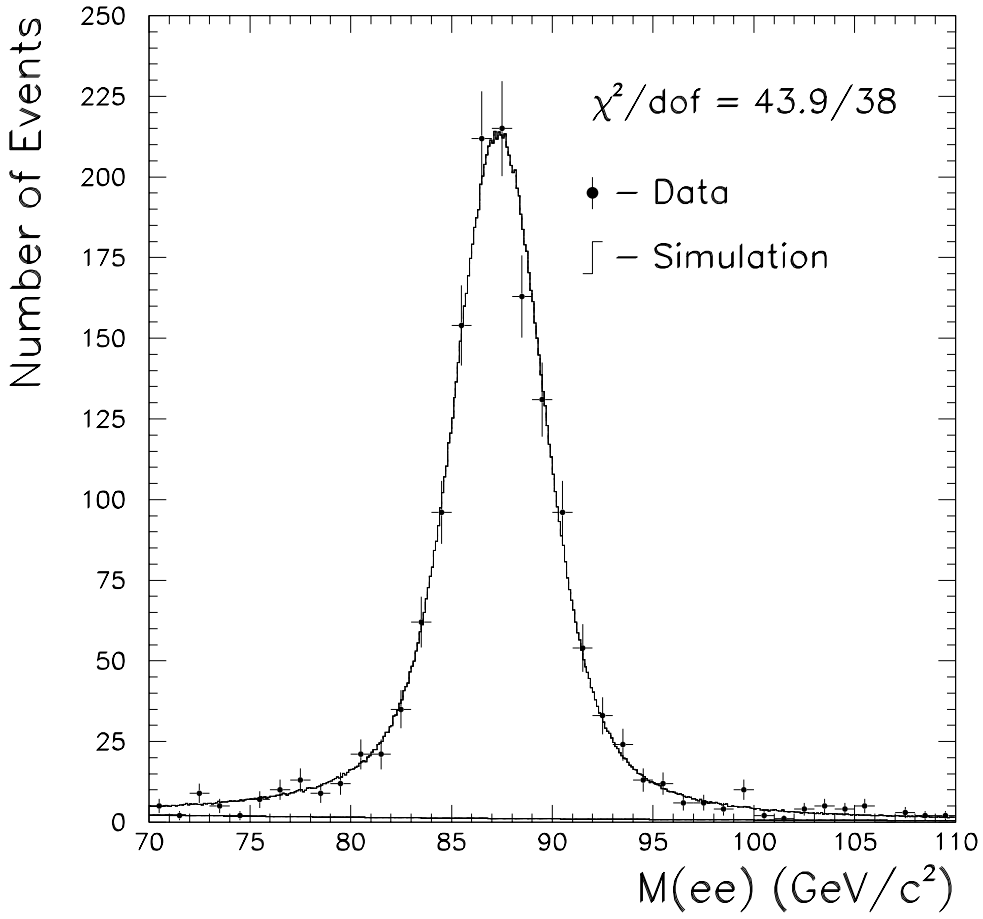

Figure 6.6: The fit to the invariant mass spectrum for the CC-CC Z boson events. The dots are the data and the solid line is the Monte Carlo simulation. The small contribution from the background is the solid line at the bottom of the distribution.

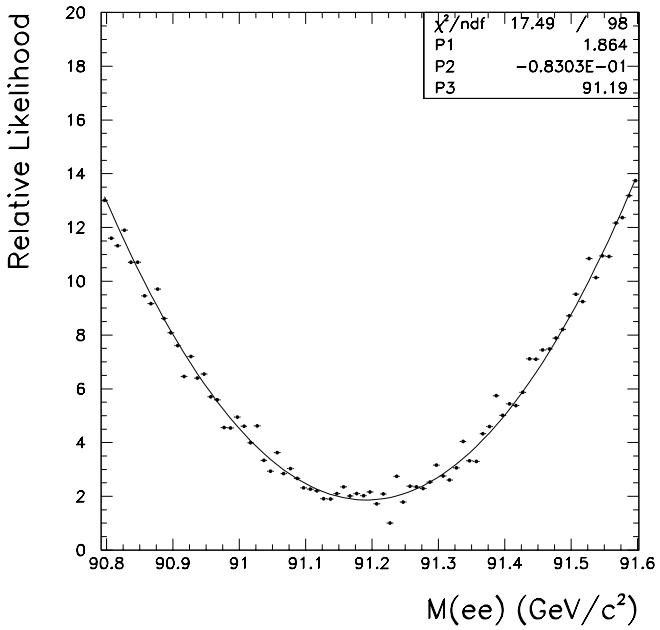

Figure 6.7: The relative likelihood distribution for the fit to the CC-CC Z boson events.

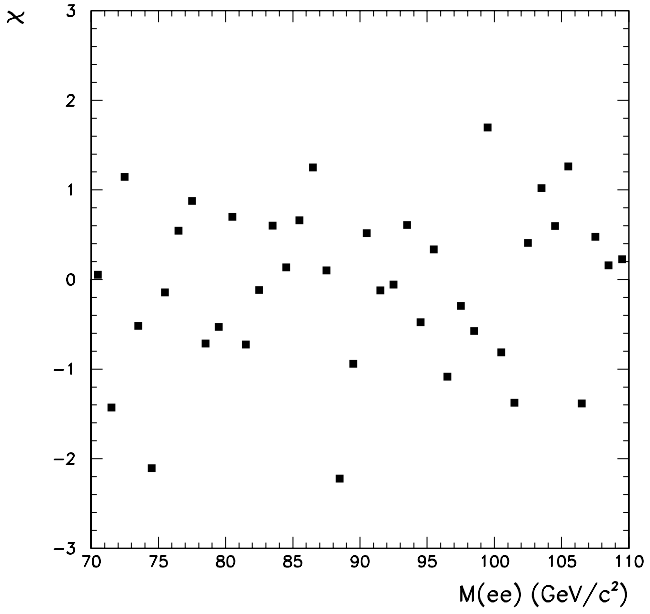

Figure 6.8: The comparison of the data and Monte Carlo versus the invariant mass. The variable χ is equal to number of events minus the number of Monte Carlo events over the square root of the number of data events.

6.3 The Effect of the Offset on the W Boson Mass

What is the effect of the error on δ_{EM} on the W boson mass? The ratio (R) of the measured W to Z boson masses is written as

$$R = \left(\frac{M_W}{M_Z}\right)^{Meas}. \tag{6.12}$$

Using equation 6.4 to write the measured W and Z boson masses as a function of the α_{EM}, δ_{EM}, and the true masses, equation 6.12 becomes

$$R \approx \frac{\alpha_{EM} M_W^{True} + f_W \delta_{EM}}{\alpha_{EM} M_Z^{True} + f_Z \delta_{EM}} \tag{6.13}$$

$$\approx \left(\frac{M_W}{M_Z}\right)^{True} + \frac{\delta_{EM}}{\alpha_{EM}} \left(\frac{f_W \cdot M_Z^{True} - f_Z \cdot M_W^{True}}{M_Z^{True} \cdot M_Z^{True}}\right) \tag{6.14}$$

where f_W and f_Z are the kinematic factors given in equation 6.5. Observe that if $\delta_{EM} = 0$ then the ratio of the true masses is equal to the ratio of the measured masses. The derivative of the ratio with respect to the offset is

$$\frac{\partial R}{\partial \delta_{EM}} \approx \frac{1}{\alpha_{EM}} \frac{(f_W \cdot M_Z^{True} - f_Z \cdot M_W^{True})}{M_Z^{True} \cdot M_Z^{True}}. \tag{6.15}$$

The true W boson mass is

$$M_W^{True} = R \cdot M_Z^{True} \tag{6.16}$$

and so the derivative of the true W boson mass with respect to the offset is

$$\frac{\partial M_W^{True}}{\partial \delta_{EM}} \approx \frac{1}{\alpha_{EM}} \frac{(f_W \cdot M_Z^{True} - f_Z \cdot M_W^{True})}{M_Z^{True}}. \quad (6.17)$$

Therefore, the effect of the offset on the W boson mass is suppressed by a factor which depends upon the W and Z boson masses and kinematics. Equation 6.17 is evaluated with the Monte Carlo and determined to be

$$\frac{\partial M_W^{True}}{\partial \delta_{EM}} \sim 0.1. \quad (6.18)$$

From equation 6.18 the error on the W boson mass due to uncertainty on δ_{EM} is 21 MeV/c^2.

6.4 Summary

The electromagnetic energy scale has been determined, for the central calorimeter, to a precision of 0.095%. The uncertainty on the energy scale is currently dominated by the statistical error on the Z boson events. The energy scale error for the W boson mass is 77 MeV/c^2, where 74 MeV/c^2 is from the statistical uncertainty of the Z boson and 21 MeV/c^2 is from the uncertainty on δ_{EM}. The data used to measure the W boson mass are corrected with a δ_{EM} of -0.16 GeV.

Chapter 7

The W Boson Mass and Systematic Errors

7.1 The W Boson Mass

The W boson mass is measured by performing a fit to the transverse mass distribution. The Monte Carlo generated probability distributions are compared to the data distribution using the maximum likelihood technique [65]. The maximum likelihood is the product of the probabilities of the events coming from a given distribution. Stated mathematically, the likelihood ($L(m)$) as a function of a given mass m is

$$L(m) = \prod_{i=1}^{N} P_i(m) \tag{7.1}$$

where $P_i(m)$ is the probability of the i^{th} event for a mass m, and N is the number of events in the data sample. In practice the negative log likelihood ($\mathcal{L}$) is used and

is given by

$$\begin{aligned} \mathcal{L} &= -\ln L \\ &= -\sum_{i=1}^{N} \ln P_i(m). \end{aligned} \tag{7.2}$$

The Monte Carlo used to generate the probability distributions was discussed in chapters 5 and 6. The mass is given by the minimum of equation 7.2 and is

$$\left.\frac{\partial \mathcal{L}}{\partial m}\right|_{M_W} = 0. \tag{7.3}$$

The error on M_W is the region allowed by the minimum of $\mathcal{L}$ plus 1/2 a unit. Figure 7.1 shows the best fit to the data and yields a W boson mass of

$$M_W = 80.346 \pm 0.069\ GeV/c^2. \tag{7.4}$$

The fitting region is the transverse mass range from 60-90 GeV/c^2. Figure 7.2 shows the relative likelihood as a function of the W boson mass. Figure 7.3 shows the χ per bin over the transverse mass fit range. No bias is observed in the χ distribution which is consistent with that expected from statistical fluctuations. The χ^2/dof is 78.6/59. The Kolmogorov-Smirnoff test [65], which is sensitive to the shape of the distribution, returns a probability of 90%.

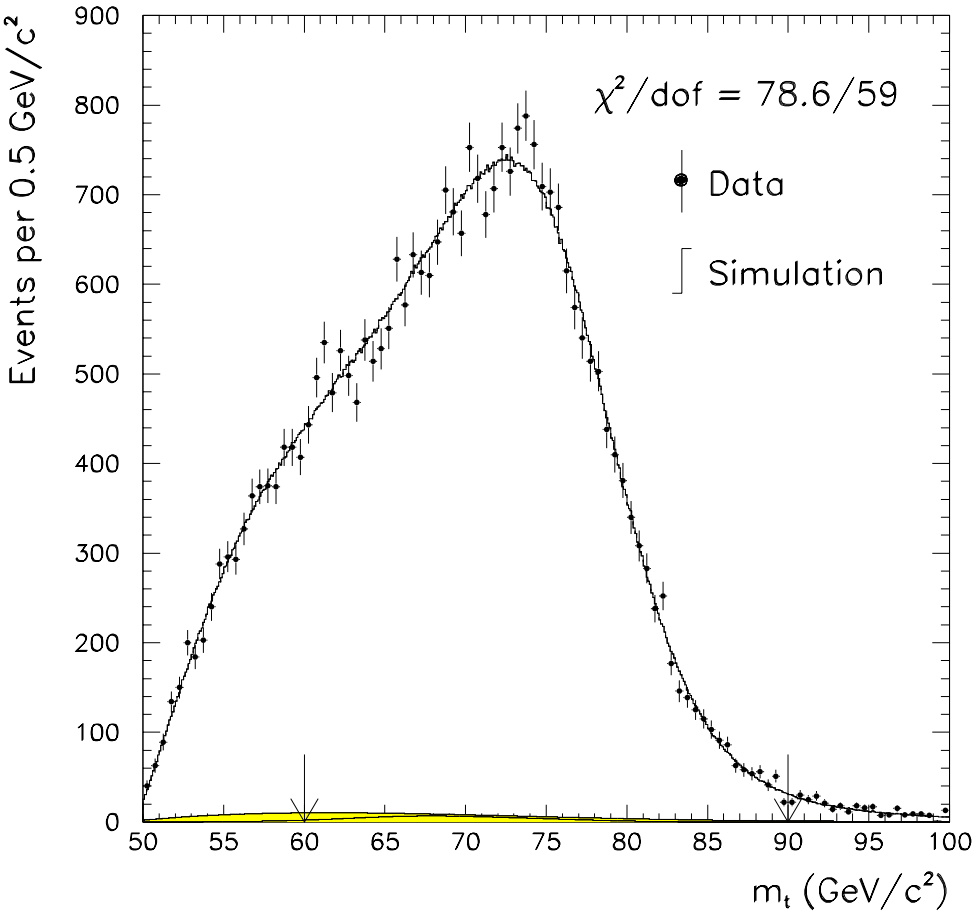

Figure 7.1: The best fit to the transverse mass distribution. The dots are the data and the solid line the Monte Carlo simulation. The shaded region at the bottom of the plot is background and the arrows indicate the fitting region.

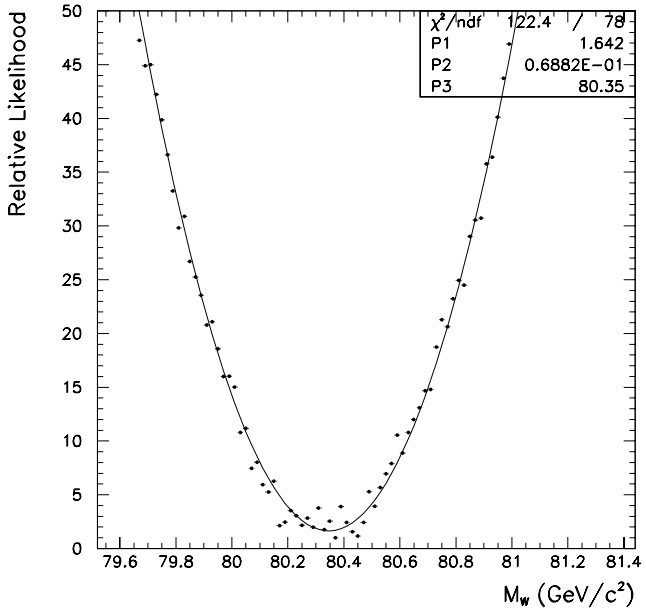

Figure 7.2: The relative likelihood distribution as a function of the W boson mass. The fit is a second order polynomial where P2 is the error and P3 the fitted mass.

7.1.1 The Lepton Fits

The W boson mass can also be measured from the fits to the E_T and $\not\!\!E_T$ distributions and are shown in figure 7.4. The observed masses are: $80.329 \pm 0.092(stat.)$ for the E_T fit and $79.741 \pm 0.126(stat.)$ for the $\not\!\!E_T$ fit. The lepton fits are used only as consistency checks on the m_t fit and will be discussed later in section 7.4.

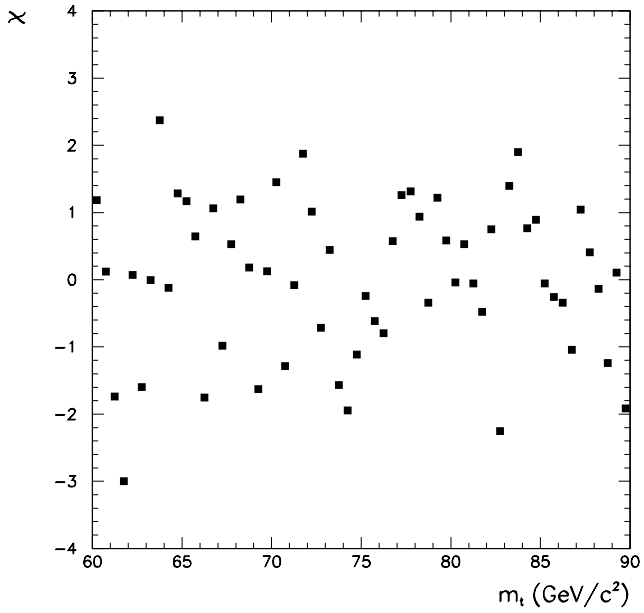

Figure 7.3: The comparison between the Monte Carlo and data as a function of the transverse mass.

7.2 Systematic Errors

In general, the evaluation of the systematic errors involves varying in the Monte Carlo a parameter within its limits and measuring the change of the W boson mass. For a particular value of a parameter the Monte Carlo is used to produce "experimental" data sets of 30,000 events. Each of these experiments is then fit with the probability functions used to measure the W boson mass. Typically 56 experiments were generated for each parameter value. Figure 7.5 shows the distribution of W boson mass fits for 56 experiments of 30,000 events for a mass of 80.400 GeV/c^2.

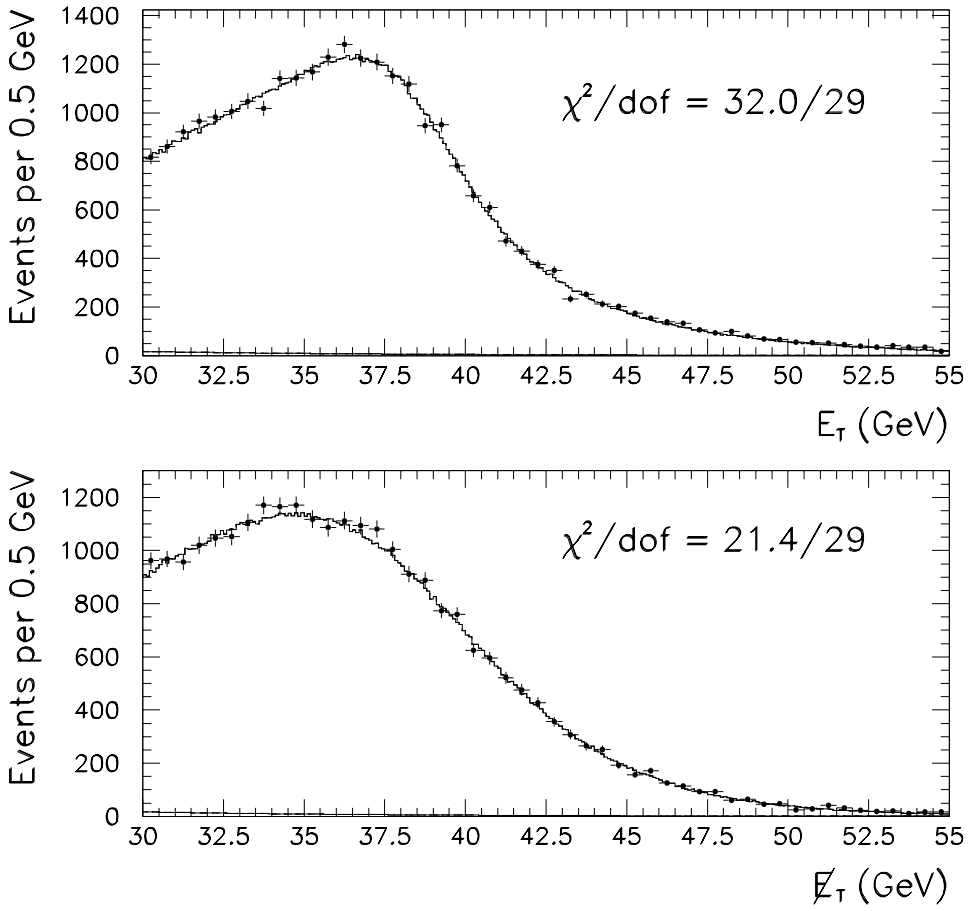

Figure 7.4: The best fit to the E_T (top) and $\not\!\!E_T$ (bottom) distributions. The fit range is from 30 to 45 GeV. The background is the falling distribution at the bottom of each plot.

These experiments were generated without any variation of the parameters and so the returned mean should be 80.400 GeV/c^2. Note the sigma of the distribution is consistent with the statistical error observed on the m_t fit from the data.

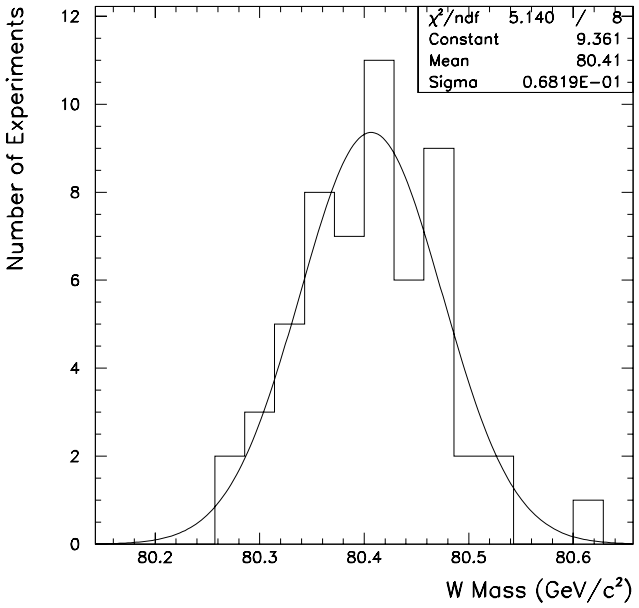

Figure 7.5: The distribution of fitted W boson masses for 56 experiments containing 30,000 events.

7.2.1 Theoretical Error

There are number of inputs to the theoretical model that have uncertainties on them which lead to systematic errors on the W boson mass. The theoretical errors are due to: the choice of $\frac{d^2\sigma}{dydp_T^W}$, the pdfs, and the parton luminosity. All three are correlated through the choice of the pdf. The radiative model also has uncertainties associated

with it since it involves a cutoff parameter γ_{Min}.

The $\frac{d^2\sigma}{dydp_T^W}$ Model

The model $\frac{d^2\sigma}{dydp_T^W}$ has three parameters, g_1, g_2, and g_3, which parameterize the non-perturbative physics [23]. The p_T^W spectrum is found to be most sensitive to the parameter g_2. To measure g_2 the Monte Carlo p_T^{ee} distribution, from Z boson events, is compared with the data. Figure 7.6 shows the p_T^Z distribution for two extreme values of g_2. The method for constraining g_2 can be found in reference [66]. The error on g_2 is taken to be $\pm 2\sigma$ where σ is the value from reference [23]. Table 7.1 shows the variation of the W boson mass as a function of g_2 for the m_t fit and table 7.2 for the lepton fit. An error of 12 MeV/c^2 is assigned to the error on the W boson mass due to the uncertainty on g_2 for the m_t fit, and 61 MeV/c^2 for the lepton fit.

PDFs

The pdfs are partially constrained though the W boson asymmetry [67]. To evaluate the uncertainty of the pdf, due to the error on the asymmetry data, the CTEQ [68] collaboration has provided special versions of their CTEQ3M pdf for two different assumptions on the asymmetry data points. The asymmetry data is from the CDF [69] collaboration. A special version of the pdf is determined by simultaneously increasing each data point by its error and rederiving the pdf. This pdf is called "asymmetry high". The second pdf is when all the data points are simultaneously decreased, and so this pdf is called "asymmetry low". Table 7.1 shows the variation of the W

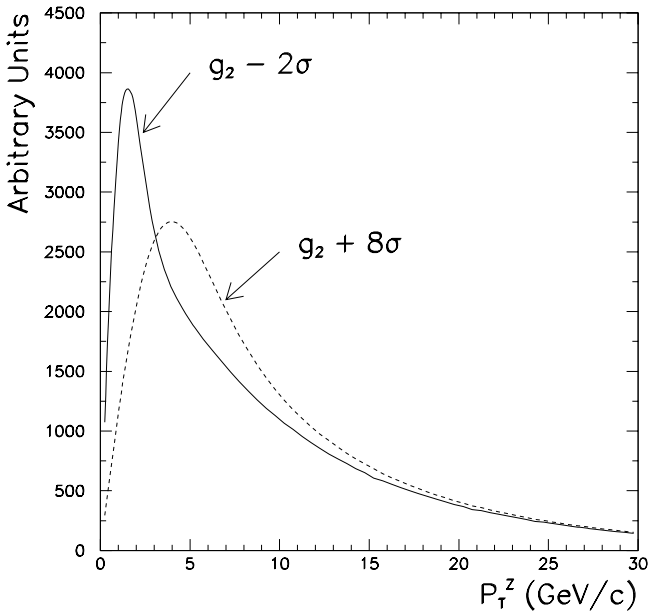

Figure 7.6: The variation of the p_T^Z distribution for two large excursions of the g_2 parameter.

boson mass for the three CTEQ3M pdfs, and as a function of g_2. The variation in the asymmetry leads to an error of $\sim 40\ MeV/c^2$ on the W boson mass. Since the probability of all the asymmetry points fluctuating coherently by one sigma is small, a conservative error of 20 MeV/c^2 is assigned for the uncertainty on the asymmetry to account for the effect on the pdfs. From table 7.2 the error on the lepton fits is taken to be 90 MeV/c^2.

The error on the W boson mass due to the choice of pdf is determined from the variation in the mass for the modern pdfs. Table 7.3 lists the variation of the W boson mass for the modern pdfs relative to the MRSA value. Without the ability to

$\delta M_W(MeV/c^2)$	$g_2 - 2\sigma$	g_2	$g_2 + 2\sigma$	$g_2 + 4\sigma$
Asymmetry Low	56±11	40±11	23±11	27±11
Asymmetry Nominal	9±6	0	-14±6	-21±6
Asymmetry High	-65±11	-51±11	-63±11	-52±11

Table 7.1: The variation of the W boson mass for the m_t fit as a function of g_2 and different assumptions of the asymmetry for the CTEQ3M pdf.

$\delta M_W(MeV/c^2)$	$g_2 - 2\sigma$	g_2	$g_2 + 2\sigma$	$g_2 + 4\sigma$
Asymmetry Low	149±14	126±14	33±14	4±14
Asymmetry Nominal	62±9	0	-59±9	-126±9
Asymmetry High	-40±14	-71±14	-145±14	-193±14

Table 7.2: The variation of the W boson mass for the lepton transverse momentum fit as a function of g_2 and different assumptions of the asymmetry for the CTEQ3M pdf.

further select a pdf the maximum variation between the pdfs is taken as the error on the W boson mass. For the transverse mass this is 48 MeV/c^2 and the lepton fits 150 MeV/c^2.

	Fit Variable	
PDF	m_t	E_T
MRSA	0	0
MRSD-'	-2±14	-26±20
CTEQ3M	-48±11	-150±15

Table 7.3: The variation of the W boson mass from the different pdfs. The center column is the transverse mass fit and the right column the lepton E_T fits.

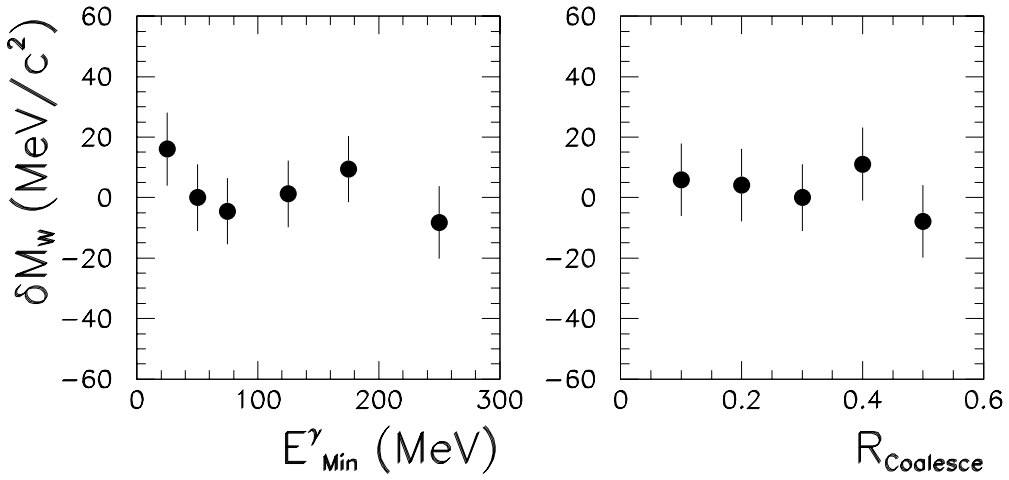

Figure 7.7: The variation of the W boson mass as a function of γ_{Min} (left) and $R_{Coalesce}$ (right).

Parton Luminosity

The parton luminosity changes the shape of the invariant mass distribution which translates into a change in the transverse mass lineshape. The parton luminosity parameter (β) is assigned a 25% error to cover the uncertainty in its calculation. This leads to an error on the W boson mass of 10 MeV/c^2.

Radiation

There are two components to the uncertainty on the W boson mass from the radiative events. The first is from the parameter γ_{Min} used in the calculation and the second is from the detector effect which forces the use of the parameter $R_{Coalesce}$. Figure 7.7 shows the variation of the W boson mass as a function of these parameters. From the variation shown in figure 7.7 and reference [70] an error of 20 MeV/c^2 is assigned to the error on the W boson mass due to radiative decays. Table 7.4 summarizes

Uncertainty	$\delta M_W(MeV/c^2)$	
	m_t	E_T
$\frac{d^2\sigma}{dydp_T^W}$ Model	12	61
Asymmetry	20	90
Parton Distribution Functions	48	150
Parton Luminosity	10	10
Radiative Decays	20	40
Total	58	190

Table 7.4: A summary of the theoretical uncertainties on the W boson mass measurement.

the theoretical errors on the W boson mass measurement.

7.2.2 Detector Effects

The inputs to the Monte Carlo have been evaluated to measure their sensitivity on the W boson mass. For incidence, figure 7.8 shows the variation, or derivative, of the W boson mass with respect to the hadronic response for the m_t and $\not\!\!E_T$ fits. The derivative $\left(\frac{\partial M_W}{\partial \alpha_H}\right)$ is measured to be 16.6 $\frac{MeV/c^2}{0.01}$ for m_t fit and -28.5 $\frac{MeV/c^2}{0.01}$ for the $\not\!\!E_T$ fit. The hadronic response is an interesting quantity in that the m_t and $\not\!\!E_T$ anti-correlate, whereas most parameters tend to be correlated. Table 7.5 lists the systematic errors, the derivative of the W boson mass with respect to the parameter, and the error on the W boson mass for the m_t fit. Table 7.6 shows the same items for the lepton fits. If the variation of the W boson mass with respect to a parameter is not linear the error is symmetrized by assigning it to the largest value. An example of this is shown in figure 7.9 which is the variation of the W boson mass with respect to the electromagnetic constant term.

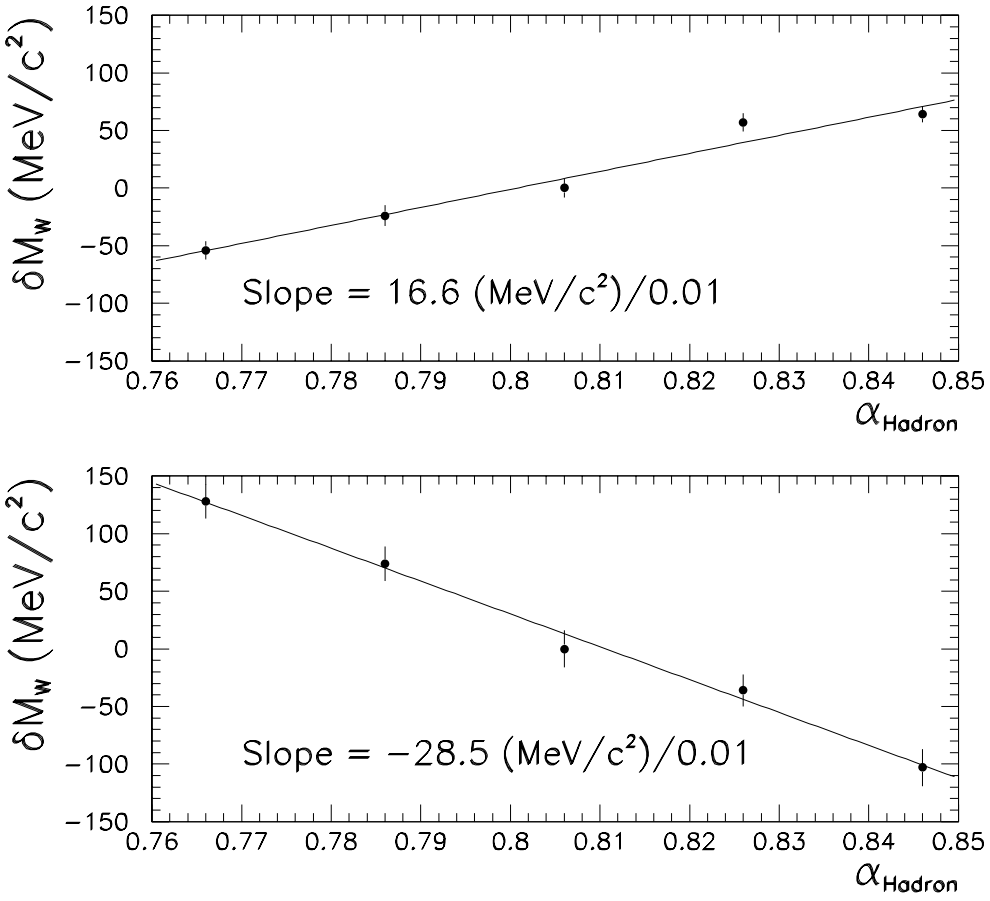

Figure 7.8: Variation of the W boson mass as a function of α_H for the transverse mass (top plot) and the neutrino (bottom plot) fits.

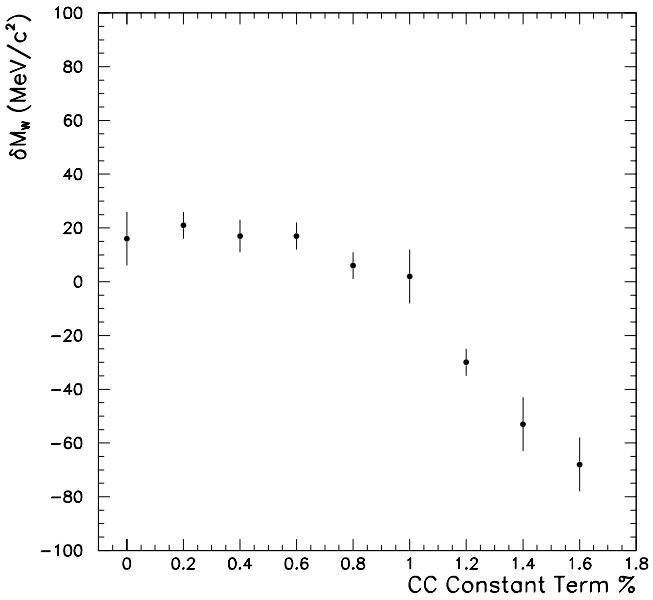

Figure 7.9: The variation of the W boson mass as a function of the electromagnetic constant term for the m_t fit. The difference is with respect to the nominal value at 0.9%.

Occasionally the derivative is evaluated on the ratio of the W and Z boson masses to take advantage of the cancelations that occur between the W and Z boson. An example of this is the error from the CDC scale. The error on the W boson mass, when the ratio is used, is 38 MeV/c^2. If the ratio was not used then the error on the W boson mass would have been 76 MeV/c^2. In this case the ratio gives a substantial reduction in the error.

Many of the parameters in the Monte Carlo are correlated but most are not strongly correlated. Since S_H and MB both smear the hadronic recoil they are

strongly correlated, see figure 5.8. This correlation is taken into account when the error is evaluated. The error on the W boson mass may be written as follows

$$\delta_M^2 = \left(\frac{\partial M}{\partial S_H}\delta_{S_H}\right)^2 + \left(\frac{\partial M}{\partial MB}\delta_{MB}\right)^2 + 2 \cdot \left(\frac{\partial M}{\partial S_H}\right)\left(\frac{\partial M}{\partial MB}\right) \cdot cov(S_H, MB) \quad (7.5)$$

where $\frac{\partial M}{\partial X}$ is the change of the W boson mass with respect to the variable $X = \{S_H, MB\}$, δ_X is the error on variable, and $cov(S_H, MB)$ is the covariance of S_H and MB. The correlation coefficient (ρ) given in terms of the covariance is

$$\rho = \frac{cov(S_H, MB)}{\delta_{S_H}\delta_{MB}} \quad (7.6)$$

$$= -0.5876. \quad (7.7)$$

Using equation 7.5, correlation coefficient, and the derivatives and parameters given in table 7.5 the error on the W boson mass from S_H and MB is determined to be 32 MeV/c^2.

7.3 Backgrounds

The background to the sample has two components: from QCD jets and $Z \rightarrow ee$ events. The QCD background occurs when a jet fakes a high p_T electron and detector effects produce significant missing p_T. The $Z \rightarrow ee$ background occurs when one of the electrons is lost producing missing E_T. All other backgrounds are negligible.

7.3.1 QCD Background

To measure the QCD background the EM1_ELE_MON trigger is used. This trigger had loose electron requirements and no missing p_T cut. From these events the $\not\!\!E_T$ is plotted for events passing the W boson selection criteria. These are called "good" events. Two regions are defined in the $\not\!\!E_T$ distribution: the signal region is $25 < \not\!\!E_T < 60\ GeV$, and a normalization region, $\not\!\!E_T < 15\ GeV$. A sample of "bad" events is selected by requiring $\chi^2 > 200$ and $\sigma_{Track} > 10$. The good and bad samples are normalized to the same number of events in the normalization region. Figure 7.10 shows the $\not\!\!E_T$ distribution for the good and bad events normalized in this region. The background is taken to be the ratio of the number of bad events to the number of good events in the signal region. The background was measured as a function of the luminosity and is shown in figure 7.11. The total QCD background, weighted by the luminosity distribution of W boson events, is $(1.5 \pm 0.3)\%$. The error of 0.3% is from the variation of the points in figure 7.11.

The shape of the QCD background has been measured in two ways. One method uses the bad events in the signal region and the distribution of their transverse mass. The second method selected fake electrons using the TRD and then plotted the transverse mass of these events. The background to the lepton fits are well represented by an exponential with a slope of -0.08 for the E_T fit and -0.10 for the $\not\!\!E_T$ fit.

The error on the W boson mass is taken as the combination of the error on the normalization and variations on the allowed background shape, and for the m_t fit is

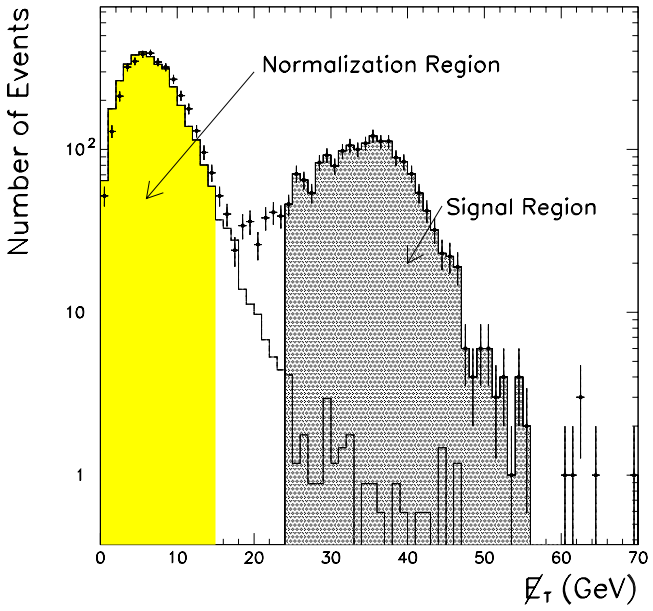

Figure 7.10: The $\not\!\!E_T$ distribution of the good (dots) and bad (solid histogram) events. The two samples are normalized in the low $\not\!\!E_T$ region. The amount of background is the ratio of the number of events in the signal region.

13 MeV/c^2.

7.3.2 $Z \rightarrow ee$

The $Z \rightarrow ee$ background, where one of the electrons is lost, is determined by using ISAJET Z boson events and putting them through the GEANT simulation. The $\not\!\!E_T$ for the GEANT simulated events was smeared to match the $\not\!\!E_T$ observed in the data. The W boson selection cuts were then applied to the GEANT simulated

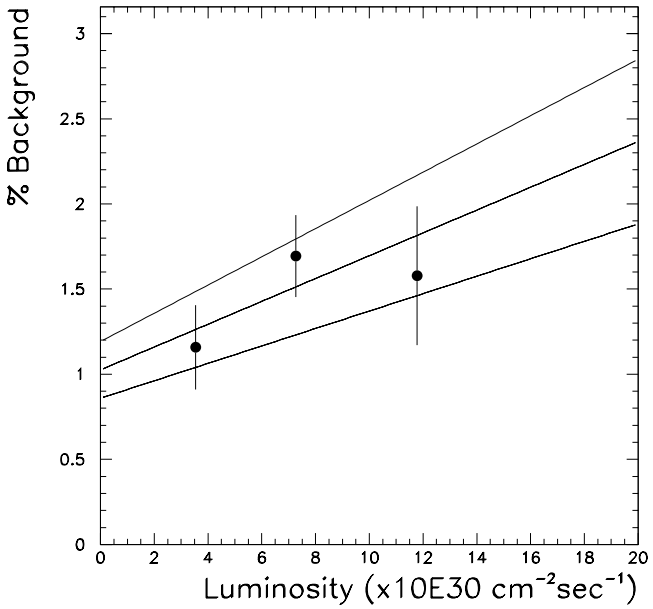

Figure 7.11: The QCD background as a function of the luminosity. The luminosity bins are 0-5, 5-10, and 10+ in units of $10^{30} cm^{-2} sec^{-1}$.

events and the background is found to be $(0.55 \pm 0.05)\%$.

Tables 7.5 and 7.6 summarize the effect of the backgrounds on the W mass measurement.

7.4 Consistency Checks

A number of consistency checks have been done to test the stability of the W boson mass value. The mass is measured with the data divided into sub-samples based on an interesting quantity to see how it varies.

Fitting Window

The upper and lower values of the fitting window has been varied over a large range. Figure 7.12 shows the change in mass for different values of the fitting window relative to the nominal value. The W boson mass only begins to move appreciably for fitting windows that are high up on the distribution or way out on the tail.

ϕ Dependence

The data are broken into 32 parts corresponding to the ϕ modules of the central calorimeter. The mass of each subsample, each having approximately 1000 events, is measured and is shown in figure 7.13. Because of the Main Ring a dependence on ϕ may have occurred but none is observed. The RMS of the fit values has two components: one from the statistical error of the mass measurements and the other from the variation in the response of the CC ϕ modules. The RMS of the points in figure 7.13 is 605 MeV/c^2 and the statistical error of each point is 380 MeV/c^2. This gives the ϕ module variation of 0.6% which is in excellent agreement with the 0.5% given as the uncertainty on the CC ϕ module calibration constants determined in reference [51].

η Dependence

Fits have been performed on the data for which a more restrictive η cut was applied to the electron. For this study the Monte Carlo also had the cut applied to the electron(s). The W boson mass, measured from the ratio, as a function of the η

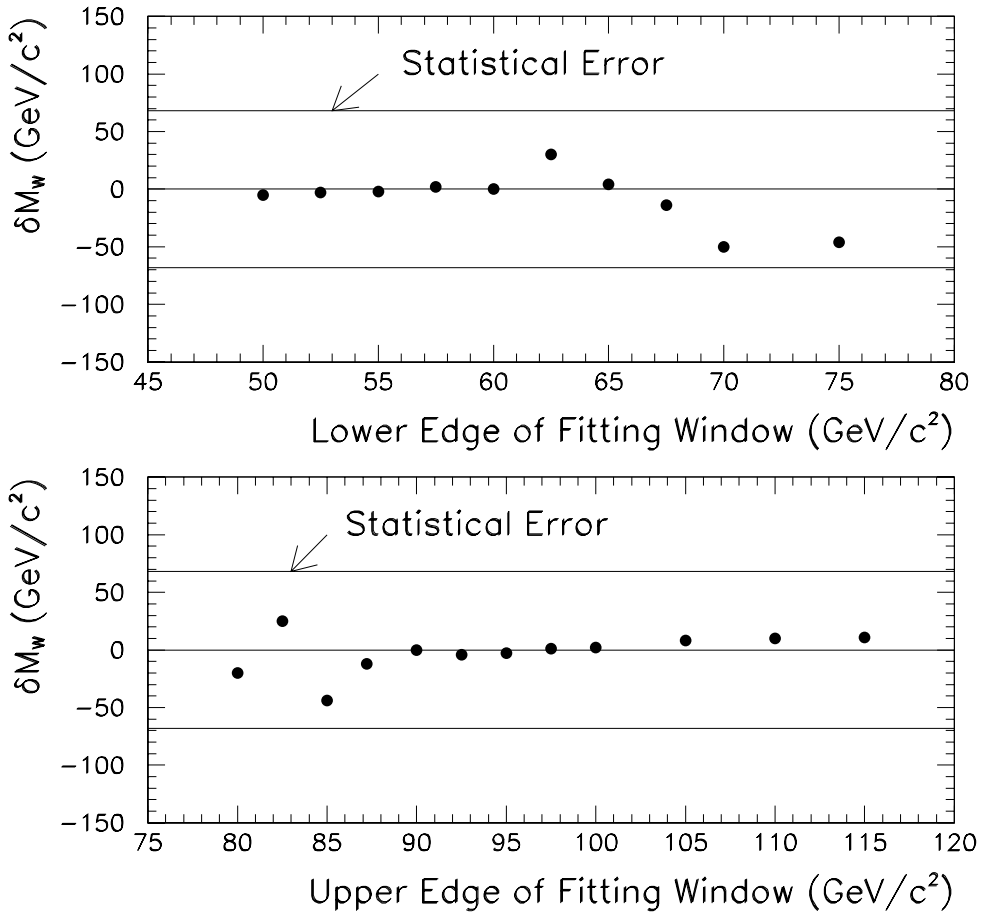

Figure 7.12: The variation in the mass as a function of the fitting window. For the top plot the fit range is from the points to 90 GeV/c^2 and for the bottom plot is the fit from 60 GeV/c^2 to the point on the plot.

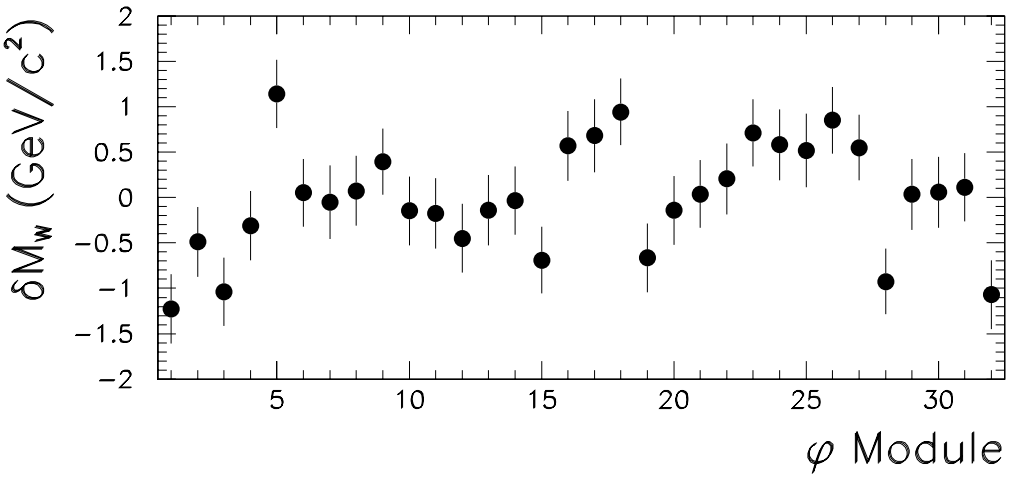

Figure 7.13: The variation of the W boson mass as a function of the ϕ module of the central calorimeter.

cut is shown in figure 7.14. The values in figure 7.14 are relative to the point at $\eta = 1.0$ which is the nominal value. The errors on the points are statistical only. No dependence on the mass as a function of the η cut is observed.

Comparison with the Lepton Mass Fits

The W boson mass extracted from the lepton fits is used as a consistency check of the m_t fit. The statistical error on the difference of the W boson masses is determined from the Monte Carlo for the m_t and lepton fits. For 30,000 events the RMS of the difference between the mass values from the m_t and E_T fits is 94 MeV/c^2 and between the m_t and $\not\!\!E_T$ fits is 115 MeV/c^2. The difference in the W boson masses from the m_t and E_T fits is

$$\Delta M_W(m_t, E_T) \;=\; 17 \pm 94(stat.) \pm 150(syst.)\, MeV/c^2 \qquad (7.8)$$

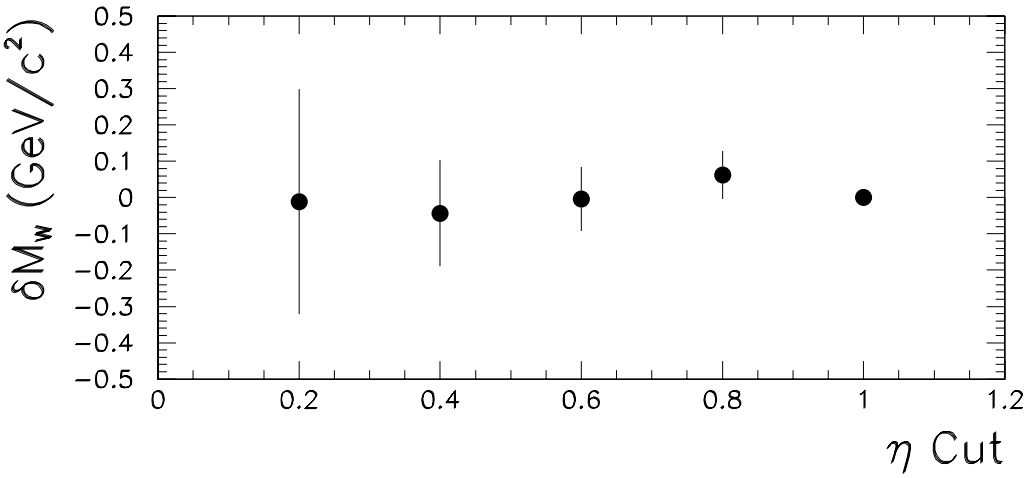

Figure 7.14: The variation of the W boson mass as a function of the lepton rapidity cut.

$$= \quad 17 \pm 177\ MeV/c^2 \tag{7.9}$$

and between the m_t and $\not\!\!E_T$ is

$$\Delta M_W(m_t, \not\!\!E_T) = 605 \pm 115(stat.) \pm 167(syst.)\ MeV/c^2 \tag{7.10}$$

$$= 605 \pm 203\ MeV/c^2 \tag{7.11}$$

and between the lepton fits is

$$\Delta M_W(E_T, \not\!\!E_T) = 588 \pm 155(stat.) \pm 141(syst.)\ MeV/c^2 \tag{7.12}$$

$$= 588 \pm 210\ MeV/c^2. \tag{7.13}$$

The systematic errors are evaluated using the derivatives in tables 7.5 and 7.6. The statistical significance of $\Delta M_W(m_t, E_T)$, $\Delta M_W(m_t, \not\!\!E_T)$, and $\Delta M_W(E_T, \not\!\!E_T)$, is 0.10, 2.98 and 2.80$\sigma$ respectively.

Luminosity Dependence

The Tevatron Run 1b more than doubled the highest instantaneous luminosity at which data had been collected at DØ. In the Monte Carlo several of the parameters are implemented in a luminosity dependent way. For example the underlying event correction and the minimum bias events that are added to the Monte Carlo depend upon the luminosity at which the W boson was taken. Errors in the application of these luminosity dependent effects could be observed when the data is divided into luminosity regions. The data are broken into four luminosity bins each with roughly the same number of events. These regions are 0-5, 5-7, 7-9, and 9+ in units of $10^{30} cm^{-2} sec^{-1}$. The Monte Carlo is run with the luminosity distribution relevant for each bin. Figure 7.15 shows the Z boson mass as a function of the luminosity. No dependence on the Z boson mass on the luminosity is observed. Figure 7.16 shows the W boson mass as a function of the luminosity for the m_t, E_T, and $\not\!\!E_T$ fits. The W boson mass in the last luminosity bin of the $\not\!\!E_T$ distribution is much lower than other three points. The question becomes how does this effect the W boson mass extracted from the m_t fit? If the W boson mass is fit using only the data in the first three luminosity bins, for the m_t fit, a mass of 80.436 GeV/c^2 is observed. Statistically, the change in the W boson mass one would expect from removing the events in the last luminosity bin is 44 MeV/c^2. Thus, the change observed is a two sigma effect. A variation of this size may be statistical but also warrants further investigation of the hadronic resolutions in the high luminosity environment.

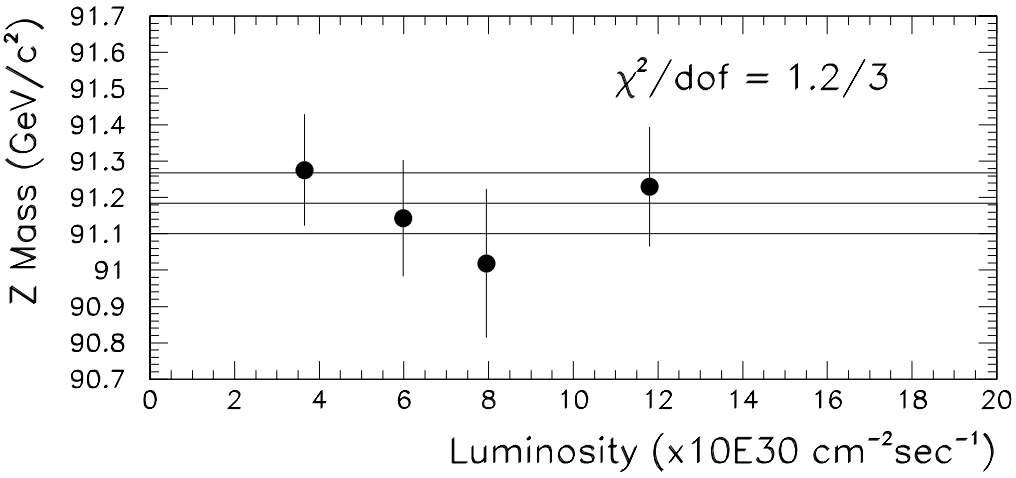

Figure 7.15: The Z boson mass as a function of the luminosity. The central line in the fit is the mean value of the four data points and the two outer lines the statistical error.

7.5 Summary

The W boson mass from the m_t mass distribution is measured to be $80.346 \pm 0.067(stat.) \pm 0.091(syst.)$ GeV/c^2. The mass has been found to be stable when divided into sub-samples and variations of the fitting window. The fits to the electron and neutrino p_T distributions give $80.329 \pm 0.092(stat.) \pm 0.196(syst.)$ and $79.741 \pm 0.126(stat.) \pm 0.236(syst.)$, respectively. All three fits have a common 0.077 GeV/c^2 energy scale error. Table 7.5 summarizes the systematic errors on the W boson mass.

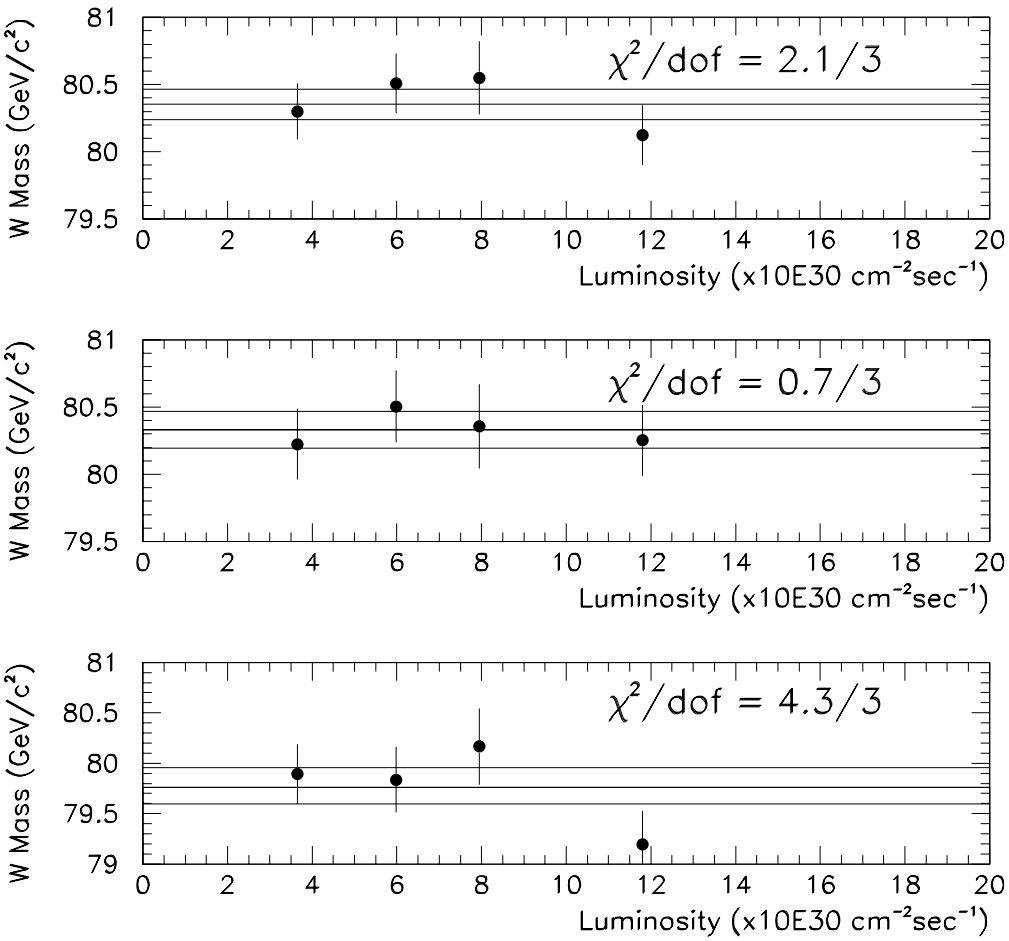

Figure 7.16: The W boson mass as a function of the luminosity. The top plot is for the m_t fit, the middle plot the E_T fit, and the bottom plot the $\not\!\!E_T$ fit. The central line in each fit is the mean value of the four data points and the two outer lines the statistical error.

Parameter	**Value and Error**	$\frac{\partial M_W}{\partial P}$	δM_W (MeV/c^2)
CC Constant Term	$\mathcal{C} = 0.9^{+0.30}_{-0.45}\%$	-7.3 $\frac{MeV/c^2}{0.1\%}$	22
Hadronic Response	$\alpha_H = 0.810 \pm 0.016$	16.6 $\frac{MeV/c^2}{0.01}$	27
Hadronic Sampling Term	$\mathcal{S}_H = 49 \pm 14\%$	-12.8 $\frac{MeV/c^2}{10\%}$	18
# Minimum Bias Events	$MB = 1.01 \pm 0.03$	-13.1 $\frac{MeV/c^2}{0.01}$	39
$\Delta U_{\|\|}$ Correction	$\Delta U_{\|\|} = 460 \pm 25\ MeV/c$	1.1 $\frac{MeV/c^2}{1MeV/c}$	28
$U_{\|\|}$ Efficiency Slope	$\epsilon = 0.013 \pm 0.001$	2.7 $\frac{MeV/c^2}{0.001}$	< 5
W Natural Width	$, _W = 2.06 \pm 0.06\ GeV/c^2$	-15.9 $\frac{MeV/c^2}{0.1GeV/c^2}$	10
CDC Z Scale	$S_{CDC} = 0.988 \pm 0.002$	18.6 $\frac{MeV/c^2}{0.001}$	37
Trigger Efficiencies	Spread	–	15
QCD Background	$1.5 \pm 0.3\%$	–	13
Z Background	$0.55 \pm 0.05\%$	–	< 5
Theoretical	Table 7.4	–	58
			91

Table 7.5: The systematic errors on the W mass using the transverse mass distribution. The total error of 91 MeV/c^2 is evaluated with all the errors taken in quadrature except for the uncertainty from $\mathcal{S}_H$ and MB which combined is 32 MeV/c^2.

Fit Type	Electron E_T		Missing p_T	
Parameter	$\frac{\partial M_W}{\partial P}$	δM_W	$\frac{\partial M_W}{\partial P}$	δM_W
CC Constant Term	3.1 $\frac{MeV/c^2}{0.1\%}$	9	-5.7 $\frac{MeV/c^2}{0.1\%}$	17
Hadronic Response	-0.1 $\frac{MeV/c^2}{0.01}$	< 5	-28.5 $\frac{MeV/c^2}{0.01}$	46
Hadronic Sampling Term	-0.6 $\frac{MeV/c^2}{10\%}$	< 5	-24.5 $\frac{MeV/c^2}{10\%}$	34
# Minimum Bias Events	2.6 $\frac{MeV/c^2}{0.01}$	8	-34.9 $\frac{MeV/c^2}{0.01}$	105
$\Delta U_{\|\|}$ Correction	0.1 $\frac{MeV/c^2}{1MeV/c}$	< 5	2.1 $\frac{MeV/c^2}{1MeV/c}$	53
$U_{\|\|}$ Efficiency Slope	-8.5 $\frac{MeV/c^2}{0.001}$	9	16.9 $\frac{MeV/c^2}{0.001}$	17
W Natural Width	-15.9 $\frac{MeV/c^2}{0.1GeV/c^2}$	10	-15.9 $\frac{MeV/c^2}{0.1GeV/c^2}$	10
CDC Z Scale	18.6 $\frac{MeV/c^2}{0.001}$	37	18.6 $\frac{MeV/c^2}{0.001}$	37
Trigger Efficiencies	–	15	–	15
QCD Background	–	15	–	18
Z Background	–	8	–	6
Theoretical	–	190	–	190
		196		236

Table 7.6: The systematic errors on the lepton p_T fits. The values of the errors are shown in table 7.5.

Chapter 8

Conclusion

8.1 The W Boson Mass

The W boson mass, measured in $W \rightarrow e\nu$ decays with the transverse mass spectrum, is

$$80.346 \pm 0.069(stat.) \pm 0.091(syst.) \pm 0.077(scale)\ GeV/c^2 \quad (8.1)$$

$$80.346 \pm 0.137\ GeV/c^2. \quad (8.2)$$

This thesis describes currently the single most precise measurement of W boson mass. Figure 8.1 shows the most recent W boson mass measurements. This measurement is combined with the previous values and presented.

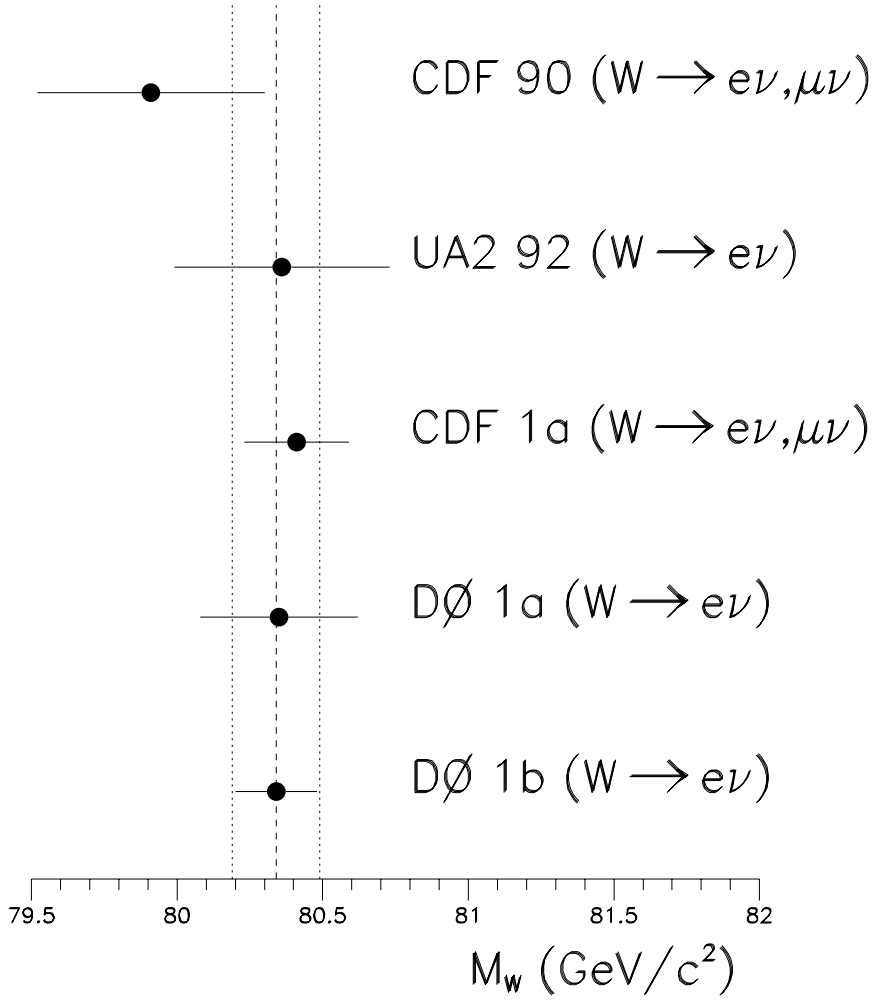

Figure 8.1: The current measurements of the W boson mass. The vertical lines are the world average and error before this measurement.

8.2 Combined W Boson Mass

To combine the Run 1a and 1b W boson mass measurements from DØ the procedure given in [71] is used. The mass may be written in terms of its errors as

$$M_W^i \pm \delta M_W^i \pm \delta M_W^{com} \tag{8.3}$$

where M_W^i is the mass of the i^{th} measurement, δM_W^i is the uncorrelated error, and δM_W^{com} is the common error between the measurements. To combine the DØ 1a and 1b measurements the weighted average is evaluated with the uncorrelated errors and is given by

$$M_W^{D\emptyset} = \frac{M_W^{1a}/(\delta M_W^{1a})^2 + M_W^{1b}/(\delta M_W^{1b})^2}{1/(\delta M_W^{1a})^2 + 1/(\delta M_W^{1b})^2} \tag{8.4}$$

with the error on $M_W^{D\emptyset}$ being

$$\delta M_W^{D\emptyset} = \sqrt{\frac{1}{1/(\delta M_W^{1a})^2 + 1/(\delta M_W^{1b})^2} + (\delta M_W^{com})^2}. \tag{8.5}$$

The uncorrelated and common errors between the Run 1a and 1b W mass measurements are shown in table 8.1. Using the results of table 8.1, $M_W^{1a} = 80.35\ GeV/c^2$, and equation 8.2 in equations 8.4 and 8.5 the combined DØ W boson mass is

$$M_W^{D\emptyset} = 80.347 \pm 0.130\ GeV/c^2. \tag{8.6}$$

Source	Run 1a	Run 1b	Common
W Statistics	140	67	
Z Statistics	160	74	
Offset(δ_{EM})			21
CC Constant Term	70	22	
Hadronic Resolution	88	32	
Hadronic Response	50	27	
$\Delta U_{\parallel}$ Correction	35	28	
CDC Z Scale	34		37
Efficiencies	30	15	
Backgrounds	34	14	
Theoretical	35		62
Total (MeV/c^2)	257	116	75

Table 8.1: Summary of the errors on the Run 1a and 1b W boson mass measurements.

This measurement is now combined with the results of other experiments, listed in table 8.2 [55], and found to be

$$M_W^{World} = 80.341 \pm 0.123\ GeV/c^2 \tag{8.7}$$

where the common error used is 85 MeV/c^2. Figure 8.2 shows the allowed Higgs

W Mass (GeV/c^2)	Experiment	Uncorrelated Error (MeV/c^2)
79.91±0.39	CDF 90	385
80.36±0.37	UA2 92	360
80.410±0.180	CDF 1a	173
80.347±0.130	DØ 1a/1b	114

Table 8.2: Summary of recent W boson mass measurements.

mass values for the current world average W boson mass from equation 8.7 and top quark mass [20, 72] of 174±7 GeV/c^2. Though the contour in figure 8.2 is narrowing the precision of the W boson and top quark masses is insufficient to put any definitive constraints on the Higgs mass.

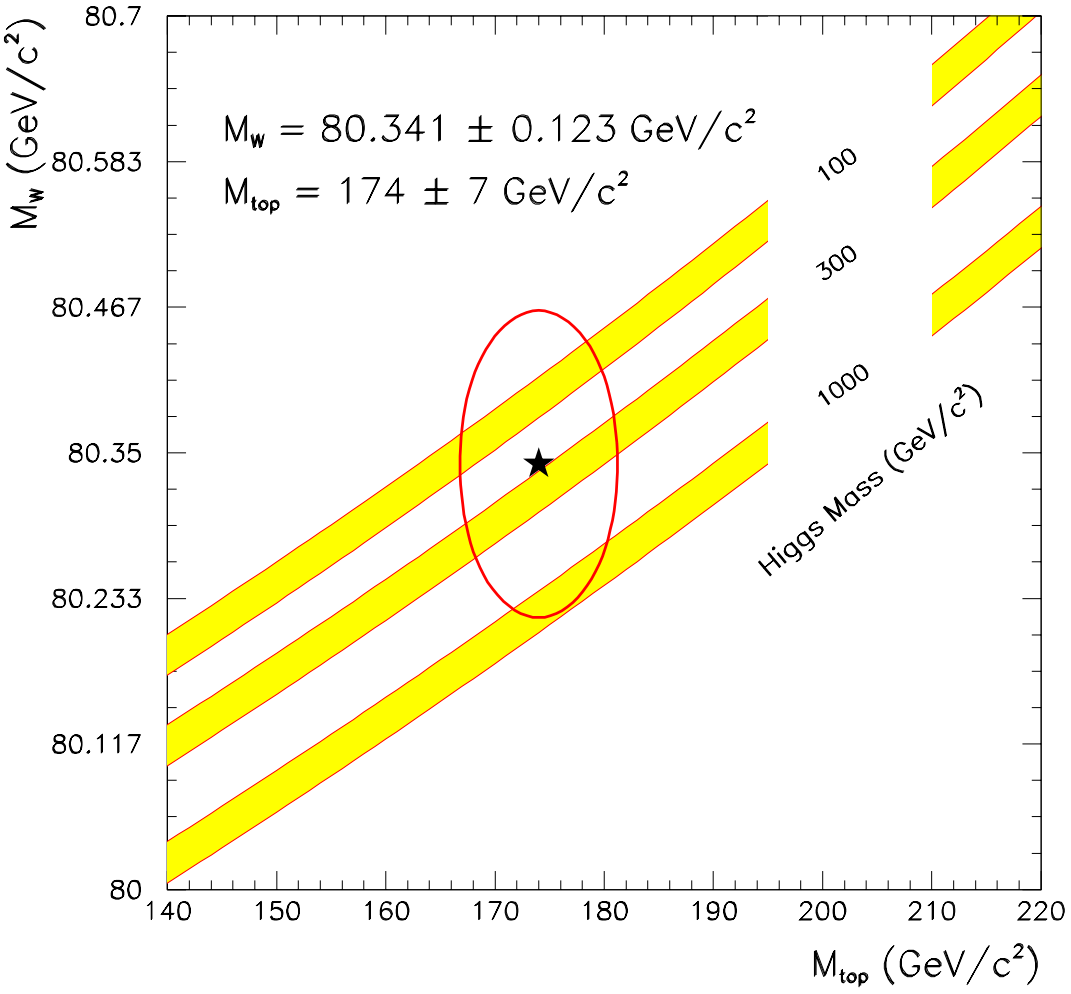

Figure 8.2: The 1σ contour allowed by the world average W boson and top quark masses. The bands are the predictions of the Higgs mass as a function of the W boson and top quark masses.

8.3 The Future

The future will bring evermore precise measurements of the W boson mass. When DØ and CDF combine all their results from Run 1 the error on the W boson mass should be between 80 and 100 MeV/c^2. Currently, the limiting factor on the mass measurement is the number of the W and Z events.

The measurement of the W boson mass at the Tevatron during Run 2, which is scheduled to begin in 1999 and accumulate $\sim 1000\ pb^{-1}$ of data, is expected to have an error of $\sim 50\ MeV/c^2$. There is also discussion about upgrading the Tevatron to provide even higher luminosities and energies after Run 2 [73].

At the moment the e^+e^- collider at CERN (LEPII) is producing W^+W^- pairs. With several years of running each of the four experiments is expected to measure the W boson mass with and error between 60 MeV/c^2 to 80 MeV/c^2. When the four masses are combined, and accounting for the common errors, the error on the mass could be as low as 40 MeV/c^2 [73].

Appendix A

The Muon Scintillation Counter

A.1 Introduction

When the Tevatron is upgraded to 36 bunches the crossing time of the beams will be reduced from 3.5 μsec to 396 nsec. The required drift time of the DØ muon system PDTs is up to 1.2 μsec. In order to accommodate this higher rate a fast detector is needed to identify which interaction produced the muon. To fulfill this task scintillation counters were built and mounted outside the C layer of the WAMUS system. Currently six of the eight octants in azimuth are instrumented. The bottom two octants will be covered after the detector has been rolled out of the collision hall. This appendix covers the design, construction, and testing of these counters. The counters for the forward regions ($|\eta| > 1$) have not yet been built since the requirements in this higher multiplicity region are still under investigation.

A.2 The Muon Scintillation Counter

The motivation for the counter is to provide information on when and where a muon passed through the DØ detector. The procedure is to have the muon interact with a medium which produces light. The light is then piped to a photomultiplier tube which converts the light into an electrical pulse. The pulse is sent to the electronics which digitize the signal. The signal is then available to the trigger for selecting events or later offline for the physicist to use as she sees fit.

A.2.1 Design Considerations

Scintillator was chosen because the counter was required to be a fast. Waveshifting fiber was chosen to readout the scintillator, over a more traditional waveshifting bar or sheet, since this removed the need for the polishing of the scintillator surfaces. The use of fiber allows the phototubes to be positioned at any location along the counter. Thus, the same basic counter design could be used in the very limited space on the bottom of the detector. The use of two phototubes per counter was decided upon to reduce the singles rates from each counter. Each PDT has eight counters mounted on it.

The design of the readout electronics required that the minimum threshold of the output signal be 10 mV. The counters were designed to be 100% efficient for a threshold of 30 mV.

Length (in)	Width (in)	Depth (in)
81.5	25	1/2
108	25	1/2
113	25	1/2

Table A.1: The different sizes of the scintillation counters.

A.2.2 The Scintillator

The counters are made from Bicron 404A 1/2" thick scintillator [74]. The scintillator is 25" wide and from 81.5" to 113" long depending on which PDT it is mounted. At one end of the counter a 45° cut was made on each corner. The cut removed $\sim$1.19 in^2 of scintillator. This cut allowed the counters to be mounted in a nested configuration which removed any geometrical inefficiency. Table A.1 summarizes the different counter sizes. The Bicron 404A scintillator was chosen for its relatively low cost and good performance. The characteristics of the Bicron 404A scintillator are listed in table A.2. A muon passing through this scintillator deposits between 1.8 and 2.0 MeV of energy per centimeter. About 10 photons are created for each keV of deposited energy. Therefore, each muon creates $\sim 2 \times 10^4$ photons in the scintillator.

On the top surface of the scintillator are machined grooves 4 mm wide and 1.75 mm deep, with spacing of the grooves of 8 mm. A groove runs only half the length of the counter. As it nears the center of the counter the depth is decreased until it is flush with the top of the scintillator. From the other end of the counter this procedure is repeated.

Physical Constants for the Bicron 404A	Value
Light Output, % Anthracene	60
Wavelength of Max. Emission (nm)	408
Decay Constant, Main Component (nsec)	2
Bulk Light Attenuation Length (cm)	170
Refractive Index	1.58
H/C Ratio	1.107
Density	1.032
Softening Point (°C)	70

Table A.2: Physical Constants for the Bicron 404A scintillator.

Physical Constants for Bicron BCF91A Fiber	Value
Core material	Polystyrene
Core refractive index	1.60
Cladding material	Acrylic
Cladding refractive index	1.49
Cladding thickness (%)	3
Emission Color	Green
Emission Peak (nm)	494
Decay Time (nsec)	12
1/e Length (m)	>3.5
Trapping Efficiency (%)	3.44 minimum

Table A.3: Physical Constants for Bicron BCF91A fiber.

A.2.3 The Fiber

Bicron BCF91A is used for the waveshifting fiber for the counter [74]. This fiber is specifically designed to be used in conjunction with the 404A scintillator. Table A.3 lists the characteristics of the waveshifting fiber. Four 1 mm fibers area laid in each groove and are epoxied at seven locations with Bicron 600 Optical epoxy. The ends of the counter were polished with a diamond cutter built at Michigan State University. In order to increase the light yield a 0.032" anodized aluminum sheet

was attached to the polished ends with mylar tape [75]. The fiber laid in the grooves that end on the 45° cut are specially prepared. Their ends were polished with the diamond cutter and sputtered with aluminum. In this way all fibers have a reflecting surface on their far end.

At the center of the counter the fibers are bundled together with two *cookies*. A cookie is a hollow acrylic tube, 2" long and 1.5" in diameter, which hold the fibers. Two of the fibers from each groove go to a cookie. The optical epoxy was used to hold the fibers in the cookie. After hardening the diamond cutter was used to polish the face of the cookie.

A.2.4 The Packaging

The scintillator and fiber are wrapped with a white Tyvek [76] sheet. Around the first sheet is wrapped a second more durable Tyvek sheet. Electrical tape is used to secure the Tyvek sheet and cover any holes or seams. The top and bottom surface of the scintillator are then covered with a 0.020" thick aluminum sheet. An 8" by 7 and 13/32" opening is cut in the top sheet for the fiber bundles. Around the hole is mounted an aluminum angle-iron lip. The aluminum sheets are taped together around the perimeter of the counter. To provide the support for the counter Unistrut bars are slipped over the aluminum sheets, around the edges, and bolted together. The counters then had cross braces attached for additional support.

A plastic cover is used to provide access to the fiber bundles. The plastic cover is fastened to the angle-iron with velcro and the seams are taped. Bolted to the

cover are two SHV and BNC connectors for the high voltage and output signal of the phototubes.

A.2.5 The Photomultiplier Tube, Base, and Assembly

The characteristics required of the phototube include: small diameter, fast response, high gain, uniform quality, and that it match the spectral output of the fiber. For this task the EMI 9902KB photomultiplier was chosen. The diameter of the tube is 1.5" with an effective cathode diameter of 1.26". The rise time of the tube is less than 3 nsec. The current amplification of the tube is 10^7 with a dark current less than 10nA. The spectral response of the tube extends into the green region matching the fiber.

In order to be compatible with the DØ high voltage system the construction of the base required that it draw only 0.2 mA at 2000 V. The circuit diagram for the bases is shown in figure A.1. This circuit minimizes output noise by filtering the signal and isolating the signal ground from the common ground. In order to keep the base assembly as compact as possible this circuit was mounted on a 1.75"$\times$1.5" printed circuit board (PCB). This PCB was soldered to a circular PCB which was attached to a Hamamatsu socket. A 2"$\times$4" aluminum cylinder is used to contain the PCBs and provide electromagnetic shielding. The socket protrudes from one end of the cylinder and the BNC and SHV connectors from the other end.

The phototube and base are secured to the cookie with a spring mechanism. Two springs are connected to the aluminum can, they extend along the phototube and are

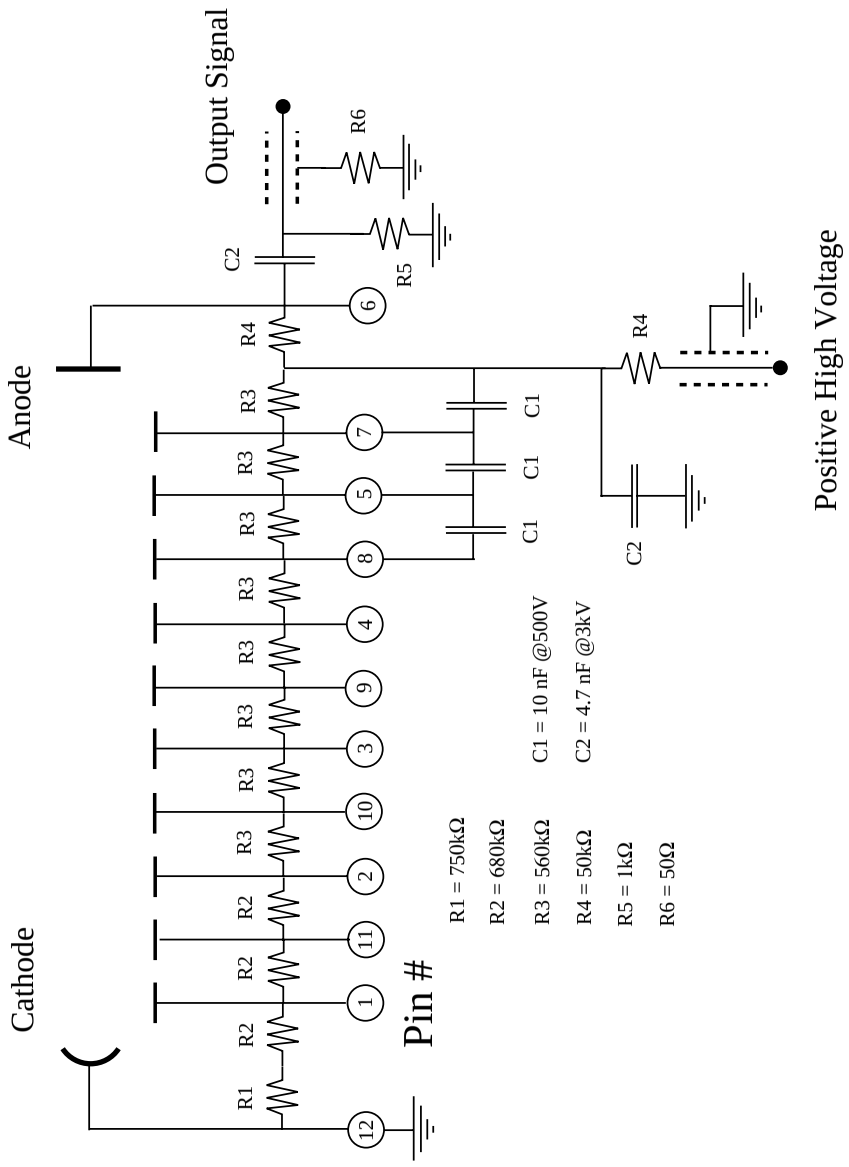

Figure A.1: The circuit diagram for the photomultiplier base.

attached to the cookie with screws. The tension of the springs keeps the phototube flush with the end of the cookie. At the interface of the photocathode and cookie it was decided that optical grease would not be used since tests showed no notable improvement in the efficiency when the optical grease was applied.

Phototubes are very sensitive to magnetic fields. Simply rotating the phototube in the magnetic field of the Earth will change the gain. At DØ the strength of the stray magnetic fields varies depending on the location of the counter. To ensure adequate protection a Magnetic Shield Corporation Model 17P37 magnetic shield was placed around the phototube [77].

The tube-base-shield assembly was connected to the counter with two aluminum fasteners. Each fastener was made in two parts. The bottom part was bolted to the aluminum sheet. The tube-base-shield rested in this bottom part while the top fastener was bolted to the bottom fastener. Two high voltage and signal cables were then connected to the bases and attached to the SHV and BNC connectors of plastic cover.

A.2.6 Quality Control and Testing

Quality control was maintained during all phases of the detector construction. Testing was done on the raw components of the counter and on the counter at different phases of the assembly process. The components that were test include: the scintillator, the fiber, and the phototubes. The counter was tested to obtain its response versus other counters. The completely assembled counter was tested after mating

the counter with the phototubes.

Scintillator

From each delivery one scintillator sheet was selected to be tested to verify that the light output was consistent with prior batches. The scintillator was placed inside a light tight box. A 2 ft by 2 ft anodized aluminum sheet was placed under the scintillator. A ribbon of 91A fiber was laid on top of the scintillator and readout with a EMI9902KA phototube. A cosmic ray *telescope* was used to provide the trigger. The telescope was made from three 1 ft^2 scintillator paddles and a coincidence of the three paddles was used to select a cosmic ray event. The signal from the phototube was sent to a LeCroy QVT which integrates the pulse area. The distribution of charge was compared to a reference set. During this testing no scintillator was rejected due to low response.

Fiber

Every reel of fiber used in counter construction was tested. The fiber was delivered in spools containing 500m of material. From this a 3 m length of fiber was taken and tested at the fiber testing facility at Fermilab. An ultraviolet light, from a pencil source, was used to excite the fiber. The light was then readout using a silicon photodiode. The current from the photodiode is proportional to the light intensity. The test was performed at three locations along the fiber: 30, 150, and 270 cm from the readout end. The fiber was required to pass two criteria: an attenuation length

measurement and an absolute light output measurement.

The attenuation length is defined to be proportional to the ratio of the light intensity at 150 cm to that at 270 cm. Fibers that had a low attenuation length were rejected. The second test measured the absolute light output of the fiber. This value was compared relative to a reference fiber. Eventually 5% of the delivered fiber was rejected by these two tests.

Phototube and Base

To determine the operating voltage, of the phototube and base, the light from an LED was used. Inside a light tight box the green (562nm) LED was pulsed with a fast voltage (8 nsec). The LED was positioned at the center of the photocathode a standard distance away. A voltage was applied to the tube and the signal was sent to a LeCroy QVT where it was integrated. The integrated signal was then compared with a reference tube, a Hamamatsu R580-17, for which the gain had previously been measured. The operating voltage of the EMI tube was defined as that voltage which gave the same integrated signal as the Hamamatsu tube. For different voltages around the operating voltage the pulse heights were measured. This gives information on the gain of tube near the nominal voltage.

Assembled Counter

The counter testing took place in the DØ assembly building. A Digital VAXstation Model 3100 was used to control the testing electronics and to store the test results.

The workstation interfaced with the CAMAC equipment through a Jorway Model 111 PDP-11/CAMAC interface. The apparatus tested three counters at the same time. The counters were stacked on top of one another inside a light tight box. The light tightness of the counters themselves was secured during another test. Only the response of the counter was tested at this stage. The same six photomultiplier tubes and bases were used to test all the counters. The six tubes were selected to have a similar response. Telescopes were setup the counter at three locations; at the ends and in the middle. When a cosmic ray muon fired the telescope the counters were readout. The ratio of observed counter hits to telescope hits defined the efficiency. Figure A.2 is a diagram of the logic for one telescope and counter.

The testing equipment was run 12 to 24 hours. Two runs were made on each set of counters. One with the high voltage was set at the nominal value and one with the voltage set at nominal-200V. These two points allowed a relative comparison to be made between all counters. The procedure was verified by testing a counter that was deliberately built with fibers that failed the quality standards. This counter showed a notable reduction in response. The overall variation in the quality of the production counters was small. Though, in order to make all counters have a similar response, a counter that showed a lower response was matched with a phototube that showed a higher than nominal gain.

The final test before installation involved using the same testing equipment. With the counter in its completed form a test was run with the high voltage set at nominal and then nominal minus 100, 200, and 300V. This test verified that the nominal

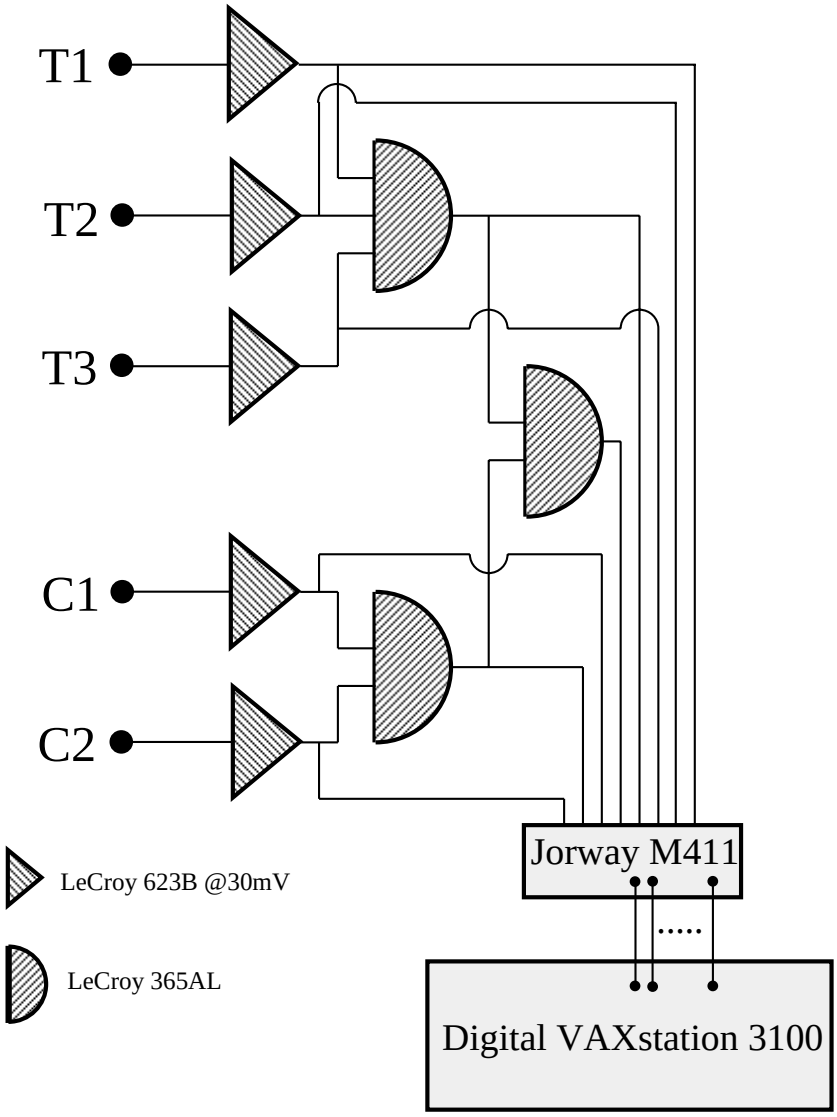

Figure A.2: A partial diagram of the scintillation counter test apparatus. T(1,2,3) refers to the output signal of the three paddles of the telescope. C(1,2) refers to the output of the two photomultiplier tubes for the counter. The LeCroy 623B discriminates the signal with a 30 mV threshold. The LeCroy 365AL is used as a multifold AND logic unit.

voltage was $\sim$100% efficient and gave the turn on curve for the counter. This turn on curve allows thresholds adjustments to be made online without compromising efficiency.

A.3 Conclusion

The scintillation counters were installed and operated during the Tevatron Run 1b. The counters were used successfully in the trigger to help reduce the wasted bandwidth from cosmic rays. The counters are also used in the offline analysis for muon identification.

Bibliography

[1] S. Weinberg, *Phys. Rev. Lett.,* **19** 1264 (1967); S.L. Glashow, *Nucl. Phys.,* **22** 579 (1968); A. Salam, in *Elementary Particle Theory*, ed. by N. Svartholm (Almquist and Wiksell, Sweden, 1968), p. 367; S.L. Glashow, J. Illiopoulos and L. Maiani, *Phys. Rev.,* **D2** 1285 (1970); M. Kobayashi and M. Maskawa, *Prog. Theor. Phys.,* **49** 652 (1973).

[2] G. Arnison, et al. (UA1 Collaboration), *Phys. Lett.,* **B122** 103 (1983).

[3] M. Banner, et al. (UA2 Collaboration), *Phys. Lett.,* **B122** 476 (1983).

[4] G. Arnison, et al. (UA1 Collaboration), *Phys. Lett.,* **B134** 469 (1984).

[5] G. Arnison, et al. (UA1 Collaboration), *Europhys. Lett.,* **1** 327 (1986).

[6] R. Ansari, et al. (UA2 Collaboration), *Phys. Lett.,* **B186** 440 (1987).

[7] C. Albajar, et al. (UA1 Collaboration), *Z. Phys.,* **C44** 15 (1989).

[8] F. Abe, et al. (CDF Collaboration), *Phys. Rev. Lett.,* **62** 1005 (1989).

[9] J. Alitti, et al. (UA2 Collaboration), *Phys. Lett.,* **B241** 150 (1990).

[10] F. Abe, et al. (CDF Collaboration), *Phys. Rev.,* **D43** 2070 (1991).

[11] J. Alitti, et al. (UA2 Collaboration), *Phys. Lett.,* **B276** 354 (1992).

[12] F. Abe, et al. (CDF Collaboration), *Phys. Rev.,* **D52** 4784 (1995).

[13] S. Abachi, et al. (DØ Collaboration), FERMILAB-Pub-96/177-E (1996), to be published in *Phys. Rev. Lett.*

[14] P. Renton, *Precision Tests of Electroweak Theories*, Lepton-Photon Conference, Beijing, P.R.China (1995).

[15] I.J.R. Aitchison and A.J.G. Hey, *Gauge Theories in Particles Physics*, Adam Hilger, 1989, 2nd Edition.

[16] V.D. Barger and R.J.N. Phillips, *Collider Physics*, Addison-Wesley, 1987.

[17] G. Bardin, et al., *Phys. Lett.,* **B137** 135 (1984).

[18] Particle Data Group, *Phys. Rev.* **D54**, part 1 (1996).

[19] R. Partridge, 31st Rencontres de Moriond: QCD and High-energy Hadronic Interactions, Les Arcs, France (1996).

[20] A. Barbaro-Galtieri, *Top Decays and Mass with CDF*, FERMILAB-Conf-96/146-E, 31st Rencontres de Moriond: QCD and High-energy Hadronic Interactions, Les Arcs, France (1996).

[21] J. Collins, and D. Soper, *Nucl. Phys.,* **B193** 381 (1981), erratum **B213** 545 (1983); **B197** 446 (1982). J. Collins, D. Soper, and G. Sterman, *Nucl. Phys.,* **B250** 199 (1985).

[22] P. Arnold and R. Kaufmann, *Nucl. Phys.,* **B349** 381 (1991).

[23] G.A. Ladinsky and C.P. Yuan, *Phys. Rev.,* **D50** 4239 (1994).

[24] N. Hadley, "Cone Algorithm for Jet Finding", DØ Internal Note #904.

[25] J. Smith, W.L. van Neerven, and J.A.M. Vermaseren, *Phys. Rev. Lett.,* **50** 1738 (1983).

[26] Design Report, *The DØ Experiment at the Fermilab $p\overline{p}$ Collider* November, 1984.

[27] S. Abachi, et al. (DØ Collaboration), *Nucl. Instr. and Meth.* **A338** 185 (1994).

[28] A.R. Clark et al., *Nucl. Instr. and Meth.* **A315** 193 (1992).

[29] J. Kadyk, *Nucl. Instr. and Meth.* **A300** 436 (1991).

[30] V.L. Ginzberg and I.M. Frank, *JETP* **16** 15 (1946).

[31] F. Feinstein, Ph.D. Thesis, Northwestern University (unpublished) (1992).

[32] A.R. Clark et al., *Nucl. Instr. and Meth.* **A279** 243 (1987).

[33] R. Avery et al., *IEEE Trans. Nucl. Sci.* **NS-40** 573 (1993).

[34] W. Guryn, *Proc. Second Int. Conf. on Calorimetry in High Energy Physics*, Capri, Italy (1991).

[35] H. Aihara et al., *Nucl. Inst. and Meth.* **A325** 393 (1993).

[36] Terry Geld, *The DØ Intercryostat Detector: Design Considerations and Test Beam Studies and Initial Performance*, Ph.D. Thesis, University of Michigan (unpublished) (1993).

[37] Scott Snyder, *Measurement of the Top Quark Mass in DØ* , Ph.D. Thesis, SUNY at Stony Brook (unpublished) (1995).

[38] P. Grudberg, Ph.D. Thesis, UC Berkeley in preparation.

[39] N. Graf, "Improvements to the Calorimeter Electron Position Algorithm", DØ Internal Note #1352.

[40] R. Brun and C. Carminati, *CERN Program Library Writeup* **W5013** (unpublished) (1993) release v3.14.

[41] S. Glenn and A. Goldschmidt, "Corrections to Biases in Cluster-Track Matching", DØ Internal Note #2419.

[42] N. Graf, DØ Internal Note in preparation.

[43] T. Yasuda, "A Study on CDC z Measurement Using Collider Muon Tracks", DØ Internal Note #2782.

[44] R. Engelmann et al., *Nucl. Inst. and Meth.* **A216** 45 (1983); DØ Collaboration, M Narain, "Proceedings of the American Physical Society Division of Particles and Fields Conference", Fermilab (1992).

[45] M. Demarteau, J. Sculli, and K. Streets, "Measurement of the W Mass", DØ Internal Note #2929.

[46] C. Balasz, J.W. Qiu, C.P. Yuan, *Phys. Lett.,* **B355** 548 (1995).

[47] E. Mirkes, *Nucl. Phys.,* **B387** 3 (1992).

[48] F.A. Berends and R. Kleiss, *Z. Phys.,* **C27** 365 (1985).

[49] F. Paige and S. Protopopescu, *BNL Report,* **BNL38034** (unpublished) (1986) release v7.13.

[50] D. Anderson, *Fermilab Academic Lecture Series: Principles of EM Calorimetry,* DØ Internal Note #1713.

[51] Qiang Zhu, *Measurement of the W Boson Mass in Proton-Antiproton Collisions at* $\sqrt{s} = 1.8TeV$, Ph.D. Thesis, New York University (unpublished) (1994).

[52] G. Eppley, "Multiple Interactions, A Primer", DØ Internal Note #1856.

[53] I. Adam, DØ Internal Note in preparation.

[54] S. Glenn, "A Parametric Detector Simulation for Dibosons", DØ Internal Note #2846.

[55] I. Adam, E. Flattum, U. Heintz, and A. Kotwal, "W Boson Mass Measurement using Run 1b Data", DØ Internal Note #2982.

[56] E. Flattum, "Effect of Electron Identification Cuts on radiative W events", DØ Internal Note #2396.

[57] U. Heintz, DØ Internal Note in preparation.

[58] W.G.D. Dharmaratna, "Reconstruction of the Calorimeter Response-Test Beam Load 2", DØ Internal Note #1731.

[59] S. Rajagopalan, "An Estimate of the Energy Scale Offset at DØ", DØ Internal Note #2481.

[60] P. Grannis, "Calibrations Using Collider Events", DØ Internal Note #796.

[61] U. Heintz, "Reconstruction π^0 Decays in the DØ Detector", DØ Internal Note #2209.

[62] U. Heintz, "A Measurement of the Calorimeter Response using π^0 Decays", DØ Internal Note #2268.

[63] I. Adam, C. Bormann, H. Castilla, N. Denisenko, E. Flattum, A. Sanchez, and M. Tartaglia, "Observation of the $J/\psi \rightarrow ee$ decays at DØ and calibration of the central calorimeter electromagnetic energy scale", DØ Internal Note #2298.

[64] I. Adam, "WZ APS Presentations", DØ Internal Note #2128.

[65] A.G. Frodesen, O. Skjeggestad, and H. Tøfte, *Probability and Statistics in Particle Physics*, Columbia University Press, 1979.

[66] Ian Adam, *A Measurement of the W Boson Mass in $p\overline{p}$ collisions at $\sqrt{s}$ = 1.8 TeV with the E_T distribution*, Ph.D. Thesis, Columbia University, in preparation.

[67] R. Brock, "A Characterization of the Differences Among pdf Fits and their Relationship to W and Z Production", DØ Internal Note #2821.

[68] H.L. Lai, et al. (CTEQ Collaboration), *Phys. Rev.* **D51** 4763 (1995).

[69] F. Abe, et al. (CDF Collaboration), *Phys. Rev. Lett.,* **74** 850 (1995).

[70] M. Demarteau, J. Sculli, and K. Streets, "Studies of Radiative Decays of the W and Z", DØ Internal Note #2470.

[71] M. Demarteau, H. Frisch, U. Heintz, R. Keup, and D. Saltzberg, "Combining W Mass Measurements", DØ Internal Note #2115 and CDF Internal Note #2552.

[72] S. Protopopescu, XXVIII International Conference on High Energy Physics, Warsaw, Poland (1996).

[73] D. Amidei and R. Brock, "Future Electroweak Physics at the Fermilab Tevatron", FERMILAB-Pub-96/082, (1996).

[74] Bicron Corporation, 12345 Kinsman Road, Newbury, OH 44065-9677.

[75] Alcoa Brite Products, Inc. 3040 Northwoods Parkway, Norcross, GA 30071.

[76] Dupont De Nemours & Co., 705 Center Rd., Rt 141, Wilmington, DE.

[77] Magnetic Shield Corp., 740 North Thomas Dr., Bensenville, IL 60106.